Analytical and Numerical Methods for Planar Aperture Antennas

Massimiliano Casaletti

Mémoire pour l'obtention de l'Habilitation à Diriger des Recherches

Sorbonne Université

Spécialité
Sciences pour l'Ingénieur

Présentée par
Massimiliano CASALETTI
Maître de conférences,
Laboratoire d'Électronique et Électromagnétisme (L2E)
Sorbonne Université

Analytical and Numerical Methods for Planar Aperture Antennas

soutenue le 12 octobre 2018

devant le jury composé de :

M. André DE LUSTRAC	Professeur émérite à l'Université Paris Nanterre	Rapporteur
Mme Claire MIGLIACCIO	Professeure à l'Université Nice Sophia-Antipolis	Rapporteur
M. Francesco ANDRIULLI	Professeur à l'École polytechnique de Turin	Rapporteur
M. Boris GRALAK	Chercheur CNRS (CR-HDR) à l'Institut Fresnel	Examinateur
Mme Hélène ROUSSEL	Professeure à Sorbonne Université	Examinatrice
M. Marc HELIER	Professeur à Sorbonne Université	Examinateur
M. Philippe POULIGUEN	HDR, Responsable ondes DGA	Examinateur

Contents

Introduction

I have always been fascinated by mathematics and physics. From my perspective engineering represents the perfect mix using mathematics to explain and control physical phenomena that occur in in the real world. This is especially true for applied electromagnetics. I therefore graduated in 2003 from the University of Siena in Italy with a master degree in Telecommunications Engineering. After two months I obtained a two years Research Training Network grant (AMPER: Application of Multiparameter Polarimetry) at Mothesim (MOdelisation, THEorie et SIMulation) in France to work on polarimetry with Dr. Frédéric Molinet. In parallel I started a PhD at the University of Siena under the supervision of Pr. Stefano Maci. My topic was related to deterministic and stochastic numerical methods for the electromagnetic analysis. After the PhD, I continued my research at Siena with a four-year research associate position during which I worked on metamaterials, beam expansion techniques and numerical methods.
In November 2010, I joined IETR in Rennes as a postdoctoral researcher working with Pr. Ronan Sauleau on substrate integrated waveguide antennas. In September 2013, I joined Sorbonne Université, formerly University of Pierre and Marie Curie, as *maître de conférences*.

The aim of this manuscript is to summarize my research activity and to presents its evolution in the next years. The document is organized into four chapters as follows. The first chapter is my curriculum vitae. The second chapter briefly summarizes my teaching activity. The third chapter introduces my past research and the last chapter presents the research activity I intend to carry on for the coming years.

Note relative aux modalités de rédaction du mémoire d'habilitation à diriger des recherches à Sorbonne Université : *selon les UFR, votre mémoire d'habilitation, synthèse et perspectives de vos travaux d'environ 50 pages (hors les articles joints), en français ou en anglais, peut être ou pas déjà rédige lorsque vous soumettez votre pré-dossier à la CTH.* http://www.sciences.sorbonne-universite.fr/fr/recherche/hdr.html

Chapter 2 : Teaching activities

Since September 2013, I have taught in the Bachelor and Master program at Sorbonne Université. The programs in which I am involved are listed below:

***Bachelor*:** 3-year bachelor program in Electronics at Sorbonne
Master SysCom (Embedded Systems Technologies and Applications speciality): 2-year master program in Engineering Science at Sorbonne.

Since 2015, I am in charge of the new module ***Numerical methods and algorithms (L3).*** This course covers interpolation, numerical integration (classical methods and Gaussian methods), and numerical techniques for ordinary differential equations.

From 2020 I will be also in charge of the new module ***Numerical methods and matlab (L2).*** This course will cover the solution of linear systems (Gaussian Elimination, LU and Cholesky decomposition, over-determined systems).

The teaching activity is detailed in the next sections.

2.1 Teaching activities in first-year bachelor (L1)

2013-2014

- ***Introduction to electronics***
  16h TD 8h TP
- ***Mechanical and electrical systems***
  28h TD 12h TP

2.2 Teaching activities in second and third-year bachelor (L2/L3)

2017-2018

- ***L2 Electrostatic Fields***
  18h TD
- ***L2 Mathematical tools for the electronics 1***
  36h TD
- ***L3 Numerical methods and algorithms***
  8h CM + 16h TD + 56h TP
- ***L3 EM propagation et radiation***
  28h TD + 8h TP

2015-2016

- ***L2 Electrostatic Fields***
  18h TD
- ***L2 Mathematical tools for the electronics 1***
  36h TD
- ***L3 Numerical methods and algorithms***
  8h CM + 16h TD + 56h TP
- ***L3 EM propagation et radiation***
  30h TD + 16h TP

2016-2017

- ***L2 Electrostatic Fields***
  18h TD
- ***L2 Mathematical tools for the electronics 1***
  36h TD
- ***L3 Numerical methods and algorithms***
  8h CM + 16h TD + 56h TP
- ***L3 EM propagation et radiation***
  28h TD + 8h TP

2014-2015

- ***L2 Electrostatic Fields***
  18h TD
- ***L2 Electronics project: heartbeat detector***
  26h TP
- ***L2 Mathematical tools for the electronics 1***
  36h TD
- ***L3 EM propagation et radiation***
  30h TD + 16h TP

2013-2014

- ***L2 Introduction to Matlab***
  15h TD
- ***L2 Electronics project: heartbeat detector***
  22h TP
- ***L3 EM propagation et radiation***
  30h TD + 16h TP

2.3 Teaching activities in master (M1/M2)

2017-2018

- ***M2 Antennas, modelling and radar applications***
  20h TP

2016-2017

- ***M2 Antennas, modelling and radar applications***
  20h TP

2015-2016

- ***M1 alternance Numerical methods for differential equations***
  12h TP
- ***M2 Antennas, modelling and radar applications***
  24h TP

2014-2015

- ***M1 alternance Numerical methods for differential equations***
  12h TP
- ***M1 Numerical methods for differential equations***
  14h TD + 12h TP 1h G
- ***M2 Antennas, modelling and radar applications***
  24h TP

2013-2014

- ***M1 alternance Numerical methods for differential equations***
  12h TP
- ***M1 Numerical methods for differential equations***
  12h TP

2.4 Teaching activities before September 2013

Université Rennes 1, IUT de Rennes and IUT de Saint Malo

2012-2013

- ***L1 Electromagnetics***
  10h TD
- ***L1 Optoelectronics***
  10h TP
- ***M1 Waveguide propagation***
  16h TP

University of Siena (Italy)

2009-2010

- ***M2 Antennas and propagation***
  30h CM
- ***L2 Antenna design***
  24h TP

2008-2009

- ***M2 Antennas and propagation***
  30h CM
- ***L2 Antenna design***
  24h TP

2007-2008

- ***M2 Antennas and propagation***
  30h CM

Chapter 3 : Past research activities

This chapter briefly outlines my research activities during my Master project work in Italy (October 2002 – March 2003, Part I), during my PhD activity in France, England and Italy (October 2003 – October 2006, Part II), my Post-Doc fellowship in Italy (November 2006-October 2010, Part III) and my Post-Doc fellowship in France (November 2010 – August 2013, Part IV). It is worth noting that what presented here does not aim to be complete and exhaustive. For more details the reader should refer to the related articles.

3.1. Master thesis work (October 2002 –March 2003)

Rigorous network representation and dispersion analysis of a Frequency Selective Surface printed over a dielectric slab

***List of related publications*: [P.29], [C.56]-[C.58].**

Introduction

A Frequency Selective Surface (FSS) is a thin surface able to reflect and transmit an incident electromagnetic field based on the frequency of the field [3.1]. It is composed by 2D-periodic array of metallic elements with a unit-cell dimension smaller than the wavelength. Under this latter assumption only one of the infinitude of Floquet's modes propagates. In other words, the field scattered by the FSS under a plane-wave illumination is essentially a plane-wave as for a continuous surface. This means that propagation can be studied by using a simple Transmission Line (TL) along the direction orthogonal to the FSS (equivalent to the dominant Floquet's mode) [3.2] where the FSS is represented in terms of a lumped RLC network placed in parallel across the TL. Under the assumption of lossless element (perfect electric conducting element) the equivalent impedance is purely imaginary.

This model is exact only for an infinitesimally thin FSS, for which the tangential electric field is continuous across the FSS (continuous voltage in the TL) while the magnetic field is discontinuous (current discontinuity in the TL).

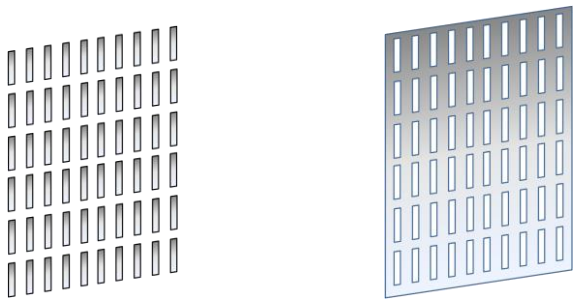

(a) (b)

Figure 3.1 Geometry for a dipole-FSS printed on a grounded dielectric slab.

Figure 3.1 shown to example of the most common types of metasurfaces: the dipole-type cell (a) and the slot-type cell (b). A dipole-type FSS in free space will strongly reflect the wave at the frequency where all the dipole are resonating, while it will reflect little energy below this frequency (and in between two resonances) acting as a stop-band filter. On the contrary, a slot-type FSS will strongly transmit the wave at the frequency where all the slots are resonating in phase, while most of the field will be reflected for other frequencies acting as a pass-band filter.

FSS printed on grounded stratified dielectric media (Fig.3.2) have been widely used during the years for synthesizing artificial surfaces and electromagnetic band-gap (EBG) structures [3.3]-[3.7]. The main advantages of FSS technology is their low cost and easily fabrication. Major effort has been devoted to the implementation with FSS of artificial magnetic conductors (AMC) or surfaces which exhibit "soft" and/or "hard" equivalent boundary conditions. The benefits of such structures are suppression of surface wave coupling, reduction of diffraction lobes, improvement of planar antenna efficiency, realization of compact antennas, and suppression of parallel plate waveguide modes

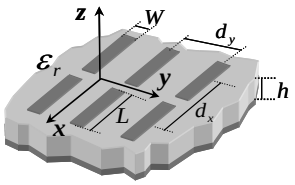

Figure 3.2 Geometry for a dipole-FSS printed on a grounded dielectric slab.

State of the art and motivation at the period of the research

Several authors have treated the artificial surface problem via equivalent lumped circuits to characterize both the reflection and the dispersion properties [3.8]-[3.10]. The lumped parameters are generally based on quasi-static approximations, capable of modeling the surface reflection properties to impinging plane waves in a limited frequency range. Therefore, it is important to derive a rigorous network description valid in a wide range of frequencies and wavenumbers from the visible to the nonvisible region.

Proposed solution

The proposed solution invokes the inductor (L) and capacitance (C) properties of the equivalent boundary impedance associated with the FSS; however, it does not specify particular L and C parameters on a quasi-static approach, but rather it identifies wavenumber-dependent parameters which exhibit weak variations with frequency. These parameters are poles and zeros of the FSS equivalent admittance which is properly defined by a homogenization process. They have the capability of rigorously reconstructing the surface response on a large region of the dispersion diagram.

In the range of frequency where a single propagating Floquet mode occurs, the structures under analysis is equivalent to two coupled transmission line networks, one for the Transverse Electric Field polarization (TE) and the other for the Transverse Magnetic Field polarization (TM) as shown in Fig. 3.3.

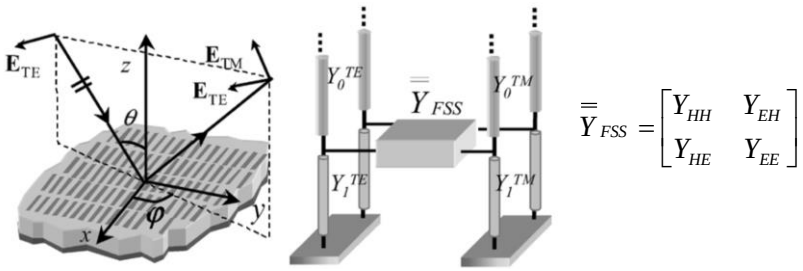

Figure 3.3. EBG structure composed by a FSS printed on a dielectric slab.

Foster's reactance theorem [3.11] implies that the variation of the admittance functions ($Y_{FSS}^{TM}(k_x,\omega)$) with the frequency satisfies pole-zero analytical properties of classical lumped LC admittance functions. An analytical form for $Y_{FSS}^{TM}(k_x,\omega)$ can be then obtained by applying the Forster's theorem knowing the FSS resonances, yielding for the TE and TM case:

$$Y_0^{TM,E}(k_{x,y},\omega)+Y_{1cc}^{TM,E}(k_{x,y},\omega)+Y_{FSS}^{TM,E}(k_{x,y},\omega)=0\,, \tag{3.1}$$

The numerical solution of (3.1) provides the dispersion behavior of both surface and leaky-wave modes. Figure 3.4 shows the results obtained for a structure composed by periodic dipoles printed over a dielectric slab. Full-wave simulations are used for comparison.

The method can be used for the dispersion analysis of new kind of waveguide as the quasi-TEM waveguides with artificial walls [3.12], [3.13] or for planar leaky-wave antenna. In the following an example of the first kind of structures is considered and analyzed. The waveguide is a standard WR90 rectangular waveguide (a=2.286 cm, b=1.018 cm) with the side walls covered by a slab printed with a dipole FSS (Fig.3.5a). In the frequency range where the surface acts as a PMC for grazing incidence, the structure is compatible with a TEM propagation. The modal analysis for the FSS-loaded waveguide is performed through the resonance equation obtained with the transmission line network shown in Fig. 3.5b. The curves obtained with the equivalent network model (Fig. 3.5c) are successfully compared with those obtained by a commercial full-wave simulator (CST™ Microwave Studio). The dispersion curve of the standard TE10 mode of the WR90 waveguide is also shown for comparison (we use here the terminology TE w.r.t. the direction of wave propagation (y), but this is also TE w.r.t. z).

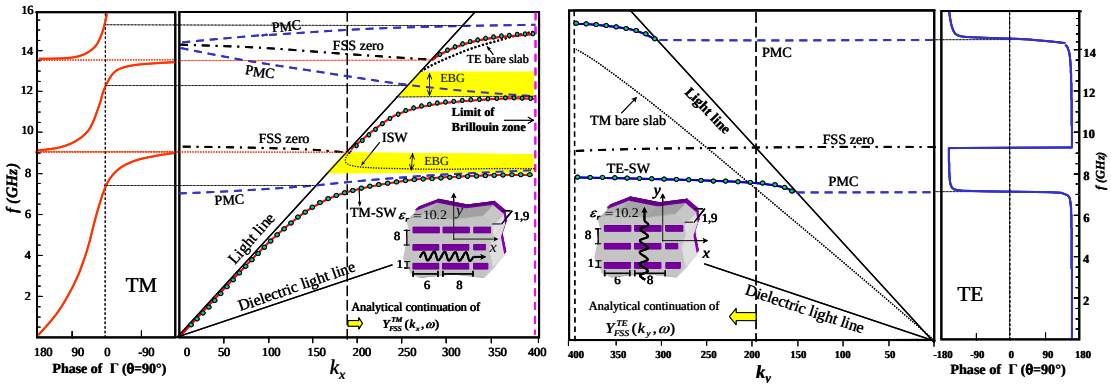

(a) (b)

Figure 3.4. Dispersion diagrams for the structure shown in the inset (dimension in mm). On one side, the phase of the reflection coefficient for grazing incidence is presented. The dispersion curves of the FSS- admittance poles (dash-dotted line) and that of the zero-phase of Γ (dashed line, PMC label) are extrapolated beyond the light line. The vertical line denotes the limit of the region where the analytical expression of the FSS admittance is analytically continued by extrapolation of poles and zeros. The dispersion curves of (a) TM and (b) TE surface wave modes are calculated by the presented method (dots) and by a conventional dispersion full-wave analysis (continuous line).

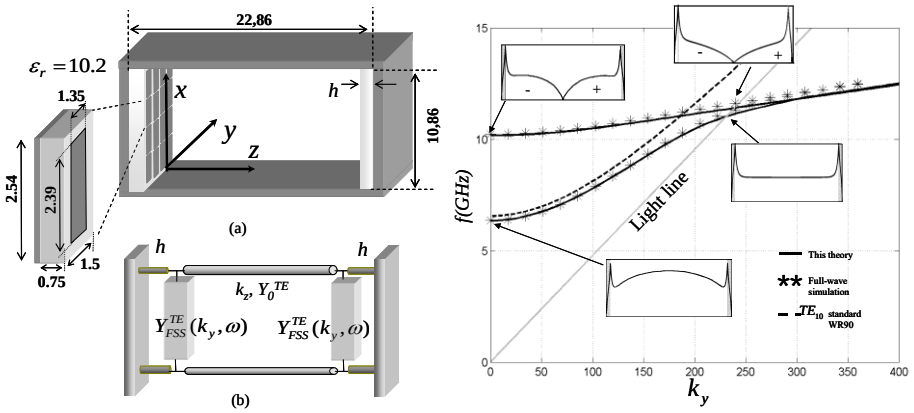

Figure 3.5.Quasi-TEM rectangular waveguide realized by FSS loaded grounded substrates. (b) Relevant transverse transmission line network for deriving the dispersion equation (c) Dispersion diagram for a rectangular waveguide with vertical walls loaded by FSS. In the insets: amplitude profile of the modes in the transverse plane at various frequencies.

References

[3.1] B. A. Munk, *Frequency Selective Surfaces: Theory and Design*. NewYork: Wiley, 2000.

[3.2] L. Felsen and N. Marcuvitz, *Radiation and Scattering of Waves*, NJ:IEEE Press, 1994.

[3.3] F.-R. Yan, M. Kuang-Ping, Y. Qia, and T. Itoh, "A novel TEM waveguide using uniplanar compact photonic-bandgap (UC-PBG) structure," *IEEE Trans. Microw. Theory Tech*, vol. 47, no. 11, pp. 2092–2098, Nov. 1999.

[3.4] P. S. Kildal, "Artificially soft and hard surfaces in electromagnetics,"*IEEE Trans. Antennas Propag.*, vol. 38, no. 10, pp. 1537–1544, Oct. 1990.

[3.4] F.Yang andY. Rahmat-Samii, "Microstrip antennas integrated with electromagnetic band-gap (EBG) structures: a low mutual coupling design for array applications," *IEEE Trans. Antennas Propag.*, vol. 51, no. 10, pp. 2936–2946, Oct. 2003.

[3.5] , "Reflection phase characterizations of the EBG ground plane for low profile wire antenna applications," *IEEE Trans. Antennas Propag.,Special Issue on Metamaterials*, pt. I, vol. 51, no. 10, pp. 2691–2703, Oct. 2003.

[3.6] J. Y. Zhang, J. Y. von Hagen, M. Younis, C. Fischer, and W. Wiesbeck,"Planar artificial magnetic conductors and patch antennas," *IEEE Trans.Antennas Propag., Special Issue on Metamaterials*, pt. I, vol. 51, no. 10,pp. 2704–2712, Oct. 2003.

[3.7] R. Leone and H. Y. D. Yang, "Design of surface-wave band-gaps for planar integrated circuits using multiple periodic metallic patch arrays," in *Microwave Symp. Digest IEEE MTT-S*, vol. 2, May 20–25, 2001, pp. 1213–1216.

[3.8] Fei-Ran Yan, Kuang-Ping M, Yongxi Qia, T. Itoh, "A novel TEM waveguide using uniplanar compact photonic-bandgap (UC-PBG) structure", *IEEE Trans. Microwave Theory Tech*, vol. 47, no.11, pp. 2092-2098, Nov. 1999

[3.9] S. Tretyakov, *Analitical Modeling in Applied Electromagnetics*. New York: Artech House, 2003.

[3.10] A. Grbic and G. V. Eleftheriades, "Periodic analysis of a 2-D negative refractive index transmission line structure," *IEEE Trans. Antennas Propag., Special Issue on Metamaterials*, pt. I, vol. 51, no. 10, pp. 2604–2611, Oct. 2003.

[3.11] Foster, R. M., " A reactance theorem", Bell System Technical Journal, vol.3, no. 2, pp. 259–267, November 1924.

[3.12] R. Orta, R. Tascone, D. Trinchero,G. Loukos, J.C. Vardaxoglou, "Dispersion curves and modal fields of waveguide with FSS inserts", *Electronics Letters*, vol. 31 , no. 13, pp. 1073 – 1075, June 1995.

[3.13] A. Cucini, M. Caiazzo, P. Bennati, S. Maci, "Quasi-TEM waveguide by using FSS-based hard surfaces," URSI EMT Symposium, Pisa, Italy, May 2004.

3.2. PhD frame-time (October 2003 – October 2006)

Deterministic and stochastic methods for the electromagnetic analysis of complex structures

The PhD work has been divided in 3 different research activities:

- **Part I: "Field diffracted by an arbitrary target in front of a statistical flat rough surface"** - This part has been developed at the private company MOTHESIM (Modélisation, Théorie et SImulation Mathématiques), France under the European RTN research contract AMPER (Application of Multi-Parameter Polarimetry). Supervisor Dr. F. Molinet. During this time the author have spent one month at the University of Essex, England under the supervision of Dr D. Bebbington.
- **Part II: "Iteration-free approach to the scattering from large objects by using incremental diffraction-type special functions"** - developed at the University of Siena Italy in collaboration with the Politecnico di Torino, Italy under the supervision of Prof. S. Maci and Prof. G. Vecchi.
- **Part III: "Efficient computation of the mixed potential dyadic Green's function for dielectric multilayer structures"** - developed at the University of Siena in collaboration with the private company I.D.S. (Ingegneria dei Sistemi), Italy under the supervision of Prof. S. Maci and Dr. Alessia Polemi. The numerical implementation of the developed theory has been included in the commercial software ADF-EMS (Antenna Design Framework – ElectroMagnetic Satellite).

***List of related publications*: [P.28], [C.52]-[C.55].**

3.2.1 Field diffracted by a target in front of a statistical flat rough surface

Motivation and State of the art at the period of the research

The radar scattering from rough surfaces has been investigated by many researchers and an extensive literature exists on this subject. In contrast, only few works have been done for the scattering of a deterministic target in front of a rough surface or bared in a medium limited by a rough surface due to the difficulty of the problem.

Activity goals

The scope of the first part of the PhD project has been the development of a new approach able to overcome the limitations of existing procedures. Attention has been devoted to the near-field interactions between the object and the rough surface. These interactions are important for an exact formulation of the problem and derivation of the field diffracted by the arbitrary target.

Proposed solution

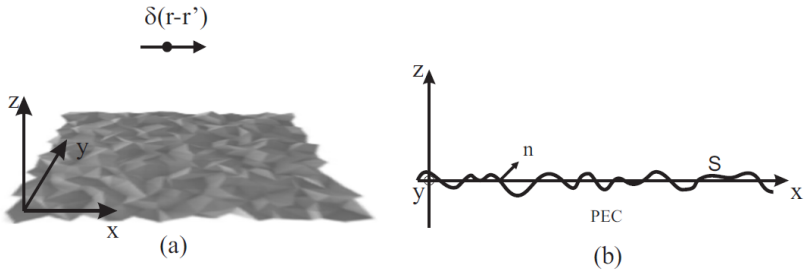

Figure 3.6 Geometry for the Green's function problem.

The basic idea in order to solve the problem has been the derivation of the Green's function for the half-space delimited by a flat random rough surface (Fig. 3.6). This has been done using a second order perturbation method. The surface high profile $h(x,y)$ is described as a continuous stochastic process in the spatial variables x and y with zero average, variance σ^2 and autocorrelation function $R_{h,h}$. Under the assumption that the roughness is small compared to the incident wavelength ($\forall x,y \in S,\ |h(x,y)| < \lambda$) and for small gradients of the height function ($|\nabla h(x,y)| \ll 1$), it is possible to develop the field on the boundary S in Taylor's expansion around the average height $z = 0$

$$\hat{\mathbf{n}}\times\mathbf{E}\big|_{z=h(x,y)} \simeq \hat{\mathbf{n}}\times\mathbf{E}\big|_{z=0} + h(x,y)\frac{\partial}{\partial z}\hat{\mathbf{n}}\times\mathbf{E}\Big|_{z=0} + \frac{h^2(x,y)}{2}\frac{\partial^2}{\partial z^2}\hat{\mathbf{n}}\times\mathbf{E}\Big|_{z=0} . \tag{3.2}$$

The total field $\mathbf{E}$ is decomposed as the sum of the incident field $\mathbf{E}_{inc}$ and the scattered field by the surface $\mathbf{E}_{scat}$: $\mathbf{E} = \mathbf{E}_{inc} + \mathbf{E}_{scat}$.

Perturbation theory assumes that the scattered field may be written as a series:

$$\mathbf{E}_{scat} = \sum_n \mathbf{E}_s^{(n)} , \tag{3.3}$$

where the n-order term $\mathbf{E}_s^{(n)}$ is $O(h^n)$.

Since in general $\partial h(x,y)/\partial x$ and $\partial h(x,y)/\partial y$ are $O(kh)$, the boundary condition in (3.2) can be satisfied separately equating the terms of the same order.

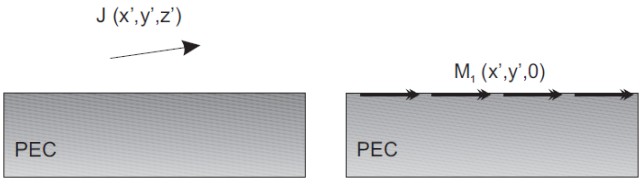

(a) (b)

Figure 3.7 Equivalent problems for the zero order solution (a) and for the higher order solutions (b)

The zero order solution is given by the solution of the flat surface problem (Fig. 3.7a). Higher order solutions are equivalent to the field radiated by a magnetic current distribution placed on the flat surface (Fig. 3.7b), which amplitude is given by the tangential electric field on the surface obtained for the previous order solution. The second order magnetic current is thus given by the field radiated by the first order current on the source himself. This fact implies that a singularity extraction has to be carefully done.

Figure 3.8 presents the Green's function for an electric dipole placed at a wave length from a smooth rough surface with σ = 0.1λ and Gaussian correlation length 1λ. The average electric field in the dipole plane is presented. As can be seen the field is lightly perturbed by roughness. As RMS increases, the average field becomes more and more perturbed by roughness (Fig. 3.9).

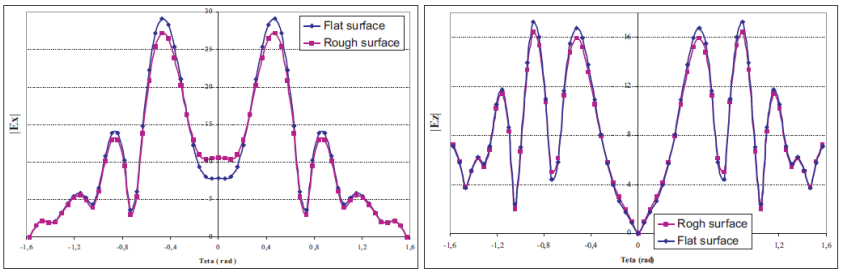

(a) (b)

Figure 3.8 Electric Average Far Field (a) X-component (b)Y-component.

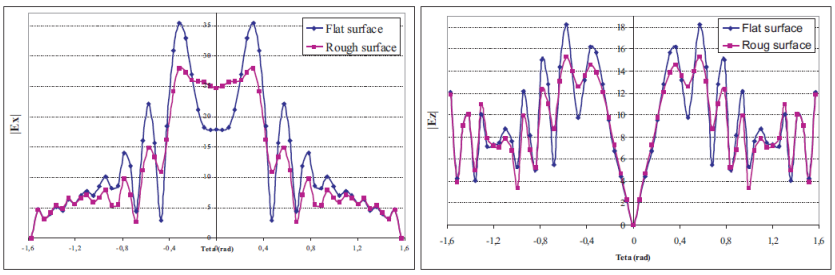

(a) (b)

Figure 3.9 Electric Average Far Field (a) X-component (b)Y-component.

Then the derivation of the scattered field by a target in front of the rough surface has been addressed using an integral equation approach (electric field integral equation) with a Method of the Moments scheme. It has been shown that only the inverse of the mean value of this integral operator (or the corresponding solution impedance matrix) needs to be calculated in order to derive the zero, first and second order terms of the induced currents and radiated field. Both quantities are random variables. The elements of the coherency matrix are then calculated once the diffracted electromagnetic field is known.

3.2.2 Iteration-free approach to the scattering from large objects by using Incremental diffraction-type special functions

State of the art at the period of the research

The Integral Equation (IE) approach combined with the Method of the Moments (MoM) is widely used in the derivation of the electromagnetic scattering [3.14]. Conventional MoM formulations are severely limited by the problem size leading in some cases to large, dense and sometimes ill-conditioned matrices. Different approaches have been presented in literature to overcome these problems. The iteration free approach is an interesting method, where standard basis functions are aggregated into larger functions (Synthetic Function eXpansion - SFX) [3.15], [3.16]. These aggregate basis functions are obtained from the numerical solution of smaller-size problems, and then used in the MoM solution of larger problems.

Activity goals

We have proposed an analytical method to generate SFX to analyze large areas of rough-edge perfectly metallic planar objects.

Proposed solution

The core of the proposed method is based on the construction of basis functions (BF) describing the edge diffraction effects. The key issue investigated here is the excitation mechanism employed to generate these basis functions. Two different approaches are investigated, and the relevant results critically compared: 1) spherical wave generated diffraction BFs; 2) and grazing plane-wave generated BFs with different propagation directions.

A) SPHERICAL WAVE GENERATION OF PHYSICAL OPTICS BASIS FUNCTIONS (SWG-POF)

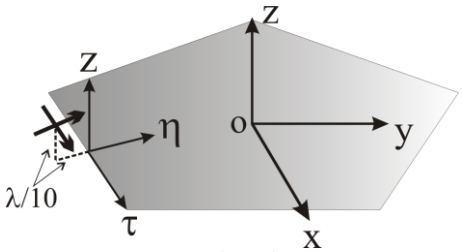

Figure 3.10 Geometry for defining SWG-POF

The diffraction process can be described by equivalent spherical wave incremental contributions arising from the edges. Elementary dipoles distributed close to the edge are used as generating sources of fringe currents as shown in Fig. 3.10 with the geometry of the problem.

The electric dipoles are centered at a generic position τ' and displaced at $\lambda/10$ from the edge along both τ and η in order to avoid inappropriate singularities at the edge. Pairs of dipoles parallel and orthogonal to the edge are used to consider both polarizations, namely TE and TM. The PO induced currents normalized with respect to the maximum values can be approximated by the following expressions:

$$\begin{Bmatrix} \mathbf{f}_{\tau}(x',x,y) \\ \mathbf{f}_{\eta}(x',x,y) \end{Bmatrix} = \sum_m \frac{\alpha}{\pi\lambda} \frac{e^{-jkr_m}}{r_m} \left(1-\tfrac{1}{kr_m}\right) \chi(x,y) \begin{Bmatrix} \hat{\boldsymbol{\tau}}_m \\ \hat{\boldsymbol{\eta}}_m \end{Bmatrix} \tag{3.4}$$

where: $\hat{\boldsymbol{\tau}}_m = \hat{\mathbf{s}}_m^- = \dfrac{(\mathbf{v}_{m+1}-\mathbf{v}_m)}{|\mathbf{v}_{m+1}-\mathbf{v}_m|}$, $\hat{\boldsymbol{\eta}}_m = \hat{\mathbf{z}} \times \hat{\mathbf{s}}_m^-$, $r_m = \sqrt{(\tau-\tau')^2+(\eta-\lambda/10)^2+(\lambda/10)^2}$, $\hat{\mathbf{s}}_m^- = \dfrac{(\mathbf{v}_{m+1}-\mathbf{v}_m)}{|\mathbf{v}_{m+1}-\mathbf{v}_m|}$,

$\mathbf{v}_m$ (m=1,.. N) are the position vectors of the s-block surface vertexes, α is a normalization constant, and $\chi(x,y)$ is the characteristic function of the s-block equal to one inside the s-block and zero elsewhere. The basis functions are normalized in such a way that the maximum value of the amplitude (obtained for $\eta = 0$, and $\tau = \tau'$) is equal to one. The generating sources are placed along the polygonal contour of the surface with uniform steps, thus constructing a sequence like $\mathbf{f}_{n,\xi}(x,y) = \mathbf{f}_{\xi}(n\delta,x,y)$. These functions are called Spherical wave generated-PO functions (SWG-POF) since derived by currents reconstructing diffraction effects,. The step δ between contiguous generating sources will be chosen according to a spectral Singular Value Decomposition (SVD).

(B) NEARLY GRAZING PLANE WAVE GENERATION OF PO BASIS FUNCTIONS

An alternative description of the diffraction contribution can be given in terms of BFs generated by propagating nearly grazing plane waves. As a generating source we taken TE or TM polarized plane waves characterized by the wave-vector $\mathbf{k}' = \mathbf{k}_t' + \mathbf{z}\sqrt{k^2 - \left(k_x'\right)^2 - \left(k_y'\right)^2}$, where $\mathbf{k}_t' = k_x'\hat{\mathbf{x}} + k_y'\hat{\mathbf{y}}$ is the transverse to z part of $\mathbf{k}'$, and k is the free-space wave-number. The transverse wave-vectors $\mathbf{k}_t'$ associated to the generating plane waves are chosen so that $k^2 \tilde{\tilde{<}} \left(k_x'\right)^2 + \left(k_y'\right)^2$ (near grazing incidence) with a constant angular step; namely

$$\mathbf{k}_{tn}' = k\left(\sin\left(n\Delta\phi\right)\hat{\mathbf{x}} + \cos\left(n\Delta\phi\right)\hat{\mathbf{y}}\right) \tag{3.5}$$

where the step $\Delta\phi$ between contiguous wave-numbers will be chosen according to the SVD scheme in a similar way as for the selection of the spherical wave basis functions. The normalized PO currents associated to the above plane waves are given by

$$\mathbf{f}_{n,TM}(\mathbf{k}', x, y) = \mathbf{k}_{tn}' e^{-j(k_x'x + k_x'y)}\chi(x, y), \quad \mathbf{f}_{n,TE}(\mathbf{k}', x, y) = \mathbf{k}_{tn}' \times \hat{\mathbf{z}} e^{-j(k_x'x + k_x'y)}\chi(x, y) \tag{3.6}$$

where χ is the above-defined characteristic function of the polygonal surface. We note that in order to interpret the TE component in (3.6) as a normalized grazing wave PO current for TE polarization, we should apply a process to the limit for *near* grazing of the *normalized* currents.

As an example, a square flat plate of dimension $L = 4\lambda$ is illuminated by an electric dipole at 1 wavelength from the plate. The plate has been considered as a unique block in the iteration-free procedure. The simulations have been done by using 98 SWG-SFX and 80 PWG-SFX. Figs.3.11 shows the comparison of the far field and the induced currents with a standard MoM (FEKO™) using 12800 RWG BFs. A very good agreement is observed with the results obtained using just 98 SWG-SFX and 80 PWG-SFX. Both types of basis functions reduce the computational cost of the MoM analysis of large and complex structures presenting wide edged flat metallic surfaces. The most evident computational gain consists on a reduction of the MoM matrix size that has a dimension proportional to the perimeter and not to the plate area. A comparison of the two different generating processes shows that the spherical wave generation approach is more accurate. On the other hand, the plane wave generation approach exhibits advantages of closed form spectral domain entries, with favourable capability in treating electrically large problems.

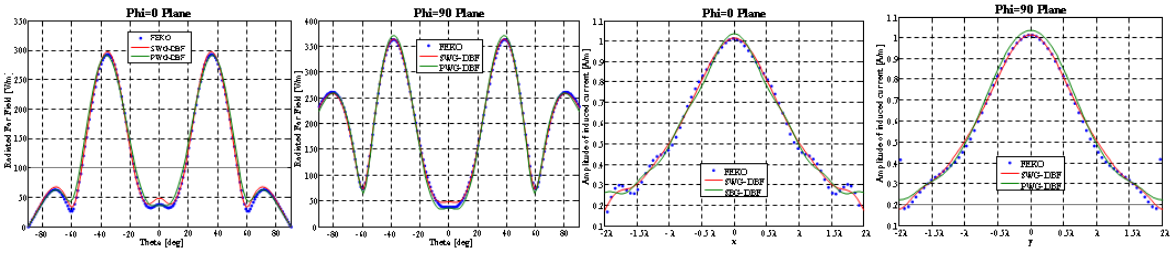

(a) (b) (c) (d)

Figure 3.11 Square plate, $L = 4\lambda$ **;** Induced currents: (a) E-plane; (b) H-plane. Far-field (c) E-plane; (d) H-plane. The comparison is done between the proposed method and full-wave simulation using FEKO.

3.2.3 Efficient computation of the mixed potential dyadic Green's function for dielectric multilayer structures

Motivation and State of the art at the period of the research

Mixed potential formulation represents the state of the art for the Integral Equation approach to electromagnetic scattering problems. This approach requires the computation of scalar and vector potentials associated to both electric and magnetic sources using their associated dyadic Green's functions. The computations of these quantities for a homogenous medium are expressed in a simple and well-known form while the case of dielectric stratified medium represents a challenging problem.

The private company I.D.S. (Ingegneria dei Sistemi[3.17]) was interested including the dyadic Green's function for stratified mediums (figure 3.12) in their commercial software ADF-EMS (Antenna Design Framework – ElectroMagnetic Satellite). This activity has opened the possibility to analyze planar antennas (patches, etc.) with ADF-EMS using an IE-Method of the Moment method.

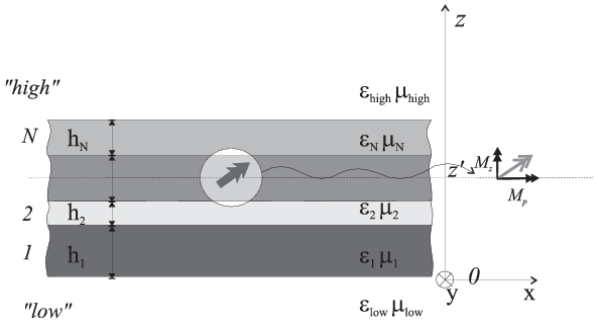

Figure 3.12 Geometry of the Green's function problem for a dielectric multilayer structure.

Activity goals

Computation of the mixed potential Green's function for stratified medium and implementation of an efficient routine.

Proposed solution

The problem has been solved using a 2D spectral domain representation. Each dyadic component is expressed as a bi-dimensional inverse Fourier integral. Different acceleration techniques have been applied to each component in order to speed-up the numerical integration process. No details are given due to contract policy. Results obtained with the developed code has been successfully compared to those obtained with the available state of the art Method of the Moments commercial software's (Ansoft Designer™ and FEKO™) at a reduced computational time.

References

[3.14] Roger F. Harrington, "Field Computation by Moment Methods" , Wiley-Blackwell, 21 April 1993.
[3.15] P. Pirinoli, L. Matekovits, G. Vecchi, F. Vapiana, and M. Orefice, "Synthetic functions: multiscale MoM analysis of arrays," *Proceedings of the 2003 IEEE Antennas Propagation Society Symposium, vol. 4, pp. 799-802, Columbus, 22-27 June 2003.*
[3.16] V. V. S. Prakash and R. Mittra, "Characteristic basis function method: A new technique for fast solution of integral equations," *Microwave and Optical. Technology Letters, pp. 95–100, Jan. 2003.*
[3.17] https://www.idscorporation.com/

3.3. Post-Doc frame-time I (November 2006 – October 2010)

During the post-doc fellowship at the University of Siena my research activity have been focused on 3 different research topics:

- Electromagnetic scattering form electrically large objects.
- Efficient beam expansion of the field radiated by apertures.
- Planar metasurface structures.

***List of related publications*: [P.19], [P.22]-[P.27], [IC.7]-[IC.19], [C.32],[C.34]-[C.35],[C.39]-[C.50].**

3.3.1 Electromagnetic scattering form electrically large objects

State of the art and motivation at the period of the research

Iteration free approaches have been introduced in the recent years for the prediction of the electromagnetic scattering from large complex objects [3.18][3.19][3.20][3.21]. All these approaches are of the Domain-Decomposition type, and rely on segmenting the structure in smaller parts, called blocks. Each block is analyzed in the presence of several auxiliary sources that represent the effect of all the other blocks. The solution of the corresponding electromagnetic problem is then used to construct basis functions (BF), called Synthetic Functions (SFX), over the considered block. To this end a Singular Value Decomposition (SVD) is used to select the relevant and linearly independent responses [3.18][3.20][3.21]. These new functions are subsequently used in the full-wave MoM analysis to the entire structure. *The generation of the SFX is time consuming because several simulations of each block alone has to be performed. Moreover there is still not a clear criterion for the selection of auxiliary sources.*

Proposed solution

To overcome such limitations, I have contributed to the development of two new kind of entire domain BFs generated analytically, as presented in the following sections:
- Section (A) presents the derivation of BFs for generic planar surfaces.
- Section (B) describes the extension to a generic curved surface.

(A) Flat surfaces

A new type of analytical entire-domain BFs have been introduced for the analysis of the electromagnetic scattering from multifaceted bodies and radiation from planar apertures. The BFs are particularly suited for polygonal contours; however, arbitrary contours may be treated with the same technique.

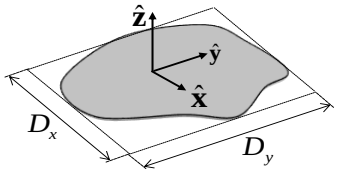

Figure 3.13 Geometry of the problem

The induced current $\mathbf{J}(x,y)$ on a general flat surface is a spatially limited function (Fig.3.13 shows the geometry of the problem). This property implies the applicability of the usual sampling (Shannon) theorem to express its Fourier spectrum $\tilde{\mathbf{J}}\left(k_x,k_y\right)$ as a function of an infinite set of spectral samples, leading to:

$$\mathbf{J}(x,y)=\Delta k_x\Delta k_y\sum_{n,m=-\infty}^{+\infty}\tilde{\mathbf{J}}\left(n\Delta k_x,m\Delta k_y\right)W(x,y)e^{-j\left(k_{xn}x+k_{ym}y\right)} \qquad (3.7)$$

where $\Delta k_{x,y}=2\pi/D_{x,y}$, $W(x,y)=1$ on the surface, zero elsewhere. Equation (3.7) state that every current distribution defined over a flat face can be represented as a sum of linear phase functions (LPF).
The completeness of the BF set can be easily demonstrated by the delta-Dirac reconstruction in its spatial and spectral representation:

$$\delta(x,y)=\Delta k_x\Delta k_y\sum_{n,m=-\infty}^{+\infty}W(x,y)e^{-j\left(k_{xn}x+k_{ym}y\right)}\,,\qquad 1=\Delta k_x\Delta k_y\sum_{n,m=-\infty}^{+\infty}\tilde{W}\left(k_x-k_{xn},k_y-k_{ym}\right) \qquad (3.8)$$

The free space Green's function has the well-known properties to behave as a low-pass filter for the current in the 2D spectral domain. Relation (3.8) state that the summation of $\tilde{W}$ centered in the phase lattice is a equal to the unity. This latter aspect has been used in order to find the function needed to represent the circular spectral domain Ω_γ (of radius η) defined by the band-pass of the Green's operator. A truncated version of the r.h.s. of (3.8) has been introduced with summation extended to the spectral samples inside a circular domain $\Omega_{\gamma'}\subset\Omega_\gamma$ of radius $\eta'>\eta$.

Namely, as a criterion of truncation to define the degrees of freedom, we impose that in Ω_η the average quadratic error in reconstructing unity is less than a fixed threshold $\varepsilon'_{\min}$ by summing spectral LPF with phasing inside $\Omega_{\eta'}$. Fig. 3.14 shows this procedure for a triangular plate. The required flatness can be achieved by gradually filling the spectral circle Ω_η by increasing the number of spectral LPF.

The number of degrees of freedom N_{DoF} can be defined as the number of LPF inside $\Omega_{\eta'}$ multiplied by a factor 2 to account for the two polarizations, thus leading to the approximation

$$N_{DoF}\approx 2\frac{\pi\left(k_0\eta'\right)^2}{\Delta k_x\Delta k_y}=2\frac{\pi D_xD_y\left(\eta'\right)^2}{\lambda^2} \qquad (3.9)$$

wherein λ is the free-space wavelength. The approximation in (3.9) is more accurate for increasing dimension of the plate in wavelength. Figures 3.15-3.16 show the proposed method applied to a metallic disc and to a corner.

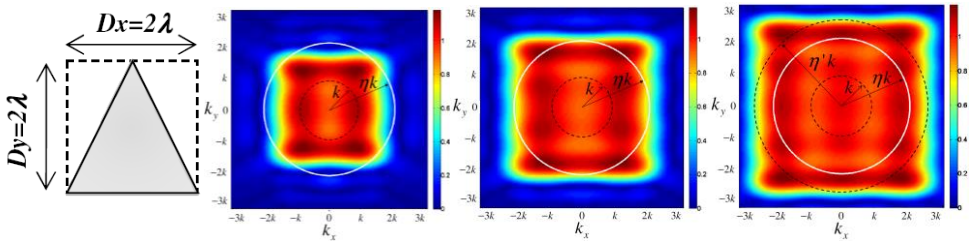

Figure 3.14 Filling of the spectral circle of radius area ηk_0 ($\eta=2.1$) for a triangular surface as in (a) by increasing the number of spectral LPF functions. (a) Wavenumbers within a circle of $1.5k_0$; (b) Wavenumbers within a circle of radius $2k_0$, (c) Final setting of $\eta'=2.5$ with error $\varepsilon'_{\min}=0.03$ with respect to unity.

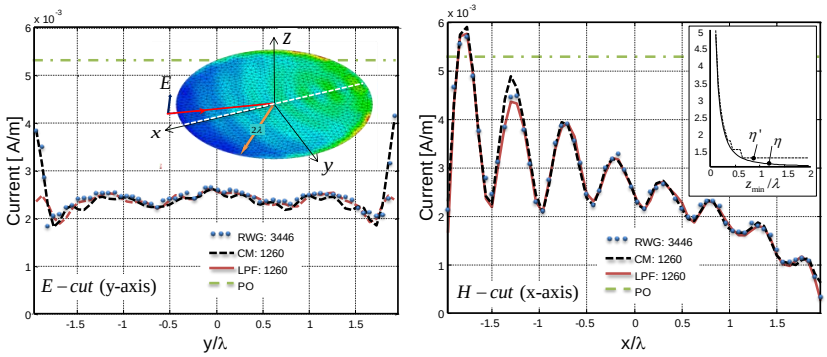

(a) (b)

Figure 3.15. Induced current amplitude on the E-plane (a) and H plane (b) for a circular plate illuminated close to grazing incidence ($\theta = 80°$, geometry shown in the inset of (a)). Comparison among RWG (3446), LPF expansion (1260), and Circular waveguide mode (CWM) expansion (1260). The inset of Fig (b) shows the behavior of η and η' as a function of the observation level.

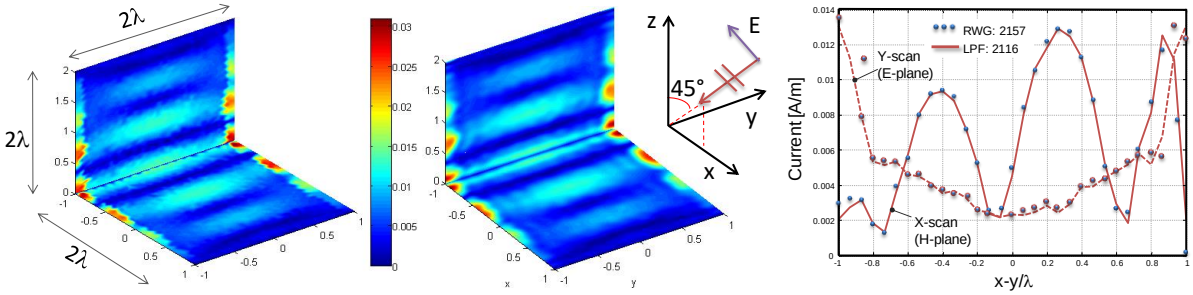

(a) (b) (c)

Figure 3.16 Currents on a perfectly conducting corner reflector composed by two orthogonal square plates of side 2λ , illuminated by a plane wave. (a) Colored map of the MoM currents (2157 unknowns). (b) Colored map of the LPF expansion (2116 terms). (c) Comparison of current amplitude on the bottom face

(B) Curved surfaces

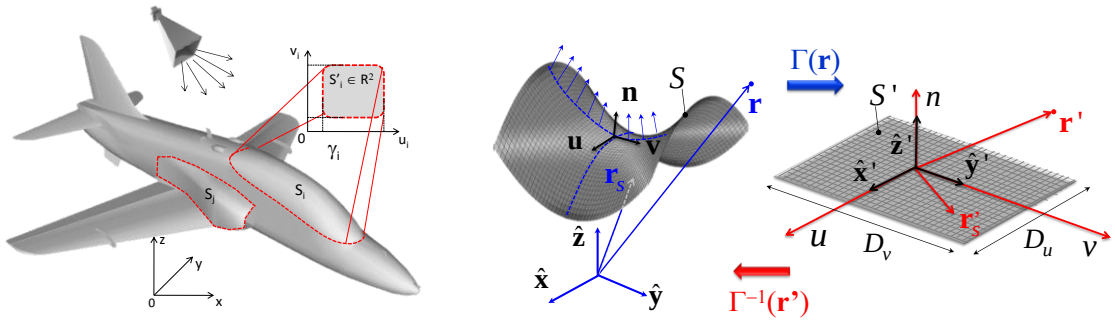

(a) (b)

Figure 3.17 (a) Example of representation of generic surface S as a collections of portion (patches) with relative local mappings. (b) Transformation Γ used for mapping the curved surface S of curvilinear parameter ***u, v*** and normal ***n***, in a flat parametric surface. The inverse function is denoted by Γ^{-1}. The parametric domain can be arbitrary contoured.

A complete set of entire-domain BFs have been introduced for the analysis of scattering from bodies with curved surfaces (figure 3.17a); they are defined via the application of a generalization of the Shannon sampling theorem. The BFs are defined for curved patches with arbitrary contours, via a three-step procedure (for simplicity only the basic ideas are presented):

1) First, the curved patch is mapped, via Transformation Optics [3.22]-[3.24], onto a flat parametric domain surrounded by a virtual anisotropic inhomogeneous space (Fig. 3.17b) described by the permittivity and permeability tensors $\underline{\underline{\boldsymbol{\varepsilon}}}'$, $\underline{\underline{\boldsymbol{\mu}}}'$:

$$\underline{\underline{\boldsymbol{\mu}}}' = \mu_0 \underline{\underline{\boldsymbol{\alpha}}}\ ;\quad \underline{\underline{\boldsymbol{\varepsilon}}}' = \varepsilon_0 \underline{\underline{\boldsymbol{\alpha}}};\quad \underline{\underline{\boldsymbol{\alpha}}} = \det[\Lambda]\underline{\underline{\boldsymbol{\Lambda}}}^{-1}\cdot\left(\underline{\underline{\boldsymbol{\Lambda}}}^{T}\right)^{-1},\quad \underline{\underline{\boldsymbol{\Lambda}}} = \begin{bmatrix} \frac{\partial x}{\partial u} & \frac{\partial x}{\partial v} & \frac{\partial x}{\partial n} \\ \frac{\partial y}{\partial u} & \frac{\partial y}{\partial v} & \frac{\partial y}{\partial n} \\ \frac{\partial z}{\partial u} & \frac{\partial z}{\partial v} & \frac{\partial z}{\partial n} \end{bmatrix}, \tag{3.10}$$

where $\underline{\underline{\boldsymbol{\Lambda}}}$, depends on the particular patch geometry.

2) Next, LPF functions are defined on the parametric flat domain as for flat surfaces

$$\mathbf{J}'(\mathbf{r}') = \sum_{n,m} \alpha_{n,m,p}\mathbf{f}_{n,m,p}(\mathbf{r}') \quad f_{n,m}(\mathbf{r}') = \exp\left(-j\left(k_u^{n,m}u + k_v^{n,m}v\right)\right)W(u,v) \tag{3.11}$$

The sufficient and non-redundant number of functions is found by solving the local dispersion equation

$$\left[\underline{\underline{\mathbf{K}}}\cdot\underline{\underline{\boldsymbol{\mu}}}^{-1} + \omega^2\underline{\underline{\boldsymbol{\varepsilon}}}\cdot\underline{\underline{\mathbf{K}}}^{-1}\right]\cdot\tilde{\mathbf{E}}(\mathbf{k}) = 0 \quad , \qquad [K] = \begin{bmatrix} 0 & -k_n & k_v \\ k_n & 0 & -k_u \\ -k_v & k_u & 0 \end{bmatrix} \tag{3.12}$$

and using (locally) the spectral domain completeness relationship introduced for the flat case.

3) Finally, the back-transformation from flat anisotropic to curved isotropic space yields the BFs for the curved patch.

$$\mathbf{J}(\mathbf{r}_S) = \sum_{\substack{n,m=-\infty \\ k=1,2}}^{\infty} \alpha_{n,m,p}\mathbf{f}_{n,m,p}(\mathbf{r}_S) \qquad f_{n,m,p}(\mathbf{r}_S) = \frac{\left|\underline{\underline{\boldsymbol{\Lambda}}}^{T}\cdot\hat{n}\right|}{\det[\Lambda]} f_{n,m}\left(\boldsymbol{\Gamma}^{-1}(\mathbf{r}_S)\right) \tag{3.13}$$

The number of BFs so obtained matches the degrees of freedom of the field known in literature [3.25]. Numerical results confirm the effectiveness of the representation for both fields and currents. The case of a NURBS surface is shown in Fig.3.18.

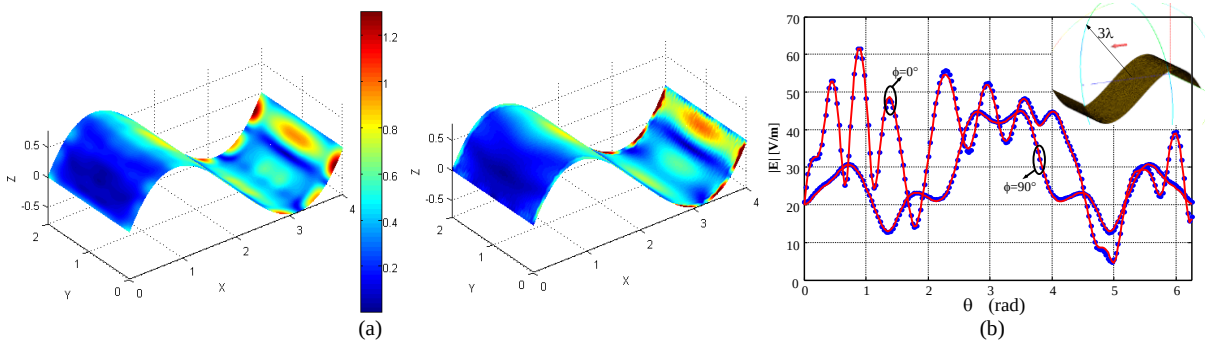

Figure 3.18(a) Comparison between induced current on a NURBS surface illuminated by en electric dipole botained by SBF expansion and reference solution obtained by a MoM (FEKO). (b) Field scattered versus aspect angle q in radians. Comparison between the field radiated by the reconstructed SBF currents (continuous line) and the reference solution obtained by a MoM (dots)

References

[3.18] L. Matekovits, G. Vecchi, G. Dassano, and M. Orefice, "Synthetic function analysis of large printed structures: The solution space sampling approach," in IEEE AP-S Soc. Int. Symp., Boston, MA, Jul. 2001, pp. 568–571.

[3.19] S E. Suter and J. Mosig, "A subdomain multilevel approach for the MoM analysis of large planar antennas," Microw. Opt. Technol. Lett., vol. 26, no. 4, pp. 270–277, Aug. 2000.

[3.20] V. S. Prakash and R. Mittra, "Characteristic basis function method: A new technique for fast solution of integral equations," Microw. Opt. Technol. Lett., pp. 95–100, Jan. 2003

[3.21] L. Matekovits, V. A. Laza and G. Vecchi, Analysis of Large Complex Structures with the Synthetic-Functions Approach, *IEEE Trans Antennas and Propagat*., vol. 55, no. 9, pp. 2509-2521, Sept. 2007.

[3.22] D. H. Kwon, and D. H. Werner, "Transformation Electromagnetics: An Overview of the Theory and its Application," IEEE Antennas and Propagation Magazine, Vol. 52, No. 1, pp. 24-46, Feb. 2010.

[3.23] A. J. Ward and J. B. Pendry, "Refraction and geometry in Maxwell's equations", J. of Modern Optics, Vol.43, n.4, pp.773-793, 1996.

[3.24] A. Nicolet, F. Zolla and Y. Ould Agha, "Geometrical transformations and equivalent materials in computational electromagnetism", COMPEL: The international Journal for Computation and Mathematics in Electrical and Electronic Engineering, Vol.27, N.4, 2008.

[3.25] O.M. Bucci and G. Franceschetti "On the Degree of Freedom of Scattered Fields", IEEE Trans Antennas and Propagat., vol. 37, no. 7, pp. 918-926, Jul. 1989.

3.3.2 Efficient beam expansion of the field radiated by apertures

State of the art at the period of the research

A number of different beams have been introduced in literature: Gaussian beams (GB) [3.26], Gaussian-ray basis functions (GRBF) [3.27], higher-order Gauss-Laguerre (GLB) or Gauss-Hermite (GHB) beams [3.28],[3.29], CSP, Bessel Beams (BB) [3.30] . GBs have the limitation of satisfying Maxwell's equations only in the paraxial region; however, they desirably do not possess branch singularity in space. GRBF are obtained from GB by introducing an empirical extra parameter, with the aim to control beam width at a given distance from the source. GL or GH beams deal with expansions around a preferred axis of propagation with higher-order terms representing the off-axis variations. They have the advantage of constituting an orthogonal set, and therefore are often used as basis for a mode matching technique. However, their descriptive capability is still restricted to the paraxial region. To expand the field in the whole space, CPS beams represents a good solution.

In Gabor-type (phase-space) expansions [3.31], the field is expanded using a lattice of beams emerging from a set of points in the aperture plane and propagate from each point in a 2D lattice of directions. These beams describe the local radiation properties of the aperture distribution; the beam amplitudes are determined by the local radiation properties (the local spectrum) of the aperture near the lattice points. The difficultly of the implementation resides in the optimal choice of the spatial (space lattice points) and spectral (angular beam density) resolutions.

Research goal

The main goal of this research work has been the derivation of a new *automatic procedure* for the beam expansion of the field radiated by an aperture *valid in the whole space*.

Proposed solution

I have contributed to the introduction of two new types of beams with cylindrical symmetry. They are exact solution of Maxwell equation with closed form expressions in both space and spectral domains. In addition, their formulations are found to be very accurate for expanding in beams the field generated by generic apertures (circular, rectangular; etc.).

- FORMULATION A

In this case, the proposed beams are generated in a natural way starting from the spectral-domain radiation integral written in cylindrical coordinates

$$I = \frac{1}{8\pi^2 j}\int_0^{\infty}\int_0^{2\pi} \tilde{g}\left(k_\rho,\alpha\right) e^{-j\rho k_\rho \cos(\alpha-\phi)} \frac{e^{-jz\sqrt{k^2-k_\rho^2}}}{\sqrt{k^2-k_\rho^2}} k_\rho \, d\alpha dk_\rho \,, \tag{3.14}$$

where $\tilde{g}\left(k_\rho,\alpha\right)$ denotes an aperture spectrum of either electric or magnetic field or of a scalar potential, while $e^{-jzk_z}/k_z ; k_z = \sqrt{k^2-k_\rho^2}$, is the spectral-domain representation of the free-space Green's function.

Due to the inherent periodicity in α, the aperture plane in a Fourier series, $\tilde{g}\left(k_\rho,\alpha\right)$ can be expanded in a Fourier series $g\left(k_\rho,\alpha\right) = \sum_{n=-\infty}^{\infty} c_n\left(k_\rho\right) e^{-jn\alpha}$ and the integral in α in (3.14) can be evaluated in a closed form, yielding:

$$I = \frac{(-j)^{n+1}}{4\pi}\sum_{n=-\infty}^{\infty} e^{-jn\phi}\int_0^{+\infty} c_n\left(k_\rho\right)\frac{e^{-jz\sqrt{k^2-k_\rho^2}}}{\sqrt{k^2-k_\rho^2}} \mathrm{J}_n\left(\rho k_\rho\right) k_\rho dk_\rho \,, \tag{3.15}$$

where J_n is the Bessel function of *n*-th order.

The coefficients $c_n\left(k_\rho\right)$ are represented by the Generalized Pencil of Function (GPOF) method [3.32] as

$$c_n\left(k_\rho\right) = \sum_{m=1}^{M} d_{mn} e^{b_{mn}\sqrt{k^2-k_\rho^2}}, \tag{3.16}$$

where d_{mn} and b_{mn} are the output residues and poles of the GPOF algorithm. Using (3.16) in (3.15) leads to

$$I = \sum_n \sum_{m=1}^{M} a_{mn} W_n(\rho, \phi, z + jb_{mn}), \quad W_n\left(\rho, \phi, \tilde{z}\right) = e^{-jn\phi} \int_0^{\infty} \frac{e^{-j\tilde{z}\sqrt{k^2 - k_\rho^2}}}{\sqrt{k^2 - k_\rho^2}} J_n\left(\rho k_\rho\right) k_\rho dk_\rho . \tag{3.17}$$

In (3.17), W_n possess a recursive closed form and it is evaluated at a point whose *z*-coordinate has been displaced in the complex plane by jb_{mn}. Eq. (3.17) is the defining equation of the wave object that we shall refer to as the Complex Conical beam (CCB-A), for their cylindrical symmetry.

The procedure outlined here permits the calculation of the beam expansion provided that the aperture Fourier spectrum $\tilde{f}\left(k_x, k_y\right)$ is available. The latter should not necessarily be known in analytical form, but can also be obtained through a FFT of space field samples.

- FORMULATION B

An alternative formulation has been obtained starting from the aperture field spectrum (3.14) and multiplying and dividing the integrand by $\left(k_\rho / k\right)^{|n|}$. One of these two factors is included in the Fourier expansion yielding the coefficients $c_n\left(k_\rho\right)$ defined by (3.16). The subsequent GPOF expansion is *n*-dependent

$$q_n\left(k_\rho\right) = \sum_{m=-M}^{M} d'_{mn} e^{b'_{mn}\sqrt{k^2 - k_\rho^2}}, \tag{3.18}$$

because $q_n\left(k_\rho\right) = c_n\left(k_\rho\right)\left(k / k_\rho\right)^{|n|}$.

The initial radiation integral, as in the first case, reduces to the double sum

$$I = \sum_n \sum_{m=1}^{M} a'_{mn} \Psi_n(\rho, \phi, jb'_{mn} + z), \; a'_{mn} = (-j)^{n+1} \frac{1}{4\pi} d'_{mn}, \; \Psi_n\left(\rho, \phi, z\right) = e^{-jn\phi} \int_0^{\infty} \frac{e^{-jz\sqrt{k^2 - k_\rho^2}}}{\sqrt{k^2 - k_\rho^2}} J_n\left(k_\rho \rho\right) \left(\frac{k_\rho}{k}\right)^{|n|} k_\rho dk_\rho . \tag{3.19}$$

A closed form solution to this integral has been obtained as

$$\Psi_n\left(\rho, \phi, \tilde{z}\right) = e^{-jn\phi} k \frac{\rho^n}{\left(\tilde{z}^2 + \rho^2\right)^{n/2}} \sqrt{\frac{\pi}{2k\sqrt{\tilde{z}^2 + \rho^2}}} \, \mathrm{H}^{(2)}_{n+1/2}\left(k\sqrt{\tilde{z}^2 + \rho^2}\right) = e^{-jn\phi} k \sin^n \tilde{\theta} \, \mathrm{h}_n^{(2)}\left(k\tilde{r}\right), \tag{3.20}$$

where $\mathrm{h}_n^{(2)}\left(k\tilde{r}\right)$ is the spherical Hankel function of the second kind and $\sin\tilde{\theta} = \tilde{z} / \tilde{r}$. The solution for negative orders *n* is again obtained as $\Psi_{-n}\left(\rho, \phi, \tilde{z}\right) = (-1)^n e^{j2n\phi} \Psi_n\left(\rho, \phi, \tilde{z}\right)$. Eq. (3.20) is the defining equation of the wave object that we shall refer to as the Complex Conical Beam of type B (CCB-B).

One can also notice that the new wave objects denoted by Ψ_n constitute a special subset of the classical spherical harmonics ψ_{mn} when $m = n$; namely

$$\Psi_n\left(\rho, \phi, \tilde{z}\right) = \psi_{nn}\left(\tilde{r}, \tilde{\theta}, \phi\right) = e^{-jn\phi} P_n^n\left(\cos\tilde{\theta}\right) \mathrm{h}_n^{(2)}\left(k\tilde{r}\right). \tag{3.21}$$

It is worth noting that for *n*=0, we again obtain a complex source point

$$\Psi_0\left(\rho, \phi, \tilde{z}\right) = W_0\left(\rho, \phi, \tilde{z}\right) = j \frac{e^{-jk\tilde{r}}}{\tilde{r}} \tag{3.22}$$

Two examples of expansion of the radiated field by an aperture are shown in Figs. 3.19-3.20. A circular aperture with radius $r_w = 4\lambda$ illuminated by a TM_{44} mode is considered in Fig. 3.19. A total of 64 and 52 CCB's have been automatically generated by the GPOF procedure to represent the field. Fig.3.19a presents successful comparative results obtained using both formulations A and B; the reference solution is provided by the direct integration of (3.14). Fig. 3.19b presents the absolute errors between normalized fields. Figures 3.20a-b present a comparison between the electric field radiated by a rectangular aperture of dimensions $5\lambda x 2\lambda$ with uniform aperture field (both phase and amplitude) obtained: using the Gauss-Hermite expansion, CCB type A and B and the reference solution provided by the direct integration, in two principal planes.

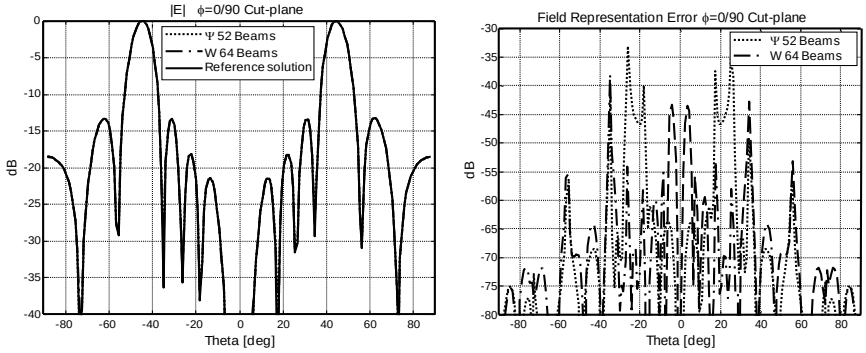

(a) (b)

Figure 3.19. a) E-plane (ϕ = 0) and H-plane (ϕ = 90º) cuts of the radiated total electric field magnitude by a TM_{44} circular waveguide mode, sampled on a sphere of radius 300λ; b) Corresponding field representation error.

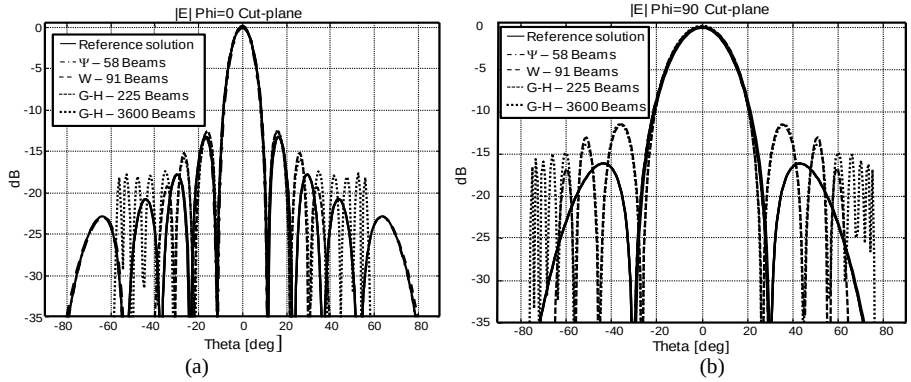

(a) (b)

Figure 3.20. a) E-plane (ϕ = 0) and b) H-plane (ϕ =90) cuts of the total electric field magnitude radiated by a 5x2λ phased rectangular aperture, sampled on a sphere of radius 300λ.

References

[3.26] G.A. Deschamps, "The Gaussian Beam as a Bundle of Complex Rays", Electronics Letters, vol. 7, No. 23, 1971, pp. 684-685

[3.27] H-T. Chou, P. H. Pathak, and R. J. Burkholder, "Application of Gaussian-ray Basis Functions for the Rapid Analysis of Electromagnetic Radiation from Reflector Antennas", IEE Proc. Microw. Antennas Propagat., vol. 150, 2003, pp. 177-183

[3.28] W.A. Imbriale and D.J. Hoppe, "Recent Trends in the Analysis of Quasioptical Systems", Proc. Millenium Conference on Antennas and Propagation, Davos, Switzerland, 2000.

[3.29] S. Withington, J.A. Murphy and K.G. Isaak, "Representation of Mirrors in Beam Waveguides as Inclined Phase-Transforming Surfaces", Infrared Phys. Technol., vol. 36, no. 3, Apr. 1995, pp. 723-734.

[3.30] L. B. Felsen, "Complex-Source-Point Solutions of the Field Equations and their Relation to the Propagation and Scattering of Gaussian Beams", in Proc. Symp. Math, vol 18, 1975, pp. 39-56

[3.31] A. Shlivinski, E. Heyman, A. Boag, and C. Letrou, "A Phase-Space Beam Summation Formulation for Ultrawide-Band Radiation: A Multiband Scheme", *IEEE Trans. Antennas Propagat.*, Vol. 52, No. 8, pp. 2042-2056, Aug 2005.

[3.32] T. K. Sarkar and O. Pereira, "Using the Matrix Pencil Method to Estimate the Parameters of a Sum of Complex Exponentials", IEEE Antennas and Propagation Magazine, vol. 37, no. 1, Feb. 1995, pp. 48-55.

3.3.3 Planar metasurface structures

Introduction

Metasurfaces constitute a class of thin meta-materials, which are used from microwave to optical regime to create new antennas and microwave devices.

Proposed solution

In this context I have proposed the use of impedance surfaces for transforming surface or guided waves into a different configuration of wave-field with desirable properties. These surfaces have been obtained by an appropriate synthesis of inhomogeneous surface impedance that allow a local modification of the dispersion equation and, at constant operating frequency, of the local wave-vector. Two innovative solutions have been implemented:

- Section (A) presents a highly directive *H*-plane antenna with a Luneburg lens inside a Parallel Plate Waveguide.
- Section (B) presents a new kind of spiral antennas.

(A) Highly directive H-plane Luneburg lens antenna

State of the art and motivation at the period of the research

Traditional dielectric lenses, manufactured using several layers of various dielectrics with appropriate profiles are still very expensive due to complex manufacturing process. Furthermore, in order to achieve a relatively smooth refractive index variation a large number of dielectric layers are needed making the whole process even more complicated. Planar metasurface lenses are low profile and easier to fabricate compared to standard dielectric lenses, thus offering advantages for new communication antennas and sensor applications. Moreover the variation of the surface impedance that corresponds to the refractive index can be made practically continuous since a large number of layers/pixels can be used.

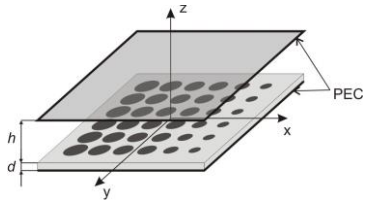

Figure. 3.21 Printed circular patches on a dielectric substrate inside a parallel-plate waveguide. Changing the patch radii controls the equivalent inhomogeneous surface impedance.

Proposed solution

A highly directive *H*-plane antenna using a Luneburg lens has been designed. The lens effect has been obtained by changing the effective permittivity of the dielectric inside a parallel plate waveguide by varying the equivalent boundary conditions of one wall of the parallel plate waveguide, as shown in Fig.3.21. The final effect of changing the boundary condition on one wall of the parallel plate waveguide is equivalent to changing the local dispersion and phase velocity. This effect allows to modify the global wave-front as it occurs in a solid dielectric lenses with variable refraction index.

A dielectric slab with printed circular patches of variable radii has been placed on top of one wall of an ideal infinite parallel-plate waveguide (PPW) structure. The wave-number along a generic ρ coordinate (parallel to the metallic plates) associated to a propagating TM mode has been interpreted as the product between the free-space wavenumber k and an equivalent refractive index n_{eq} , namely

$$k_\rho = \sqrt{k^2 - k_z^2} = k\sqrt{1-\left(k_z^2/k^2\right)} = kn_{eq}\,, \tag{3.23}$$

where $n_{eq} = \sqrt{1-\left(k_z/k\right)^2}$ and k_z is the wavenumber along z. It is evident from (3.23) that in order to have a refractive index $n_{eq} > 1$, k_z should be imaginary, that is the guided mode in the PPW has to be evanescent along the z direction. For TM polarization, assuming that each patch is embedded in a locally uniform periodic lattice, the transverse resonance dispersion equation is obtained by solving the equivalent circuit in Fig. 3.22a, where the patch-texture is effectively represented by the impedance Z_s^{TM} on one side of a short circuited TM transmission line. This impedance, which depends on the local radius of the local patches, is obtained using the pole-zero matching method, presented in Section 3.1, with a MoM analysis.

The solution of the transmission line resonance in Fig. 3.22a is simply obtained by using the transverse resonant technique, namely

$$Z_S^{TM} + jZ_0^{TM}\tan\left(k_z h\right) = 0\,, \tag{3.24}$$

where $Z_0^{TM} = \zeta k_z/k$, ζ is the free space impedance, h is the height of the parallel-plate waveguide from the top of the patches to the upper plate and Z_s^{TM} is the effective surface impedance of the patch layer.

A Luneburg lens possesses the property to focus parallel rays into a single point on the lens edge, or reciprocally, to transform radial rays from a point source at the lens edge into parallel rays at the exit from the lens. This effect can be used to design a high-gain antenna with very good scanning properties. The lens is defined by the law $n_{eq}(\rho) = \sqrt{2-\left(\rho/R\right)^2}$, where ρ is the radial coordinate and R is the radius of the lens.

This impedance profile needed to synthesize the lens has been obtained from (3.24) as

$$\frac{X_s}{\zeta} = \sqrt{1-\left(\rho/R\right)^2}\tanh\left(kh\sqrt{1-\left(\rho/R\right)^2}\right). \tag{3.25}$$

A lens designed at a center frequency of 13 GHz, with a radius R = 75.6 mm, placed in a parallel-plate waveguide with a height h = 1.8 mm is shown in Fig.3.22c. The dielectric substrate has permittivity ε_r = 10.2 and

thickness d = 0.7 mm. The final antenna layout is shown in Fig. 3.23a. Fig. 3.23b shows the field inside the lens, while Fig. 3.23c shows the radiation patterns in the H plane at several frequencies. The essential benefit of this kind of antenna lies in the simplicity of the realization compared to standard dielectric lens antennas.

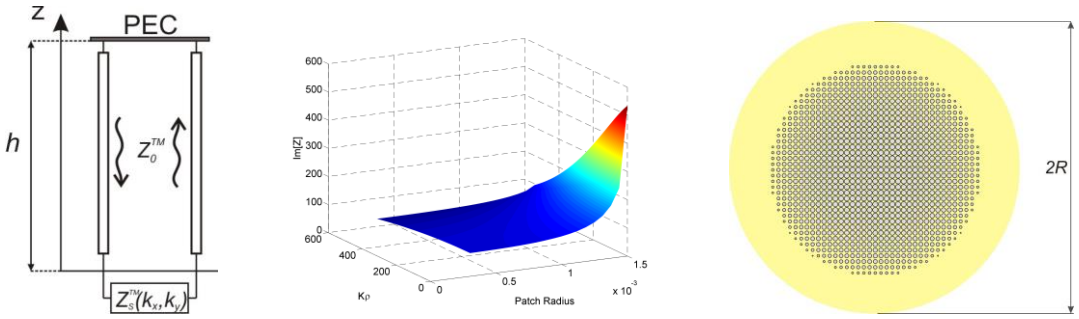

(a) (b) (c)

Figure 3.22 (a) Equivalent circuit defining the surface impedance for TM_z polarization, where $Z_0^{TM} = \zeta k_z / k$. (b) Impedance values obtainable using different patch radii with respect to the $k_\rho = k n_{eq}$. Dielectric substrate with permittivity ε_r = 10.2 and thickness d = 0.7 mm, pixel size is 3.15 mm and minimum spacing between the patches is 0.3 mm. (c) Array of circular patches with the surface impedance profile corresponding to the Luneburg lens (pixel size is 3.15 mm and minimum spacing between the patches is 0.3 mm).

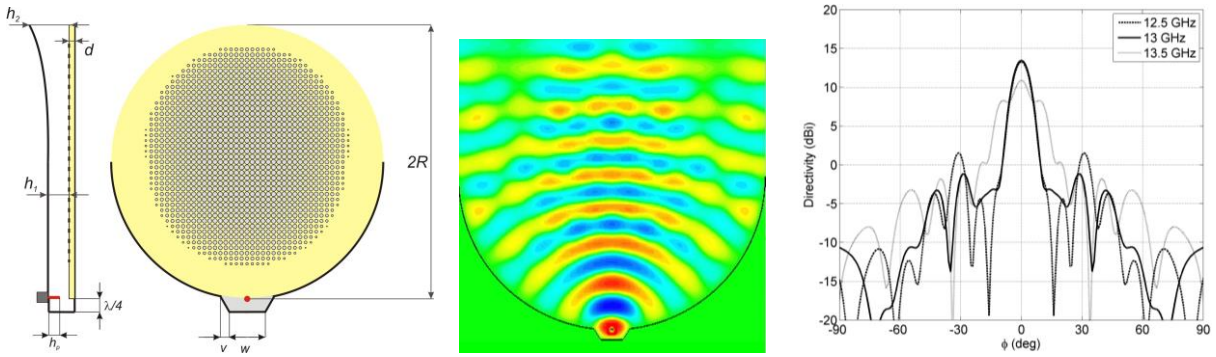

(a) (b) (c)

Figure 3.23 (a) geometry of the designed antenna with the exponential change in the waveguide height (h_1 = 2.3 mm, h_2 = 5.75 mm), (b) snapshot of the simulated E_z field above the patches, (c) farfield patterns in the H-plane.

(B) Spiral leaky-wave antennas based on modulated surface impedance

State of the art and motivation at the period of the research

The antennas presented here are completely different from conventional spiral antennas based on the active region concept.

Proposed solution

A new typology of planar circularly polarized leaky wave (LW) antennas excited by a single-point feed has been developed. The basic structure is constituted by variable, spiral-shape modulated metasurface.

A vertical probe excites a cylindrical surface wave (SW) on the impedance surface, and the latter converts it into a circularly polarized LW. To illustrate the phenomenology, a vertical dipole is used; however, more effective feeds may be adopted in practical realizations. The vertical elemental dipole with moment $I_0 \Delta z$ is placed on an infinite plane at z=0. We assume that the latter is subjected to the impedance boundary condition

$$j\bar{X}_s \left(\mathbf{z} \times \mathbf{H}_t\right)\Big|_{z=0} = \mathbf{E}_t\Big|_{z=0}, \tag{3.26}$$

where $\bar{X}_s$ is a positive reactance, and $\mathbf{E}_t, \mathbf{H}_t$ are the transverse-to-z components of the electric and magnetic fields, respectively. The dipole excites on the reactive surface a TM_0-type SW which at a certain distance from the dipole has the following tangent electric field (z=0)

$$\mathbf{E}_t\big|_{z=0} = j\bar{X}_s \mathbf{J}_{sw}, \qquad \mathbf{J}_{sw} = J_{sw} H_1^{(2)}\left(\beta_{sw}\rho\right)\boldsymbol{\rho}, \tag{3.27}$$

where $H_1^{(2)}$ is the Hankel functions of second kind of first order and the radial propagation constant $\beta_{sw} > k$ respects the dispersion equation

$$\beta_{sw} = k\sqrt{1+\bar{X}_s^{\,2}/\zeta^2}; \quad \alpha_z = \sqrt{\beta_{sw}^2 - k^2} = \frac{k}{\zeta}\bar{X}_s \quad , \tag{3.28}$$

where α_z is the attenuation constant in the z direction.

The reactance $\bar{X}_s$ is shaped as a sinusoidal Archimedean spiral

$$X_s(\rho,\phi) = \bar{X}_s\left[1 + M\sin\left(\beta_{sw}\rho - \varphi\right)\right], \tag{3.29}$$

where $\bar{X}_s$ represents the average values of the impedance. Its radial period is equal to the wavelength of the SW excited on an equivalent homogeneous surface impedance. The constant *M* is the *impedance modulation index.* The (-1) indexed wavenumber of the relative mode of the Floquet decomposition of the tangential field, belongs to the visible region of the aperture radiation and leads to an almost broadside beam. An analytical approximation of the radiated field has been derived. Universal curves for antenna design have been also obtained (Fig. 3.24) and a design procedure outlined. Two types of practical solutions are presented, which are relevant to different implementation of the impedance modulation:

i) a grounded dielectric slab with a spiral-sinusoidal thickness (Figure 3.25a)

ii) a texture of dense printed patches with sizes variable with a spiral-sinusoidal function (Figure3.25b).

Full wave results are compared successfully with the analytical approximations (Figs 3.26-3.27). Both the layouts represent good solutions for millimeter wave circular polarized antennas. Our solutions exhibit high-gain (20-25 dB) and moderate bandwidth (10%) in contrast with conventional spiral antennas, characterized by broad bandwidth and low gain.

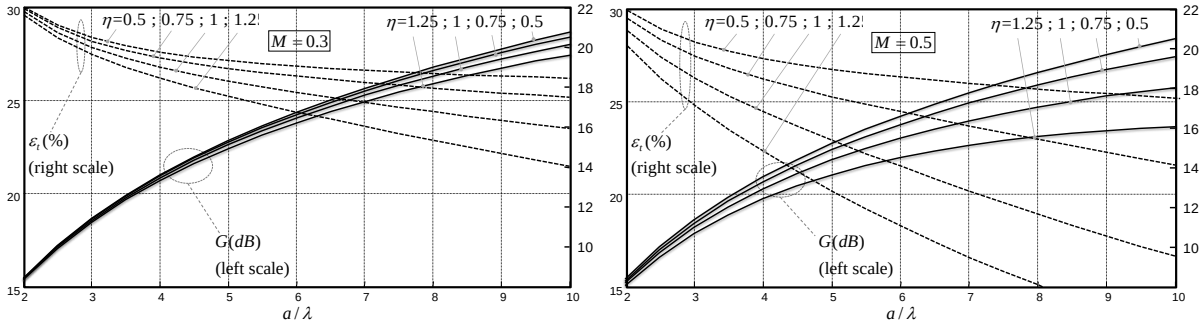

Figure. 3.24. Design curves of gain (G) and efficiency (ε_t) as a function of the aperture radius in free-space wavelengths for $\eta = \bar{X}_s/\zeta \in (0.5-1.5)$. (a) *M*=0.3 and (b) *M*=0.5

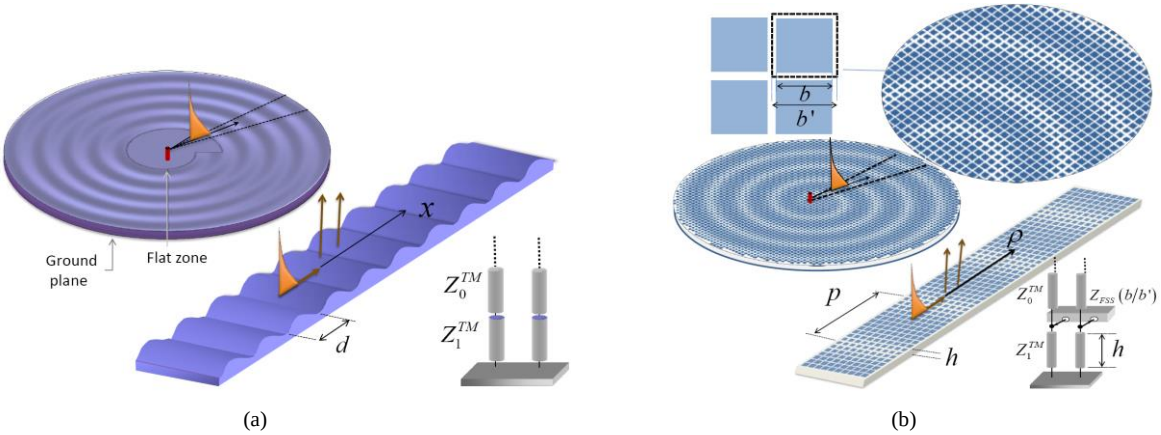

Figure 3.25 Dielectric spiral antenna with modulated thickness, its local 2D problem, and the equivalent transmission line model for the TM dominant surface wave. (b) Printed patch antenna with its local 2D problem and the equivalent transmission line model for the TM dominant surface wave. For both cases $Z_0^{TM} = \zeta k_z/k, Z_1^{TM} = \zeta_1 k_z/k_1$

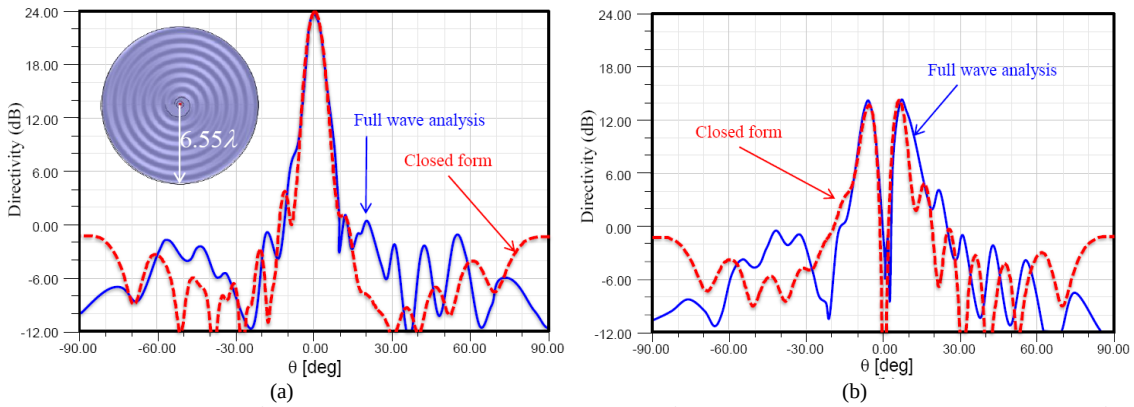

Figure 3.26 Directivity diagrams for co-polar (a) and cross polar (b) components for the 24dB gain antenna at 18 GHz. The results from the full-wave analysis (no absorbing boundary condition at the termination, continuous line) are compared with those from the closed form solution shown in (11)-(15) (dashed lines).

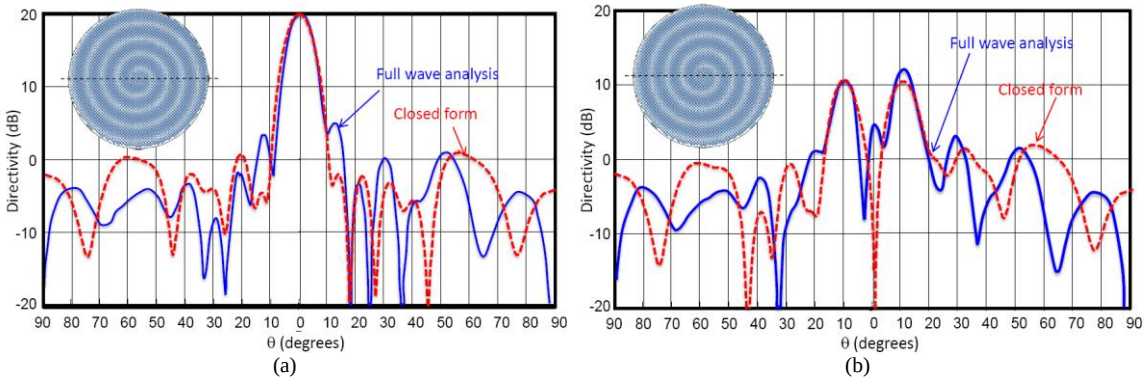

Figure 3.27 Directivity diagrams for co-polar (a) and cross polar (b) components for the 20dB gain antenna at 13 GHz. The results from the full-wave analysis (continuous line) are compared with those from the closed form solution.

3.4. Post-Doc frame-time II (November 2010 – August 2013)

During the post-doc fellowship at IETR, Université de Rennes 1, my research activity have been focused on two different topics:

- Analysis and design of complex substrate integrated waveguide (SIW) structures, described in Section 3.4.1
- Fast analysis and design of quasi-optical integrated imaging-like systems. The beam expansion method introduced in Part II in association with a Physical Optic approximation has been used for the analysis and the design of a novel wide scanning antenna based on an imaging-like system.

***List of related publications*: [P.18], [P.20]-[P.21], [IC.4]-[IC.6], [C.33], [C.36]-[C.55].**

3.4.1 Analysis and design of complex substrate integrated waveguide (SIW) structures

Introduction

Substrate Integrated Waveguides (SIW) have been introduced recently to provide a means to create waveguide based, high frequency circuits at low cost. They are realized using standard printed circuit board (PCB) technology which is easy and cheap to produce. The basic idea consists in realizing waveguide channels on a grounded dielectric slab by using arrays of metallic vias. SIW technology maintains the advantage of metallic waveguides in addition with the possibility to integrate typical of microstrip structures, allowing sophisticated packaging technology and the integration of complex beam-forming networks and antennas on the same board.

State of the art and motivation

The analysis of the propagation in SIW configurations has been carried out in many ways; however because of the presence of vias fence which form the lateral walls of the waveguide, a finite difference of finite element type of solution needs to be often employed. Thus the design of real device using quasi-optical system (electrically very large structures) can be time consuming and memory demanding.

Proposed solution

The work has been performed in two successive steps. In the first step, the field inside the waveguide structure has been efficiently computed by considering the dyadic Green's function of the PPW expressed as an expansion in terms of vectorial cylindrical eigenfunctions. The primary dyadic Green's function can be obtained from two scalar functions ℓ' and ℓ'' representing respectively the TM a TE components with respect to the z axis direction as

$$-j\omega\mu\underline{\underline{\mathbf{G}}}^{(1)}(\mathbf{r},\mathbf{r}') = k^2(\nabla\times\hat{\mathbf{z}})(\nabla'\times\hat{\mathbf{z}})\ell'(\mathbf{r},\mathbf{r}') + (\nabla\times\nabla\times\hat{\mathbf{z}})(\nabla'\times\nabla'\times\hat{\mathbf{z}})\ell''(\mathbf{r},\mathbf{r}') - \left(\hat{\mathbf{z}}\hat{\mathbf{z}} + \frac{\nabla_t\nabla_t}{\nabla_t^2}\right)\delta(\mathbf{r}-\mathbf{r}'), \quad (3.30)$$

where $k=\sqrt{\varepsilon\mu}$, ∇ and ∇' denote a gradient operator with respect to observation location and source location, respectively and ∇_t denotes the transverse gradient operator.

The scalar functions introduced above are related to the scalar wave equation subjected to TM or TE boundary conditions on the PEC plate surface, respectively. Solving the wave equations in cylindrical coordinates using a radial waveguide representation, end imposing boundary conditions on the metal plates, yelds:

$$\underline{\underline{\mathbf{G}}}^{(1)}(\mathbf{r},\mathbf{r}') = -\left(\hat{\mathbf{z}}\hat{\mathbf{z}} + \frac{\nabla_t\nabla_t}{\nabla_t^2}\right)\delta(\mathbf{r}-\mathbf{r}') - \sum_{m=0}^{+\infty}\sum_{n=-\infty}^{\infty}(-1)^n\left(1-\frac{\delta_{m0}}{2}\right)\frac{k}{2\omega\varepsilon k_{\rho_m}^2 h}\begin{bmatrix}\mathbf{M}_n(k_{\rho_m},k_{z_m},\boldsymbol{\rho},z)\mathbf{M}_n'(k_{\rho_m},k_{z_m},\boldsymbol{\rho}',z')\\ +\mathbf{N}_n(k_{\rho_m},k_{z_m},\boldsymbol{\rho},z)\mathbf{N}_n'(k_{\rho_m},k_{z_m},\boldsymbol{\rho}',z')\end{bmatrix}, \quad (3.31)$$

where δ_{m0} is the Kronecker's delta function, $\mathbf{M}_n$, $\mathbf{N}_n$ are cylindrical vectors eigenfunctions.

In the second step the field scattered by the vias has been introduced. A structure composed by N_p vias centered at $\boldsymbol{\rho}_1,\boldsymbol{\rho}_2,\ldots,\boldsymbol{\rho}_{N_p}$ and an exciting magnetic source $\mathbf{M}_s$ has been considered. The scattered field from each via has been expressed as a linear superposition of cylindrical wave as

$$\mathbf{H}_s(\mathbf{r}) = \sum_{p=1}^{N_p}\sum_{m=1}^{+\infty}\sum_{n=-\infty}^{+\infty} A_{m,n,p}^{TM}\mathbf{M}_n(k_{\rho_m},k_{z_m},\boldsymbol{\rho}-\boldsymbol{\rho}_p,z) + A_{m,n,p}^{TE}\mathbf{N}_n(k_{\rho_m},k_{z_m},\boldsymbol{\rho}-\boldsymbol{\rho}_p,z). \quad (3.32)$$

The scattered field amplitudes $A_{m,n,p}^{TM}$, $A_{m,n,p}^{TE}$ have been determined by imposing the boundary conditions on the surface of each via, namely

$$\hat{\mathbf{n}}_q\times(\mathbf{E}_{inc}+\mathbf{E}_s)\big|_{|\boldsymbol{\rho}-\boldsymbol{\rho}_q|=a_q} = \hat{\mathbf{n}}_q\times\mathbf{E}_{\text{int}}, \quad \hat{\mathbf{n}}_q\times(\mathbf{H}_{inc}+\mathbf{H}_s)\big|_{|\boldsymbol{\rho}-\boldsymbol{\rho}_q|=a_q} = \hat{\mathbf{n}}_q\times\mathbf{H}_{\text{int}}, \quad (3.33)$$

where $\hat{\mathbf{n}}_q$ is the normal unit vector to the surface and a_q is the radius of the via.

Since the scatterer is conformal to the coordinate system, (3.33) can be solved separately for the TM and TE polarization. Using (3.32) in (3.33) and with the help of the Bessel summation theorem a couple of matrix equations have been obtained and solved. The theory developed during the activity has been implemented in a Matlab code and validated by full-wave simulation with a commercial software (HFSS^{TM}). An extremely good agreement is obtained for all cases at a reduced computational time and memory occupation. As examples Fig. 3.28b reports the comparison of the transmission characteristics of the phase shifter represented in Fig. 3.28a while Fig. 3.29b those relevant to the coaxially fed low-reflection waveguide corner shows in Fig.3.29a. In Table I, CPU time for the considered cases are reported and compared to those needed to HFSS. The improvement of the proposed method is stunning.

CPU SIMULATION TIME ON A XEON E5540 2.83GHZ WITH 16GBYTE RAM

Structure	Number of metallic /dielectric posts	HFSS		This paper
		Mesh	Freq. Point	
R. h. corner	100 / 1	306 s.	83 s.	15.2 s
Phase shifter	38 / 27	234 s.	117 s.	19.5 s.

TABLE I

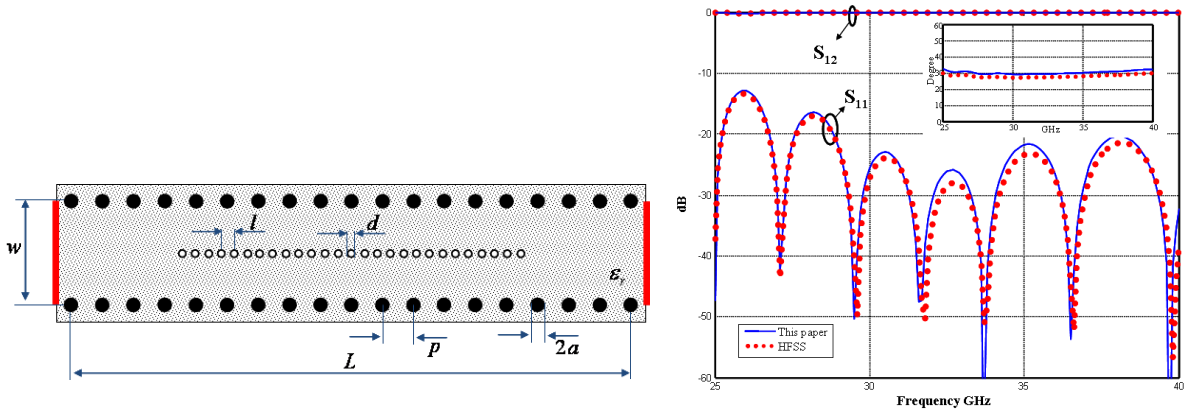

(a) (b)

Figure 3.28. (a) Phase shifter with 27 air holes. ε_r=2.2, h=0.254mm, p=1.6mm, a=0.4mm, L=28.8mm, l=0.669mm, d=0.4mm. (b) S-parameters for a phase shifter (Fig. 12) with 27 air holes. In the inset, comparison between the simulated phase obtained with the proposed method and numerical results obtained with HFSS.

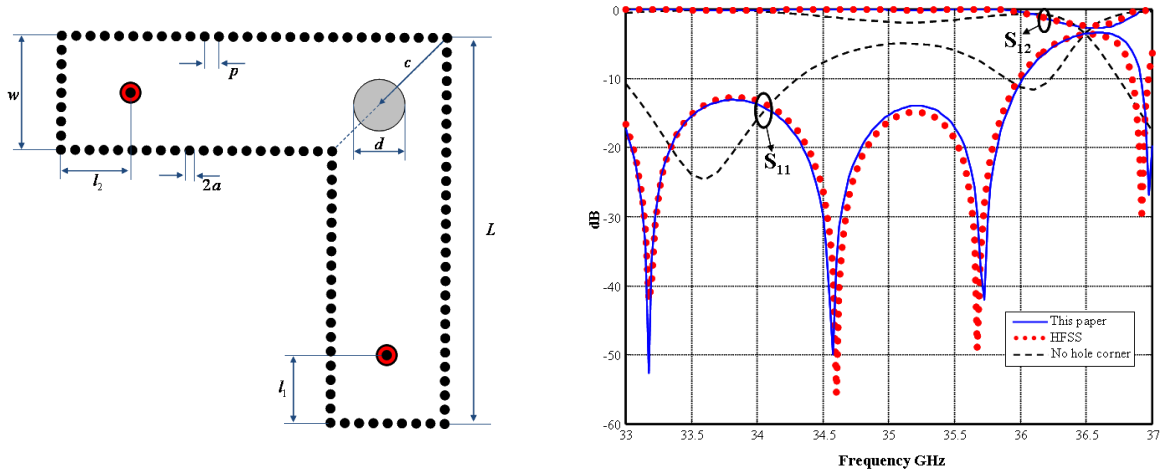

(a) (b)

Figure 3.29. (a) Geometry of the low-reflection right-angled corner. ε_r=2.2, h=1mm, p=0.65mm, a=0.2mm, L=17.6mm, l_1=l_2=3.2mm, d=2mm. (b) Comparison between the magnitudes of the S-parameters for the low-reflection right-angled corner obtained with the proposed method (blue line) and HFSS (red dots). The S-parameter for the corner structure without the air hole is also reported (black dashed line).

Chapter 4 : Present and future research activity

Since my master internship in 2003, I have acquired different research-oriented skills thanks to the different people I have met during my career. My research project for the coming years described in this chapter, intends to take benefit of these different skills (i.e., antennas, numerical methods, and metamaterials) in order to propose an original approach for current challenges in electromagnetic engineering.

My main research project deals with the development of analytical and numerical methods for the implementation of planar aperture field antennas.
Planar antennas have the attractive features of low profile and small size. They are become very popular because of their low cost and ease of fabrication, and easy integration with circuit components. In fact, printed antennas are inexpensive to fabricate using modern printed circuit technology, and are conformal to planar and non-planar surfaces. Moreover, these antennas can be easily mounted on the surface of trains, aircrafts, satellites, and even on handheld mobile devices.
Aperture field theory establish an easy and direct link between the desired antenna radiation properties (radiation pattern, polarization, etc.) and the continuous field distribution needed on the aperture of the antenna. The main challenge is the physical implementation of such ideal field.
The goal of the research activity is to develop a global methodology composed by different sub blocks for the aperture field reconstruction using planar structures as metasurfaces, slot antennas and shaped reflectors in order to take advantage of the aperture field optimization methods. This project represents the natural junction between the different activities I have been working on since my position at Sorbonne University in 2013.

A secondary and parallel activity dealing with the numerical modelling of complex natural environment is also presented in Sect 4.2.

4.1 Analytical and numerical methods for aperture field planar antennas

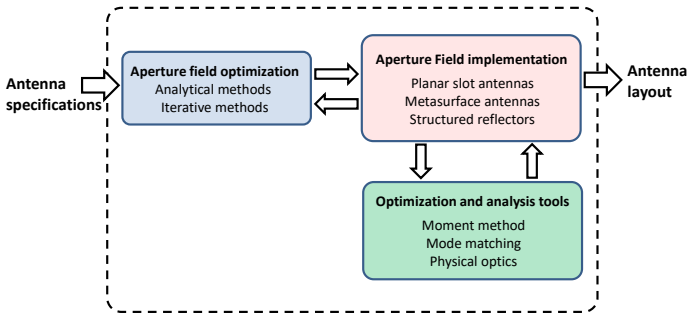

Figure 4.0. Planar antenna implementation algorithm

Aperture field implementation represents a very challenge task. Particular continuous and discrete distributions have been implemented in different ways in the past. In general a single or multiple active elements (dipoles, slots, etc.) are placed closely in the aperture plane sometime in presence of some passive elements. Classic array theory cannot be used in general because of the strong coupling between elements, thus numerical optimization represents the only safe procedure for this purpose. Numerical analysis in conjunction with classical optimization algorithms (genetic algorithm, particle swarm optimization, etc.) can be very time consuming and the optimization become easily impossible as the size of the aperture increase. Moreover, using commercial software, it can be very difficult (in general not all the data are accessible to the user) to define a desired cost function to be minimized.
The idea is to couple analytical and numerical ad-hoc methods in order to take advantage of both methodologies. This scheme can overcome the above mentioned limitations allowing to implement complicated aperture distributions and leading to novel antenna solutions.
The approach is summarized in Fig. 4.0. The long term goal (more then 5 years) is to develop a tool that, given as input certain number of antenna parameters, provides as output the corresponding optimized planar antenna layout. Even if the ideal future goal will be to develop a *blackbox*, more realistically the project aims to develop an "*opaquebox*" for average experienced user (the target are PhD students). To be more specific, the term "*opaque*" has to be interpreted in the sense that the user will need to know only the basics of the involved

methods (and set a minimum number of parameters) and not the details. This user friendly interface will facilitate the collaboration with researcher from other institutions.

The proposed technique is composed of two main steps. The process starts with an aperture field optimization that can be perform using analytical or iterative methods. It is crucial that this step is closely related to the implementation technology. In fact each technology limits in some way the degrees of freedom of the feasible aperture field. As an example, planar slot antennas radiating the energy through a discrete number of slots can only implement discrete aperture distributions.
In the second step the aperture field is synthetized using a preselect technology (slot antennas, metasurface and reflectors). In this task, simplified analytical models based on physical aspects are deeply coupled with ad-hoc numerical full-wave tools. Finally the antenna layout is generated.

In the next sections, the technical details of each block are presented. These activities are on-going and will continue in the next five years and more. On one hand, some important aspects are already well defined and presented in details. Even for these cases, the research will be very active in the next years. On the other hand, new approaches that have to be investigated are reported in the sections *"future works"*.

4.1.1 Aperture Field Optimization

***List of related publications*: [P.4], [P.8]-[P.11], [P.14]-[P.16], [BC.1].**

The goal of any aperture synthesis procedure is to derive an aperture field distribution able to generate a required pattern in the far/near-field region of the aperture. A priori, such ideal pattern may also not be a physical solution of the problem at hand. In this case, the procedure has to find the "best" physical approximation of the pattern.
Several optimization techniques based on near-field near/far-field transformations have been presented in the literature. In this research, the choice to derive the distribution analytically or with semi-analytical methods has been chosen. This aspect allows us to easily introduce physical constraints and to control the convergence of the method.
The semi-analytical methods are based on a set theoretic approach and alternate projection method [4.1]. Each requirement or relevant information is expressed as a set of constraints for the possible solution. The solution of the problem will belong to the intersection of all these sets of constraints or will be the closest one, according to a provided measure criterion.

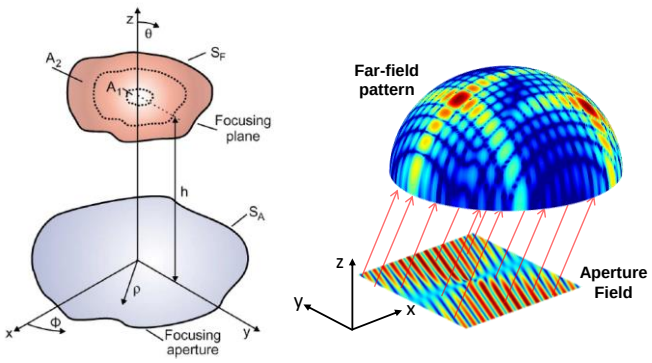

Figure 4.1. Geometry of the problem: (a) near-field synthesis; (b) far-field synthesis.

The geometry of the problem is shown in Fig.4.1. An aperture of size is located at $z=0$ and is radiating in free space. The radiation requirements define an "*objective mask"* for the near field in the focusing plane or for the radiation pattern for the far field. This mask also defines, by an inverse Fourier Transform (FT), a starting distribution for the optimization process. The physical and mechanical constraints (size of the focusing aperture, etc…) define an "*aperture mask"* for the antenna aperture plane. Once the constraints of the problem are defined, an iterative procedure based on an alternative projection method is used to derive the aperture field distribution [4.1].
The process steps can be summed as follows:

1) The physical constraints are imposed on the actual aperture field distribution by applying the aperture mask.

2) The radiation generated by the new aperture field in the far-field or in the focusing plane is computed by the FT of the electric field.
3) The radiation requirements are imposed on the radiated field by applying the objective mask.
4) The field is back propagated to the aperture leading to a new aperture field distribution.
5) While the objective goals are not met, repeat the process (return to step 1).

The procedure is repeated until lays within the imposed requirements in the focusing plane or the squared error is lower than a certain threshold. It is worth saying that the FTs in (2) and (4) have been evaluated with a Fast Fourier Transform (FFT) algorithm speeding up their computation and the overall convergence time of the design procedure.
Since this procedure it is quite known for far-field optimization only the details for the near-field case are presented in the next two subsections. Some preliminary studies on analytical distributions are presented in subsection c.
This research is in collaboration with Dr. Mauro Ettorre (IETR) and Pr. Matteo Albani (University of Siena).

A) Near Field vector optimization on a 2D plane

The required pattern is defined over a focusing plane located at a distance *h* and parallel to the radiating aperture (see Fig. 4.1a). Transverse magnetic (TM) modes with respect to the *z*-direction are considered. However, the procedure can be extended to transverse electric (TE) modes or any combination of modes. In a first stage we focus our attention on the possibility to control the beamwidth and sidelobe level of the z-component of electric field in the focusing plane. In addition invariance is assumed for the radiated field.
The objective mask for the near field in the focusing plane can be defined as follows:

$$Mask = \begin{cases} \dfrac{|E_z(x,y,h)|}{\max\left(|E_z(x,y,h)|\right)} > c_1 & \text{in } A_1 \\ \dfrac{|E_z(x,y,h)|}{\max\left(|E_z(x,y,h)|\right)} > c_2 & \text{in } A_2 \end{cases} \tag{4.1}$$

where $0 < c_2 < c_1 < 1$ are fixed limits for the normalized module of E_z in some space domains A_1 and A_2 over the focusing plane, respectively(see Fig.4.1a). Note that the mask also defines a reference solution equal to c_1 and c_2 in the two domains A_1 and A_2, respectively.
The size of the focusing aperture define the aperture mask (the field is defined only over the surface and it is assumed zero outside this region).
At each iteration the squared error of the field distribution is derived over the focusing plane. Once the error is below a certain threshold the procedure stops.
The output of the optimization is the z–component of the electric field over the focusing aperture. Thanks to the invariance of the radiated field, the tangential electric field can be easily derived.

B) Near Field vector optimization on a 3D volume

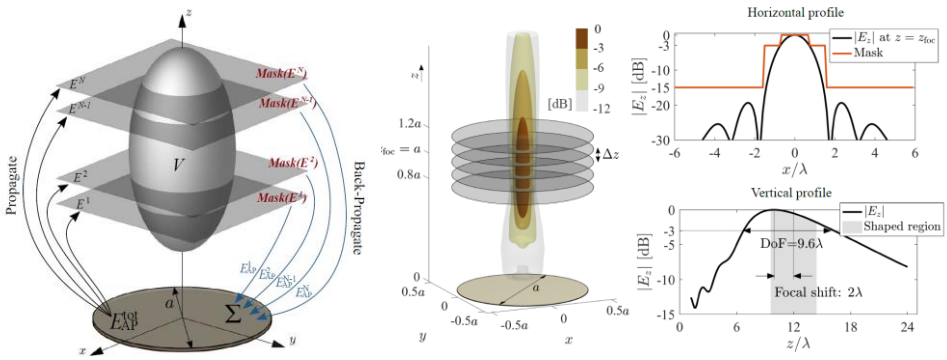

(a) (b)

Figure 4.2. (a) The problem set-up with an illustration of the applied algorithm. (b) 3D focal spot shaping: the grey disks represent the shaping planes. The horizontal profile corresponds to the middle of the shaping volume.

3-D near field shaping consists in defining the source distribution that yields the requested field shape in a predefined volume V (Fig. 4.2a). Ultimately, the goal is to shape the norm of the field, which comprises the three field components in the form of $I = \sqrt{|E_x|^2 + |E_y|^2 + |E_z|^2}$ [4.2].

Given an aperture Σ located at *z=0* (Fig. 4.2a), the objective is to shape the field in the volume *V*, given specific requirements, either on the norm or some field components. The volume is segmented in *N* horizontal parallel planes, equally spaced along z-direction. The requirements are given by specific field masks, which may differ from plane to plane.

Without loss of generality, we assume that the setup supports only a TM mode. In such a problem, the field can be expressed only in terms of the z-component magnetic vector potential *A* [4.3].

The process is visualized in Fig. 4.2 in a clockwise fashion. The whole process can be summed as follows:

1. Calculate the field $E^n(x, y, z_n)$ for *n = 1,...,N*, generated by the aperture field E_{AP}^{tot}.
2. Mask the field at each plane [Mask(E^n)].
3. Back-propagate each masked field to the aperture (E_{AP}^n).
4. Average all the back-propagated fields to create the new aperture distribution: $E_{AP}^{tot} = \sum_n w_n E_{AP}^n$
5. While the shaping goals are not met, repeat the process (return to step 1).

The algorithm stops if the field at step 5 lays inside the mask requirements within a certain defined error.

The key role of the procedure is played by the masking operation of step 2. The mask at each plane of the sampled volume can be the same or different, depending on the pattern requirements (SLL and the beamwidth). It is evident that, in order to achieve convergence of the method, limitations exist concerning the applied constraints (i.e., too small beamwidths) and also, the masks of adjacent planes cannot differ considerably. That said, both the tangential and the vertical to the aperture components can be shaped.

C) Analytical aperture field distributions

Analytical aperture distributions can be derived by physical consideration or by mathematical properties of Fourier transform. Some examples of aperture distribution that have been recently derived are presented below.

A single beam antenna with linear polarization pointing at (θ_0, ϕ_0) can be obtained by imposing the following objective aperture field [P.4**]**:

$$\mathbf{E}_t^{obj}(\boldsymbol{\rho}') = e^{-jk_0(\sin\theta_0\cos\phi_0 x' + \sin\theta_0\sin\phi_0 y')}\hat{\mathbf{e}}(\phi_0) \tag{4.2}$$

where the amplitude is constant over the aperture and the polarization of beam is controlled by $\hat{\mathbf{e}}(\phi_0)$ as :

$$\hat{\mathbf{e}}(\phi_0) = \begin{cases} \cos\phi_0\hat{\mathbf{x}} + \sin\phi_0\hat{\mathbf{y}} & \text{for } \hat{\boldsymbol{\theta}} \text{ polarization} \\ -\sin\phi_0\hat{\mathbf{x}} + \cos\phi_0\hat{\mathbf{y}} & \text{for } \hat{\boldsymbol{\phi}} \text{ polarization} \end{cases} \tag{4.3}$$

Analogously, a CP beam can be obtained by superposing two distributions of the form (4.2) radiating orthogonal LP beams with a $\pi/2$ phase shift. Thus, a broadside Right Hand CP (RHCP) antenna can be generated by distribution (4.2) with a normalized polarization vector given by

$$\hat{\mathbf{e}}(\phi_0) = \left(1/\sqrt{2}\right)\left(\hat{\mathbf{x}} + j\hat{\mathbf{y}}\right). \tag{4.4}$$

An aperture field distribution that radiates multiple beams can be obtained by superposing the field distributions of the form (4.2),(4.3) leading to [P.4**]**:

$$\mathbf{E}_t^{obj}(\boldsymbol{\rho}') = \frac{1}{N_{beams}} \sum_{k=1}^{N_{beams}} \mathbf{E}_t^k(\boldsymbol{\rho}') \tag{4.5}$$

where N_{beams} is the number of beams and $\mathbf{E}_t^k(\boldsymbol{\rho}')$ is the objective field corresponding to each individual beam. The whole aperture is thus used to generate the radiation of the whole beams.

For flat-top antenna applications require an almost constant normalized radiation pattern F_n within an angular region, (while it is below a certain threshold outside of the region), namely

$$\left\|F_n(\theta)\right\| = \begin{cases} 1 \pm \delta & \text{if } |\theta| < \theta_f \\ < \tau & \text{if } |\theta| > \theta_f \end{cases} \tag{4.6}$$

where δ is the maximum oscillation with respect to the desired level and $\tau < 1$ is the threshold.

An aperture distribution able to radiate a field of the form (4.6) with RHCP can be obtained by multiplying the bi-dimensional inverse Fourier transformation of the characteristic function of a circular disk [4.4] by the term $(\hat{\mathbf{x}} + i\hat{\mathbf{y}})$ as:

$$\mathbf{E}_t^{obj}(\boldsymbol{\rho}') = \frac{1}{\sqrt{2}}(\hat{\mathbf{x}} + i\hat{\mathbf{y}}) \frac{J_1(k_0 \rho' \sin\theta_f)}{k_0 \rho' \sin\theta_f} \tag{4.7}$$

As seen in (4.7), θ_f is fixed a priori, while quantities δ and τ in (4.6) depend on aperture dimension.

As a final example of aperture field for near field focalization is presented based on high-frequency techniques applied to cylindrical wave function. The idea is to express the field radiated by inward cylindrical waves traveling over a radiating infinite aperture in terms of incomplete Hankel functions. The radiated field is split into two main contributions: Geometrical Optics (GO) and Space Wave (SW) arising at the aperture center. Closed form expressions clearly show that the GO contribution creates a non-diffractive Bessel beam radiation close to the axis of symmetry of the generating aperture, where the SW is negligible. Therefore, non-diffractive radiation is not only generated by resonant apertures having a Bessel-like distribution given by a combination of inward and outward cylindrical waves, thus simplifying the beam generator synthesis (Fig.4.3).

In contrast, outward cylindrical wave infinite aperture distributions cannot provide a non-diffractive beam generation. The finite aperture case has been considered for an inward aperture illumination, showing that the non-diffractive Bessel beam is still generated within a given a non-diffractive range, as it happens for finite size Bessel distributions (Figure 4.4) [P.15] [BC1].

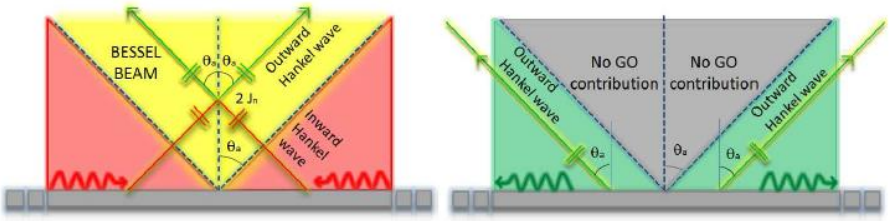

Figure 4.3- Ray interpretation of the GO field for an infinite aperture. (a) Inward Hankel aperture distribution: the GO field comprises an inward Hankel beam ray (in red), present throughout the space, and an outward Hankel beam ray (in green) bounded inside the cone $\theta < \theta_a$; the superposition of the two rays inside the cone (yellow area) creates a Bessel beam. (b) Outward Hankel aperture distribution: the GO field comprises only an outward Hankel beam ray (in green) bounded outside the cone $\theta < \theta_a$.

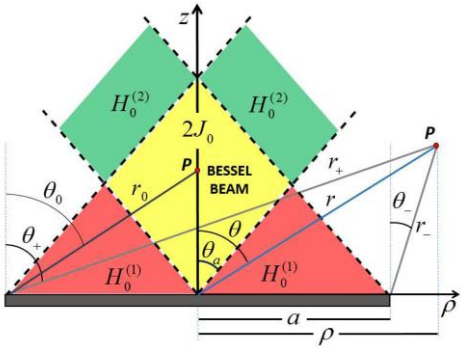

Figure 4.4 - Aperture geometry and map of the GO contribution to the z-component of the electric field radiated by a finite inward cylindrical traveling wave aperture distribution. The Bessel beam is generated in the yellow region around the longitudinal z-axis.

Future works

In the next future, the TE component of the field will be introduced in the optimization processes (A) and (B) in order to allow a full vector optimization.

The impact on antenna parameters (side lobe level, etc..) of the interaction between multiple beams in aperture expression (4.5) will be analysed and alternative expression will be investigated.

A *quality test* of our solution will be done by comparing the obtained optimal distribution with those provided by pure numerical algorithm. For this purpose we plan to open a collaboration with Dr. Giacomo Olivieri (University of Trento) an expert in convex optimization.

4.1.2 Synthesis of the aperture field distribution

This section presents the details of the aperture field synthesis approach and the analysis methods for the three different technologies: planar slot antenna, metasurface antenna, and structured reflectors.

4.1.2.1 Planar slots antennas

***List of related publications*: [P.7], [P.16]-[P.18], [P.20]-[P.21], [IC.2]- [IC.6], [C.1], [C.1], [C.13].**

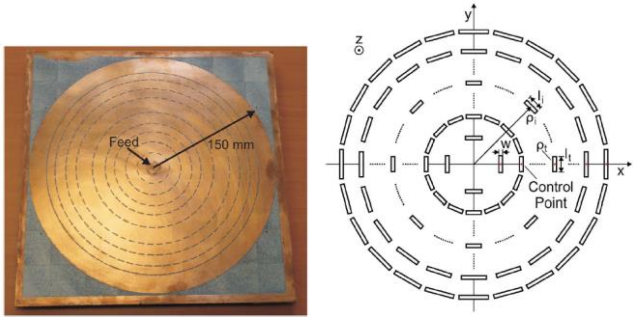

(a) (b)

Figure 4.5 (a) Example of Radial Slot Line Antenna. (b) Optimization of the slots position.

The basic idea of Radial line slot array (RLSA) [4.5],[4.6] is to launch a radial wave (outward or inward) in a parallel-plate waveguide. This wave then radiates out of a series of slots cut into the top face of the antenna. In principle, by an appropriate choice of the slots position and orientation it is possible to control the radiated field. RLSA are attractive antenna solutions thanks to their compactness, planarity and high efficiency. An example of RLSA is shown in Figure 4.5a, where an outward wave is excited by a coaxial feed placed in the middle of the antenna.

The aperture field distribution derived using one of the method presented before corresponds to an equivalent aperture magnetic current distribution. The current distribution is synthesized by using the slots of the RLSA. Each slot is equivalent to a magnetic dipole oriented along the slot length. The dipole moment is proportional to the feeding mode (outwards cylindrical wave) within the parallel plate waveguide (PPW) of the RLSA antenna and function of the position and size of the corresponding slot. The slots, and as a consequence their equivalent magnetic dipoles, must be oriented in the same direction as the current distribution for its synthesis [4.7]. It is worth saying that the mutual coupling between each slot of any ring and the surrounding slots may be different and may induce small asymmetries in the radiated field. For each slot of the RLSA the equivalent magnetic dipole moment is derived with an in-house full-wave analysis tool presented in the next subsection. The position and length of any slot is adjusted for synthesizing the derived aperture magnetic current distribution. For each slot or control point (see Fig. 4.5b) a complex fitness function is defined as follows:

$$F_t = \frac{M_r(\boldsymbol{\rho}_t)}{M_o(\boldsymbol{\rho}_t)} \tag{4.8}$$

where M_r and M_o are the realized and target magnetic dipole moment amplitude. The phase and amplitude of the fitness function represent the error between the target and actual magnetic dipole moment distribution over the aperture. The fitness function is used to modify the position and length of the slots within an optimization loop. At each iteration of the optimization process, the in-house analysis tool is used to evaluate the slots'

magnetic dipole moment distribution. The fitting function is then derived. In addition, the spillover efficiency of the antenna is also calculated. The spillover efficiency is maximized during the optimization. The position and length of the slots are updated accordingly to physical consideration as for example the phase of the guided wave. An example of RLSA optimization is reported in Fig.4.6

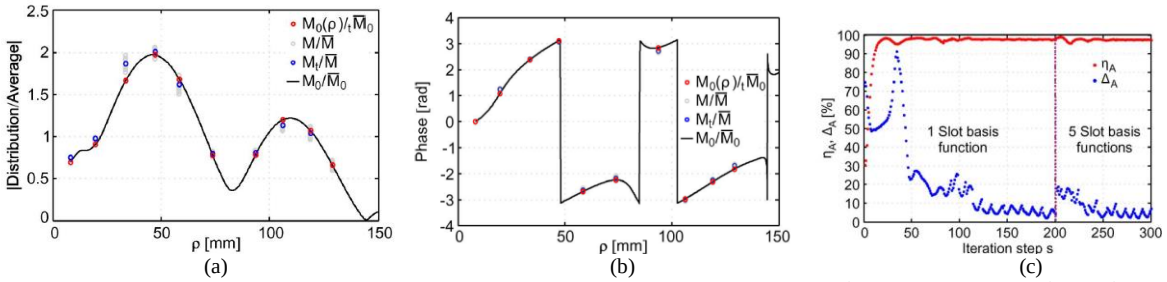

(a) (b) (c)

Fig. 4.6. Ideal and synthesized magnetic dipole moment distribution provided by the two steps of the design procedure for the final RLSA antenna: (a) magnitude;(b) phase; (c) spillover efficiency and average aperture distribution error versus iteration step with a different number of entire domain basis functions for the analysis of the RLSA with the MoM code.

Future work

The phase associated to a slot is mainly dictated by the phase of the wave propagating inside the waveguide. This limits the positions where a slot with a particular moment dipole phase could be etched. This effect can lead to aliasing in the aperture sampling.

To avoid this problem two approaches will be tested: 1) the use of non-radiating slot acting as phase shifter; 2) the use of multiple feeders.

Planar Antenna Full wave analysis

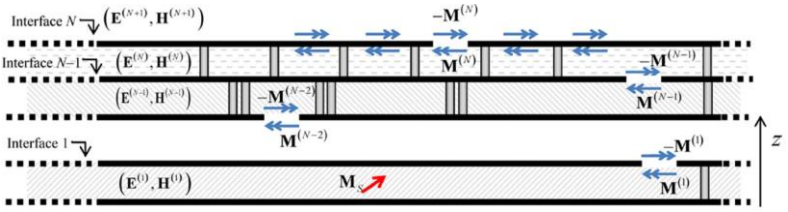

Figure 4.7. Stacked-PPW geometry analyzed in this paper. In each PPW, metallic and/or dielectric posts can be arbitrarily placed. The PPWs are numbered from the lowest (1) to the uppermost . The th PPW is bounded on the top by the th interface and on the bottom by the th interface; it is filled by a material with relative permittivity and permeability and , respectively. In the MoM described here, slots etched in the interfaces (in white) are replaced by equivalent magnetic currents (horizontal arrows). The structure is excited by the magnetic current (diagonal arrow), considered as a "feeding port" in the paper.

Over the past decade, SIW technology has been steadily becoming a technology of choice in the millimeter-wave region, primarily due to ease of fabrication using standard procedures, and the possibility of integration with other well-known radiating and guiding planar structures. Numerous structures, e.g., [4.8]–[4.11], have been designed over the years using approximate analytical methods based on the equivalent-waveguide-width model [4.12] and transmission-line theory [4.13] or finite-difference (FD) and finite-element-method (FEM)-based full-wave solvers. In the former case, the computational efficiency is achieved at the expense of accuracy, which is, in general, low for a broad range of structural parameters. In the latter case, the demand on computational resources of FD and FEM solvers may become extreme or render such solvers inapplicable even on high-end configurations. Therefore, a general, fast, and accurate analysis tool is needed for designing and optimizing generic SIW structures, ranging from, for example, relatively simple filters to complex radiating slot arrays, e.g., [4.9], [4.10], [4.14]. Existing numerical methods either are applicable to large structures but do not take into account specific features of the structures, or overly simplify the problems by assuming restrictive symmetries or simplified field variations (e.g., periodicity or absence of vertical or azimuthal variation of the post currents) [4.15], [4.16].

The main idea of this activity is to develop a rigorous full-wave code taking advantage of specific SIW features to accurately analyze complex and electrically large radiating structures through a realistic detail of all the relevant components. Specifically, as proved in my previous research activity [4.17], azimuthal variations around the posts are required to model posts with moderate diameter, while vertical parallel-plate waveguide (PPW)

modes are required to model the breaking of vertical uniformity due as for example to slot coupling or coaxial excitation.
The approach utilizes the advantages of method of moments (MoM) and mode matching (MM), as well as of the convenient representation of electromagnetic fields.

The formulation has to:
1) models losses in the dielectric substrate and in the metallic wall of the waveguides;
2) models metallic and dielectric lossy posts;
3) includes an arbitrary number of aperture-coupled stacked PPWs;
4) reduces the computation effort due to MM problems for radially attenuated modes by restricting the analyses to a limited number of posts selected through a simple rule-of-thumb;
5) speed up the computation of MoM matrix entries and forcing terms (asymptotic evaluations of the coupling integrals);

In order to achieve the above mentioned goals, we split the Green's function into a PPW contribution and a post-scattered one. The former contribution is expressed in terms of a radial transmission-line representation, converging much faster than the alternative z-transmission-line representation for larger radial dimensions. The latter contribution is expressed as a series of cylindrical vector wave functions. This leads to an efficient representation and to an easy control of the degree of accuracy. Radiating or coupling slots are accounted for by introducing equivalent magnetic currents. Boundary conditions on slots are enforced, and a method of moments is formulated and solved. Acceleration strategies based on common symmetries of slot arrays can be introduced. These are possible since we can isolate the physical contributions of different wave species (PPW modes, free-space interactions, post-scattering, guided waves) in the complete expressions of the MoM matrix entries and would not hold for an MoM fully discretizing all the vertical posts.
This work is done in collaboration with Dr. Guido Valerio (L2E).

Losses in the dielectric substrate and in the metallic wall of the waveguides

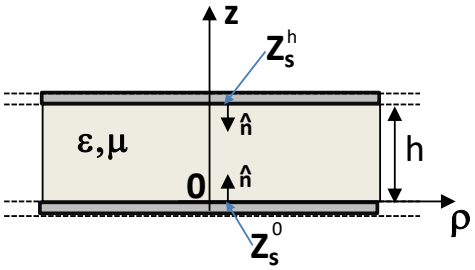

Figure 4.8. Lateral view of a lossy PPW

In typical microwave applications, SIW channels are obtained by drilling commercial metalized dielectric substrates, and then filling the holes with conducting materials (or dielectric) in order to implement the cylindrical posts. This procedure leads to structures that use the same kind of metallization for both top and bottom planes. Moreover, at microwave regime, the roughness of the metallization can be in general neglected. All these considerations lead to the use of the Leontovich equivalent boundary condition for the metallic planes

$$Z_s = (1+j)\sqrt{\omega\mu_s / (2\sigma)} \tag{4.9}$$

where σ is the conductivity, ω is the angular velocity and μ_s is the permeability.
Other type of surfaces (such as thin metals [4.18], rough surfaces [4.19],[4.20] or partially reflecting surfaces [4.21]) can be modeled through an equivalent impedance. At a first stage only lossy metal plates will be considered henceforth.
The structure under analysis consists of a PPW, defined by two horizontal lossy metallic plates placed at a distance h, laterally unbounded, filled by a dielectric medium (see Fig. 4.8). Inside the PPW an arbitrary number of vertical cylindrical posts can be placed, either of penetrable or impenetrable medium.
From a computational point of view, it is of paramount importance to choose the most effective representation according to the kind of field. In this view, the cylindrical eigenmode expansion of the field seems to be the appropriate choice [4.22]. The fields scattered by these posts can be modeled by linear sums of vector modes with unknown amplitude, while the incident field on the posts can be computed through a Green's function represented in terms of eigenfunctions expansion [4.22]. The scattered amplitudes are then found by imposing boundary conditions on the post surfaces.

Vector functions are defined as in [4.22, Sec. 7.2]

$$\begin{aligned}\mathbf{M}(\mathbf{r}) &= \nabla\times\left[\hat{\mathbf{z}}\Phi^{TM}(\mathbf{r})\right],\\ \mathbf{N}(\mathbf{r}) &= \frac{1}{k}\nabla\times\nabla\times\left[\hat{\mathbf{z}}\Phi^{TE}(\mathbf{r})\right],\end{aligned} \tag{4.10}$$

referring to the transverse (with respect to z) magnetic field TM^z and TE^z polarization, respectively. The scalar Φ functions must satisfy the scalar Helmholtz equation. Assuming a $e^{j\omega t}$ time harmonic dependence, it can be solved by conventional means, through separation of variables in cylindrical coordinates $\mathbf{r}\equiv(\rho,\phi,z)$ (in anticipation of the presence of circular cylindrical scatterers), yielding

$$\Phi^t_{mn}(\mathbf{r}) = c_m\begin{bmatrix} J_n\left(k^t_{\rho_m}\rho\right)\\ H^{(2)}_n\left(k^t_{\rho_m}\rho\right)\end{bmatrix}e^{-jn\phi}\psi^t_m(z), \tag{4.11}$$

with $t=$ TM/TE, where J_n and $H^{(2)}_n$ are n-th order Bessel and second kind Hankel functions describing the radial dependence of fields inside and outside the posts, respectively. $k^t_{\rho_m}$, $k^t_{z_m}$ are the m-th TM/TE mode transverse propagation constants and the z functions are eigenvalues of the Sturm-Liouville problem

$$\left[\frac{d^2}{dz^2}+\left(k^t_z\right)^2\right]\psi^t(z)=0 \tag{4.12}$$

subject to the following boundary conditions on the conductor plates

$$\begin{aligned}&\left[j\omega\varepsilon Z_s-(\hat{\mathbf{n}}\cdot\hat{\mathbf{z}})\frac{d}{dz}\right]\psi^{TM}(z)\Big|_{z=0,h}=0,\\ &\left[1-(\hat{\mathbf{n}}\cdot\hat{\mathbf{z}})\frac{Z_s}{j\omega\mu}\frac{d}{dz}\right]\psi^{TE}(z)\Big|_{z=0,h}=0.\end{aligned} \tag{4.13}$$

Since the coefficients of the terms in the boundary conditions are complex, this defines a nonself-adjoint Sturm-Liouville problem [4.22, Sec. 5.3]. If we wish to construct complete orthonormal sets based on these solutions in order to construct arbitrary fields, we need normalized eigenfunctions. This can be accomplished through a suitable choice of the coefficients c_m. Using the L^2-Hermitian inner product the eigenfunctions $\bar{\psi}$ of the adjoint problem are obtained from a Helmholtz operator having a complex conjugate wavenumber and adjoint boundary conditions at the conducting plates.
Since the solutions $\bar{\psi}$ to the adjoint TM/TE problems are the complex conjugate of ψ, the normalization can be performed through the bi-orthogonality relationship as [4.22, Sec. 5.3]

$$\left\langle\psi^t_m,\bar{\psi}^t_n\right\rangle=\int_0^h\psi^t_m(z)\bar{\psi}^{t*}_n(z)\,dz=\delta_{mn}, \tag{4.14}$$

with $t=$ TM/TE and δ_{mn} denoting the Kronecker's symbol $\delta_{mn}=1$ when $m=n$ or $\delta_{mn}=0$ when $m\neq n$.
This procedure leads to

$$\begin{aligned}\psi^{TM}_m &= \bar{\psi}^{TM*}_m=\sqrt{\frac{2}{h}}\frac{Z^{TM}_m\cos\left(k^{TM}_{z_m}z\right)+jZ_s\sin\left(k^{TM}_{z_m}z\right)}{\sqrt{\left(Z^{TM}_m\right)^2-Z_s^2+2jZ^{TM}_mZ_s\Big/\left(k^{TM}_{z_m}h\right)}},\\ \psi^{TE}_m &= \bar{\psi}^{TE*}_m=\sqrt{\frac{2}{h}}\frac{Z^{TE}_m\sin\left(k^{TE}_{z_m}z\right)-jZ_s\cos\left(k^{TE}_{z_m}z\right)}{\sqrt{\left(Z^{TE}_m\right)^2-Z_s^2-2jZ^{TE}_mZ_s\Big/\left(k^{TE}_{z_m}h\right)}}.\end{aligned} \tag{4.15}$$

where $Z_m^{TM} = \dfrac{k_{z_m}^{TM}}{\omega\varepsilon}, Z_m^{TE} = \dfrac{\omega\mu}{k_{z_m}^{TE}}$ are the modal impedance of the *m*-th TM/TE mode, respectively and $k_{z_m}^{TM}, k_{z_m}^{TE}$ are the *m*-th solution (eigenvalues) of the following dispersion equations

$$\begin{aligned} j\left(Z_s^2 + Z_m^{TM^2}\right)\tan\left(k_{z_m}^{TM} z\right) + 2Z_m^{TM} Z_s = 0 \\ j\left(Z_s^2 + Z_m^{TE^2}\right)\tan\left(k_{z_m}^{TE} z\right) + 2Z_m^{TE} Z_s = 0 \end{aligned} \tag{4.15}$$

Having obtained orthonormal bases for the eigenfunction expansion, we proceed to derive the dyadic magnetic Green's function, given in [4.24],[4.25] as

$$\begin{aligned} \underline{\mathbf{G}}^{PPW,HM}\left(\mathbf{r},\mathbf{r}'\right) = -\frac{1}{k^2}\left[\hat{\mathbf{z}}\hat{\mathbf{z}} + \frac{\nabla_t \nabla_t}{\nabla_t^2}\right]\delta\left(\mathbf{r}-\mathbf{r}'\right) + \frac{1}{4j}\left[\sum_{m=0}^{+\infty}\sum_{n=-\infty}^{\infty}\frac{(-1)^n}{k_{\rho_m}^{TM^2}}\mathbf{M}_{m,-n}\left(k_{\rho_m}^{TM}, k_{z_m}^{TM}, \boldsymbol{\rho}', z'\right)\mathbf{M}_{mn}\left(k_{\rho_m}^{TM}, k_{z_m}^{TM}, \boldsymbol{\rho}, z\right)\right. \\ \left. + \sum_{m=1}^{+\infty}\sum_{n=-\infty}^{\infty}\frac{(-1)^n}{k_{\rho_m}^{TE^2}}\mathbf{N}_{m,-n}\left(k_{\rho_m}^{TE}, k_{z_m}^{TE}, \boldsymbol{\rho}', z'\right)\mathbf{N}_{mn}\left(k_{\rho_m}^{TE}, k_{z_m}^{TE}, \boldsymbol{\rho}, z\right)\right] \end{aligned} \tag{4.16}$$

Thus, the incident magnetic field radiated by a magnetic source $\mathbf{J}_M$ distributed on a surface S' is obtained as the convolution of (4.16) with $\mathbf{J}_M$, resulting in

$$\mathbf{H}^{PPW}\left(\mathbf{r},\mathbf{r}'\right) = \sum_{m=0}^{+\infty}\sum_{n=-\infty}^{\infty} v_{m,-n}^{TM}\mathbf{M}_{mn}\left(k_{\rho_m}^{TM}, k_{z_m}^{TM}, \boldsymbol{\rho}', z'\right) + \sum_{m=1}^{+\infty}\sum_{n=-\infty}^{\infty} v_{m,-n}^{TE}\mathbf{N}_{mn}\left(k_{\rho_m}^{TE}, k_{z_m}^{TE}, \boldsymbol{\rho}', z'\right) \tag{4.17}$$

where $v_{mn}^t = -\dfrac{\omega\varepsilon_0\varepsilon_r(-1)^n}{4\left(k_{\rho_m}^t\right)^2}\int_{S'}\mathbf{P}_{mn}^t\left(k_{\rho_m}^t, k_{z_m}^t, \boldsymbol{\rho}'-\boldsymbol{\rho}_q, z'\right)\cdot\mathbf{J}_M\left(\mathbf{r}'\right)d^2r'$, with $\mathbf{P}_{mn}^{TM} = \mathbf{M}_{mn}$, $\mathbf{P}_{mn}^{TE} = \mathbf{N}_{mn}$.

Metallic and dielectric lossy posts

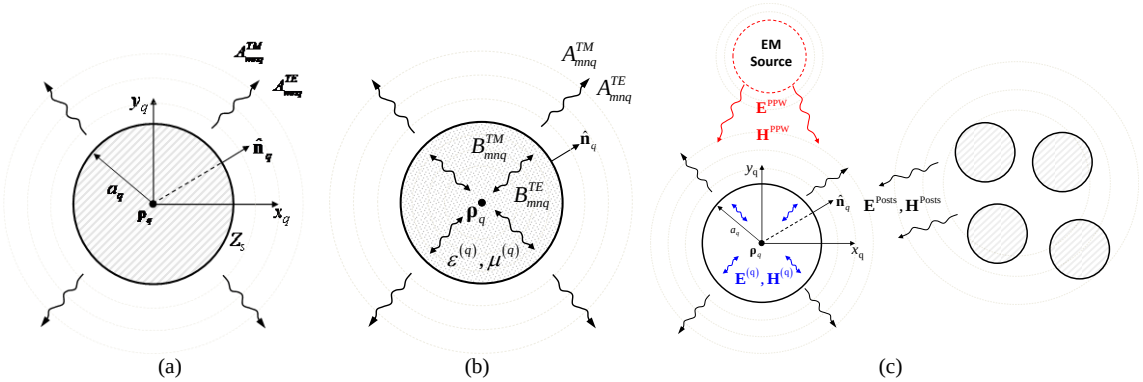

(a) (b) (c)

Figure 4.9. Vector eigenfunction expansion of the scattered field from: (a) impenetrable post; (b) penetrable post; (c) incident scattered and transmitted field in a penetrable post.

Once the dyadic Green's function and vector wave functions are known, one can proceed to the formulation of the MM/MoM problem, since all types of fields (impressed and scattered) on the post surfaces can be described efficiently. A resolvable system of linear equations is obtained by imposing the appropriate boundary conditions. The field scattered by the posts in the whole SIW structure is thus expressed as a discrete sum of vector cylindrical waves defined as

$$\mathbf{H}_s\left(\mathbf{r}\right) = \sum_{l=1}^{N_{post}}\sum_{m=1}^{+\infty}\sum_{n=-\infty}^{+\infty} A_{mnl}^{TM}\mathbf{M}_n\left(k_{\rho_m}^{TM}, k_{z_m}^{TM}, \boldsymbol{\rho}-\boldsymbol{\rho}_l, z\right) + A_{mnl}^{TE}\mathbf{N}_n\left(k_{\rho_m}^{TE}, k_{z_m}^{TM}, \boldsymbol{\rho}-\boldsymbol{\rho}_l, z\right) \tag{4.18}$$

To determine the field scattered by an impenetrable post (Fig. 4.9a) of radius a_q, described by a non-dispersive impedance condition Z_s, we impose the following boundary condition on the surface of the post

$$\hat{\boldsymbol{\rho}}_q \times \mathbf{E}^{\mathrm{TOT}}(\mathbf{r})\big|_{|\boldsymbol{\rho}-\boldsymbol{\rho}'|=a_q} = Z_s \hat{\boldsymbol{\rho}}_q \times \hat{\boldsymbol{\rho}}_q \times \mathbf{H}^{\mathrm{TOT}}(\mathbf{r})\big|_{|\boldsymbol{\rho}-\boldsymbol{\rho}'|=a_q} \tag{4.19}$$

where $\hat{\boldsymbol{\rho}}_q$ is the radial unit vector directed from the center of the post toward the exterior of the post, and $\mathbf{E}^{\mathrm{TOT}}$ and $\mathbf{H}^{\mathrm{TOT}}$ are the total electric and magnetic fields, respectively. For $Z_s = 0$ condition (4.19) resort to the PEC post case.

The fields are expanded through cylindrical wave functions as in (4.18). From the two scalar components of the vector identity (4.19) a couple of linear equations is obtained for the unknowns A^t_{mnq}. They are expressed as a series of azimuthal modes with linear phase around the *q*-th cylinder. From the orthogonality of the azimuthal eigenfunctions $e^{jn\phi}$ we can obtain two linear equations for each azimuthal harmonic $\bar{n}$

$$f_\phi^{\bar{n}}\left(A^{TM}_{mnq}, A^{TE}_{mnq}\right) = t_\phi^{\bar{n}}, \quad f_z^{\bar{n}}\left(A^{TM}_{mnq}, A^{TE}_{mnq}\right) = t_z^{\bar{n}} \tag{4.20}$$

The two equations come from the ϕ and the *z* components of (4.19); $f_\phi^{\bar{n}}$ and $f_z^{\bar{n}}$ are linear functions of A^{TM}_{mnq} and A^{TE}_{mnq}, $t_\phi^{\bar{n}}$ and $t_z^{\bar{n}}$ are known quantities depending on the excitation current. For each harmonic $\bar{n}$, (4.20) can then be projected on the $\bar{m}$-th adjoint vertical eigenfunction $\bar{\psi}^t_{\bar{m}}$ in order to obtain a linear system having the same number of equations and unknowns. The obtained equations contains the scalar products between different polarization eigenfunctions: $\left\langle \psi_m^{TE\prime}, \bar{\psi}_{\bar{m}}^{TM} \right\rangle, \left\langle \psi_m^{TM\prime}, \bar{\psi}_{\bar{m}}^{TE} \right\rangle$.

If $Z_s = 0$, (4.19) and (4.20) both reduce to the simpler case of a PEC post, where the TE and TM polarizations are decoupled.

To determine the field scattered from a penetrable (possibly lossy) post, whose radius is a_q and complex dielectric constants are $\varepsilon_r^{(q)}, \mu_r^{(q)}$, the continuity of the tangential electric and magnetic fields are imposed on the post surface (Fig. 4.9c)

$$\hat{\boldsymbol{\rho}}_q \times \mathbf{E}^{\mathrm{PPW}}(\mathbf{r}) + \hat{\boldsymbol{\rho}}_q \times \mathbf{E}^{\mathrm{Posts}}(\mathbf{r})\big|_{|\boldsymbol{\rho}-\boldsymbol{\rho}'|=a_q} = \hat{\boldsymbol{\rho}}_q \times \mathbf{E}^{(q)}(\mathbf{r})\big|_{|\boldsymbol{\rho}-\boldsymbol{\rho}'|=a_q} \tag{4.21}$$

$$\hat{\boldsymbol{\rho}}_q \times \mathbf{H}^{\mathrm{PPW}}(\mathbf{r}) + \hat{\boldsymbol{\rho}}_q \times \mathbf{H}^{\mathrm{Posts}}(\mathbf{r})\big|_{|\boldsymbol{\rho}-\boldsymbol{\rho}'|=a_q} = \hat{\boldsymbol{\rho}}_q \times \mathbf{H}^{(q)}(\mathbf{r})\big|_{|\boldsymbol{\rho}-\boldsymbol{\rho}'|=a_q} \tag{4.22}$$

where the superscripts 'PPW', 'Posts', and '*q*' stand respectively for the fields excited in the PPW in the absence of the posts, for the fields scattered by all the posts, and for the field inside the *q*-th post under analysis. The fields in the waveguide are expanded through the Hankel function formulation of (4.18), while the field inside each cylinder is expanded through the Bessel function expression. Note that, if the post is metallic, a null field is retained inside the post, and only the electric field continuity (4.21) is used.

Each equation (4.21)-(4.22) can be projected along the ϕ and the *z* directions, thus obtaining a system of four scalar equations for the unknown coefficient $A^{TM/TE}_{mnl}$ and $B^{TM/TE}_{mnl}$. These scalar equations are then projected on the basis of harmonic functions describing the azimuthal dependence of field around the considered cylinder. For each harmonic $\bar{n}$, the two equations resulting from the components of (4.22) are

$$e_\phi^{\bar{n}}\left(A^{TM}_{mnl}, B^{TM}_{mnl}\right) = t_\phi^{\bar{n}} \tag{4.23}$$

$$e_z^{\bar{n}}\left(A^{TM}_{mnl}, A^{TE}_{mnl}, B^{TM}_{mnl}, B^{TE}_{mnl}\right) = t_z^{\bar{n}} \tag{4.24}$$

and the two equations resulting from the components of (4.22) are

$$h_\phi^{\bar{n}}\left(A^{TE}_{mnl}, B^{TE}_{mnl}\right) = s_\phi^{\bar{n}} \tag{4.25}$$

$$h_z^{\bar{n}}\left(A^{TM}_{mnl}, A^{TE}_{mnl}, B^{TM}_{mnl}, B^{TE}_{mnl}\right) = s_z^{\bar{n}} \tag{4.26}$$

where *e* and *h* are linear functions of $A^{TM/TE}_{mnl}$ and $B^{TM/TE}_{mnl}$, and *t* and *s* are known quantities depending on the excitation current. The four equations can then be projected on the vertical eigenfunctions $\bar{\psi}$ in order to obtain a linear system having the same number of equations and unknowns. Specifically, a careful choice of the

eigenfunctions should be done in order to obtain stable solutions even for large losses in the cylinder. In fact, we can have eigenfunctions defined *inside* the *q*-th post (where wavenumbers are referred to the post dielectric), namely $\bar{\psi}_m^{(q)}$, and eigenvalues defined in the PPW (where wavenumbers are referred to the PPW dielectric), namely $\bar{\psi}_m$. It turns out that the best strategy is to project (4.23) and (4.26) on $\bar{\psi}_m$, and (4.24) and (4.25) on $\bar{\psi}_m^{(q)}$

$$\left\langle e_\phi^{\bar{n}}\left(A_{mnl}^{TM}, B_{mnl}^{TM}\right), \bar{\psi}_{\bar{m}_1}^{TM}\right\rangle = \left\langle t_\phi^{\bar{n}}, \bar{\psi}_{\bar{m}_1}^{TM}\right\rangle \tag{4.27}$$

$$\left\langle h_\phi^{\bar{n}}\left(A_{mnl}^{TE}, B_{mnl}^{TE}\right), \bar{\psi}_{\bar{m}_2}^{TE}\right\rangle = \left\langle s_\phi^{\bar{n}}, \bar{\psi}_{\bar{m}_2}^{TE}\right\rangle \tag{4.28}$$

$$\left\langle e_z^{\bar{n}}\left(A_{mnl}^{TM}, A_{mnl}^{TE}, B_{mnl}^{TM}, B_{mnl}^{TE}\right), \bar{\psi}_{\bar{m}_2}^{TE(q)}\right\rangle = \left\langle t_z^{\bar{n}}, \bar{\psi}_{\bar{m}_2}^{TE(q)}\right\rangle \tag{4.29}$$

$$\left\langle h_z^{\bar{n}}\left(A_{mnl}^{TM}, A_{mnl}^{TE}, B_{mnl}^{TM}, B_{mnl}^{TE}\right), \bar{\psi}_{\bar{m}_1}^{TM(q)}\right\rangle = \left\langle s_z^{\bar{n}}, \bar{\psi}_{\bar{m}_1}^{TM(q)}\right\rangle \tag{4.30}$$

We can derive explicit expressions for B_{mnl}^{TM} from (4.27) and for B_{mnl}^{TE} from (4.28), and substitute them into (4.29) and (4.30). Using the bi-orthogonality relationship (4.14) we finally obtain two scalar equations for the unknowns A_{mnl}^{TM} and A_{mnl}^{TE}. It turns out that with the above-mentioned testing choice, these expressions are composed only by terms having ratio of Bessel/Hankel functions of eigenvalue of the same medium. Thus, also with a large imaginary part of the argument the terms remain numerically stables.

Arbitrary number of aperture-coupled stacked PPWs

Let us consider a stacked configuration, where an arbitrary stratification of PPWs is present, and adjacent PPWs are coupled through slots etched in the interfaces (see Fig. 4.7). The generic *n*th PPW is bounded on the top by the *(n+1)*th interface and on the bottom by the *n*th interface. Its electromagnetic parameters are denoted as ε_n and μ_n. Magnetic currents on both the upper and the lower plates of each PPW. They are taken into account in the integral equation with a different sign, due to the opposite directions of the vectors normal to the different interface. In the *k*th PPW, the magnetic field is denoted by the superscript "*(k)*". The equivalent unknown magnetic currents are denoted with the superscript "*(k+1)*", if placed on the *upper* plate of the *k*th PPW. The currents are denoted with the superscript "*(k)*" if placed on the *lower* plate of the *k*th PPW (see Fig. 4.7).
We can write, on the *k*th interface, the following integral equation:

$$\hat{\mathbf{z}}\times\left\{\mathbf{L}^{(k+1)}\left[\mathbf{M}^{(k+1)}\right]-\mathbf{L}^{(k+1)}\left[\mathbf{M}^{(k)}\right]-\mathbf{L}^{(k)}\left[\mathbf{M}^{(k)}\right]+\mathbf{L}^{(k)}\left[\mathbf{M}^{(k-1)}\right]\right\}=\hat{\mathbf{z}}\times\left\{\mathbf{H}_{inc}^{(k)}-\mathbf{H}_{inc}^{(k+1)}\right\} \tag{4.31}$$

The integral operator $\mathbf{L}^{(k)}$ operates on a magnetic current to yield the magnetic field inside the *k*th PPW

$$\mathbf{L}^{(k)}\left[\mathbf{A}\right]=-j\omega\varepsilon_k\int_S \underline{\underline{\mathbf{G}}}^{SIW,k}\left(\mathbf{r},\mathbf{r}'\right)\cdot\mathbf{A}\left(\mathbf{r}'\right)d\mathbf{r}' \tag{4.32}$$

where $\underline{\underline{\mathbf{G}}}^{SIW,k}$ is the Green's function of the *k*th SIW.
The unknown magnetic function $\mathbf{M}$ is discretized as a sum of suitable entire-domain basis functions

$$\mathbf{M}\left(\mathbf{r}\right)=\sum_{f=1}^{N_b N_{slot}} v_f\mathbf{b}_f\left(\mathbf{r}\right) \tag{4.33}$$

where N_{slot} is the total number of slots present, and N_b is the number of basis functions present on each slot.
As far as narrow rectangular slots are of interest, the current can be assumed directed along the length of each slot, and its transverse dependence is neglected. This assumption has validated for slots having a width $w<\lambda/10$, λ being the medium wavelength. In this case, if a local Cartesian reference system (u,v) is associated to the *q*th slot (where the *u*-axis is along its length L_q, and the -axis along its width W_q, with the origin at its center), the sinusoidal basis functions $\mathbf{b}_{q,n}$ are

$$\mathbf{b}_{q,n}\left(\mathbf{r}\right)=\hat{\mathbf{u}}\frac{1}{W_q}\sin\left[\frac{n\pi}{L_q}\left(u+\frac{L_q}{2}\right)\right] \tag{4.34}$$

for $-\frac{L_q}{2} \le u \le \frac{L_q}{2}$ and $-\frac{W_q}{2} \le v \le \frac{W_q}{2}$ .This particular choice of entire-domain basis functions has several advantages. It reduces the filling time of the MoM impedance matrix, leads to a significant memory saving, and avoids possible problems related to the numerical solutions of large linear systems [4.26].
Using a Galerkin testing procedure a linear system is obtained, where the admittance matrix has a block structure as

$$\begin{bmatrix} \left(\underline{\mathbf{Y}}_{1,1}^{(0)}+\underline{\mathbf{Y}}_{1,1}^{(1)}\right) & -\underline{\mathbf{Y}}_{1,2}^{(1)} & \underline{\mathbf{0}} & \cdots & & & \\ -\underline{\mathbf{Y}}_{2,1}^{(1)} & \left(\underline{\mathbf{Y}}_{2,2}^{(1)}+\underline{\mathbf{Y}}_{2,2}^{(2)}\right) & -\underline{\mathbf{Y}}_{2,3}^{(2)} & \underline{\mathbf{0}} & & & \\ \vdots & & & & & & \vdots \\ \underline{\mathbf{0}} & \cdots & -\underline{\mathbf{Y}}_{k,k-1}^{(k-1)} & \left(\underline{\mathbf{Y}}_{k,k}^{(k-1)}+\underline{\mathbf{Y}}_{k,k}^{(k)}\right) & -\underline{\mathbf{Y}}_{k,k+1}^{(k)} & \cdots & \underline{\mathbf{0}} \\ \vdots & & & & & & \vdots \\ & & & \underline{\mathbf{0}} & -\underline{\mathbf{Y}}_{N,N-1}^{(N-1)} & \left(\underline{\mathbf{Y}}_{N,N}^{(N-1)}+\underline{\mathbf{Y}}_{N,N}^{(N)}\right) & -\underline{\mathbf{Y}}_{N,N+1}^{(N)} \\ & & & & \underline{\mathbf{0}} & -\underline{\mathbf{Y}}_{N+1,N}^{(N-1)} & \left(\underline{\mathbf{Y}}_{N+1,N+1}^{(N)}+\underline{\mathbf{Y}}_{N+1,N+1}^{(N+1)}\right) \end{bmatrix} \times \begin{bmatrix} \mathbf{v}^{(1)} \\ \mathbf{v}^{(2)} \\ \vdots \\ \mathbf{v}^{(k)} \\ \vdots \\ \mathbf{v}^{(N)} \\ \mathbf{v}^{(N+1)} \end{bmatrix} = \begin{bmatrix} \mathbf{i}^{(1)} \\ \mathbf{i}^{(2)} \\ \vdots \\ \mathbf{i}^{(k)} \\ \vdots \\ \mathbf{i}^{(N)} \\ \mathbf{i}^{(N+1)} \end{bmatrix} . \quad (1$$

(4.35)

On-diagonal submatrices collect reactions among currents placed on the same interface, while off-diagonal submatrices are defined by interactions between adjacent interfaces. The tridiagonal block structure is due to the fact that only adjacent interfaces interact through the PPW in between them.

Numerical examples

Actually we are testing our formulation for the analysis of SIW microwave devices and antennas available in the scientific literature. The results are compared with numerical simulation performed with the finite elements commercial software Ansys HFSS^{TM} 15 and measurements when available. Two examples are shown below. For the reader's convenience the measured parameters taken from the original articles are also included.

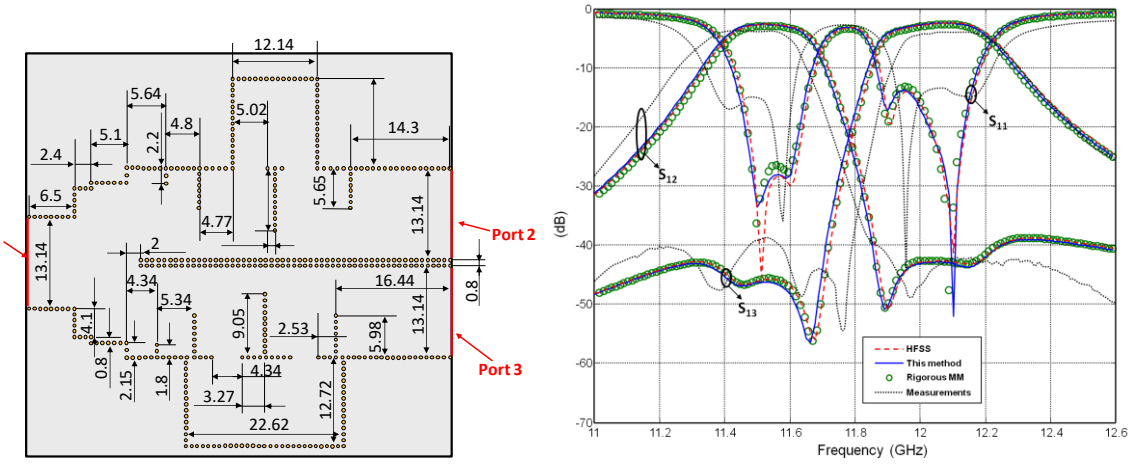

(a) (b)

Figure 4.10. (a) Geometry of the generalized Chebyshev SIW diplexer Physical parameters of the substrate: height h= 0.762 mm, relative permittivity ε_r=3.46, loss tangent tanδ= 0.0018. All dimensions are expressed in millimeters. (b) Comparison of the magnitude of the scattering parameters.

The first example is a large system implementing a generalized Chebychev diplexer [4.27]. The structure and the relevant geometrical parameters are given in Fig. 4.10a. The structure is composed by 414 copper posts and fed by 3 ports. The S-parameters of the structures computed with our method are compared to HFSS^{TM} simulations in Fig. 4.10b. A very good agreement is found among all these methods and the measurements performed in [4.27].

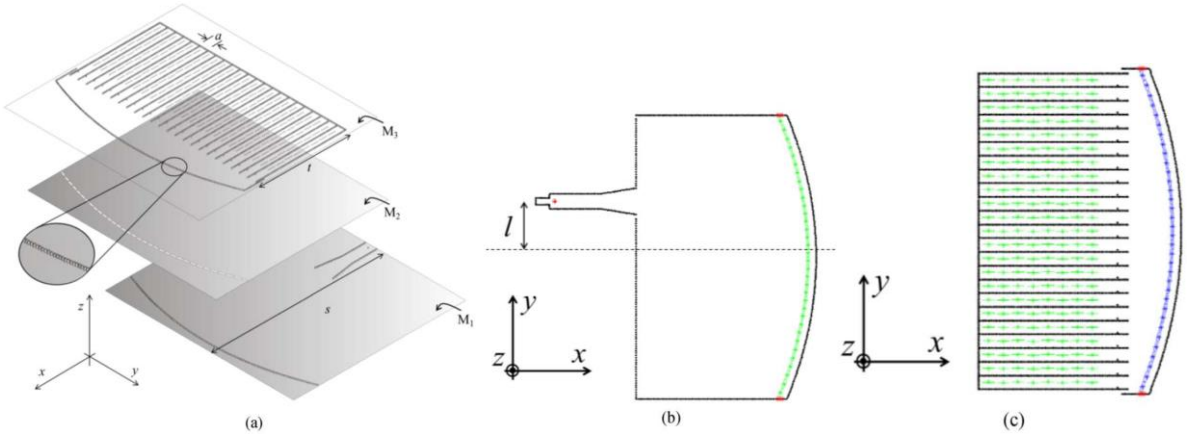

Figure 4.11. Pillbox structure in [P.20]. (a) Three-dimensional view (the slots along the 25 waveguides in the top PPW are etched in the uppermost metallic plate M_3, transparent in the picture). (b) Top view of the lower PPW (the green slots are on the common metallic plate M_2). (c) Top view of the upper PPW (the green slots are on the uppermost metallic plate M_3, the blue slots are on the common metallic plate M_2). The length shows the possible displacement of the horn from the central position to scan the beam. Main physical and geometrical parameters: a=5.7mm, t=63.2mm, s=117mm, thickness of both layers h=0.508mm, dielectric constant in both layers ε_r=2.2. The via-hole diameter is 0.4 mm, and their spacing is 0.8 mm. The average dimensions of the radiating slots are W=0.2mm, L=5.2mm. The dimensions of the coupling slots are W=1mm, L=3.6mm.

The second example is an SIW pillbox antenna, proposed in [P.20]. Its geometry is shown in Fig. 4.11a. It consists of two stacked PPWs filled by two identical Rogers 5880 substrates, having both permittivity ε_r=2.2 and height h=0.508mm. Top views of both the PPW environments are shown in Fig. 4.10(b) and (c). The structure is completely shielded at its edges by metallic vias connecting the metallic layers M_1 and M_3 in Fig. 4.11a. The stacked PPWs are coupled by means of 34 slots etched on the common plate and a parabolic reflector (quasi-optical system). The parabolic reflector is made by metal posts connecting the metallic layers and of the metallic vias connecting the metallic layers and in PPWs. There are 184 radiating slots etched on the uppermost plate; the structure is fed by a probe-fed integrated horn (realized with metallic pins) located in the lower PPW. The horn feed launches a TEM mode in the lower PPW. A total of 2896 posts are present in the complete structure. More details about the structure and fabrication process can be found in the caption of Fig. 4.10 and in [P.20]. The analysis of such a structure is a suitable test of the capabilities of the method because of its size and complexity. The far field computed with the code on two principal planes will be compared to HFSS simulations and measurements of a realized prototype [P.20]. In particular, in HFSS, despite the use of a powerful PC with 64 GB RAM memory, it was not possible to simulate the complete structure made by metallic pins. Indeed, several HFSS simulations have been performed in order to determine the parts of the structures that could be replaced by metallic walls with no loss of accuracy. As a result, the horn and the quasi-optical transition were made by perfect metallic sheets to reduce the computational effort; the total number of posts in the HFSS structure is therefore 2080. This process was quite time-consuming, and its results are frequency-dependent and not applicable to general structures. On the other hand, this analysis is not necessary for our code, which can handle the complete structure with no simplifications.

In Fig. 4.12, the computed normalized radiation patterns in the H- and E-planes are shown at 24.15 GHz, when the horn is placed in the central position [l=0 in Fig. 4.11(b)]. The number of modes and basis functions used for our code are the following: three vertical PPW modes (the TEM and the first higher-order TM and TE modes); three azimuthal modes in the field expansion for each post; three basis functions for magnetic currents on each slot. A very good agreement is observed between the approaches, whereas differences in the sidelobes can be attributed to slight differences in the definitions of the structures.

Fig. 4.13 shows the radiation patterns in the E-plane, only for two different frequencies (f=23GHz and f=24.5GHz), for the sake of brevity. The horn is placed in the central position. The patterns obtained with the code are compared this time both to HFSS simulations and measurements. In both cases, a very good agreement is found among the different approaches, confirming the validity of the proposed method. An important feature of the pillbox antenna is its scanning capability as the feeding horn is displaced along the y-axis in the focal plane of the parabola [see the parameter Fig. 4.11 (b)].

It is then of paramount importance to verify the correctness of the method when scanning the beam. Fig. 4.14 provides the normalized radiation patterns in E-plane at 24.1 GHz for three different positions of the feed horn with respect to the y-axis of the parabola (8.86, 17.72, and 26.58 mm). The main lobe of the pattern points at the elevation angles θ=8.6°,16.83°,25.74°, respectively. Only the E-plane is shown for the sake of brevity. The agreement of our code with measurements and HFSS results is remarkable.

In Table I, the computation time is compared between the HFSS simulations and these analyses. The advantage in terms of performance is evident. The data have been generated using a Personal Computer with a 2.8 GHz Intel I7 870 CPU, while the proposed methods have been implemented in Matlab™.

For the larger antenna problem, a large speedup factor is reached if we perform a single-frequency analysis or an optimization, for which a new meshing procedure is required at each step. In fact, optimization techniques for the fine tuning of these structures would not be possible with a general-purpose software due to its excessive simulation time and to the simplifications required in the model.

On the other hand, if a frequency sweep is performed, the meshing would have a smaller impact on the total HFSS time since it would be performed only once. However, the speedup ratio obtained when only the HFSS simulation time is present is still considerable.

The actual implementation of the codes does not take advantage of multi-core or multi-CPU systems, but it can be parallelized in the future.

This research is in collaboration with Dr. Guido Valerio (L2E) and Pr. Matteo Albani (University of Siena).

TABLE I

CPU SIMULATION TIME ON A XEON E5540 2.83 GHZ WITH 64 GBYTE RAM

Structure	Metallic / dielectric posts	Slots	HFSS		This paper
			Mesh	Freq. Point	
Cheb. diplexer	414 / 0	0	746 s	35 s	10.2 s
Simplified antenna	2080	218	29460 s	2860	-
Complete antenna	2896	218	Not possible		721 s

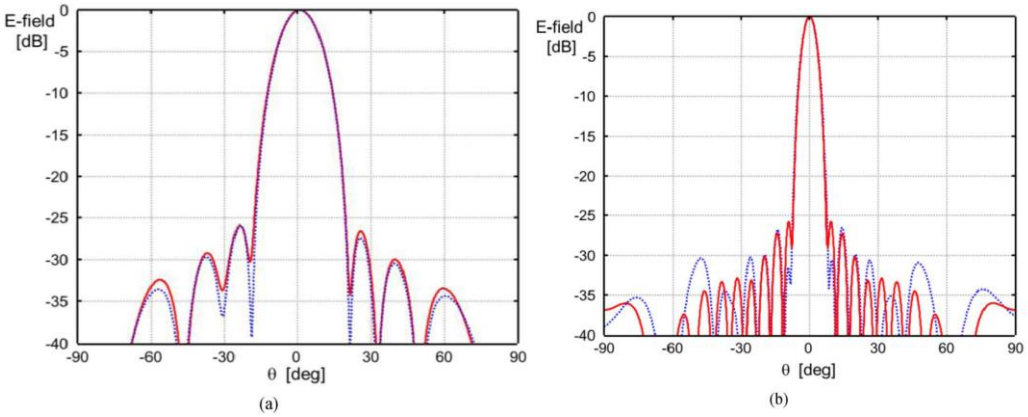

Figure 4.12. Normalized radiation patterns of the pillbox antenna with the feed horn in the central position (Fig. 10, with *l*=0) at 24.15 GHz. (a) H-plane. (b) E-plane. Approach proposed in this paper (*red lines*), and HFSS simulations (*blue lines*).

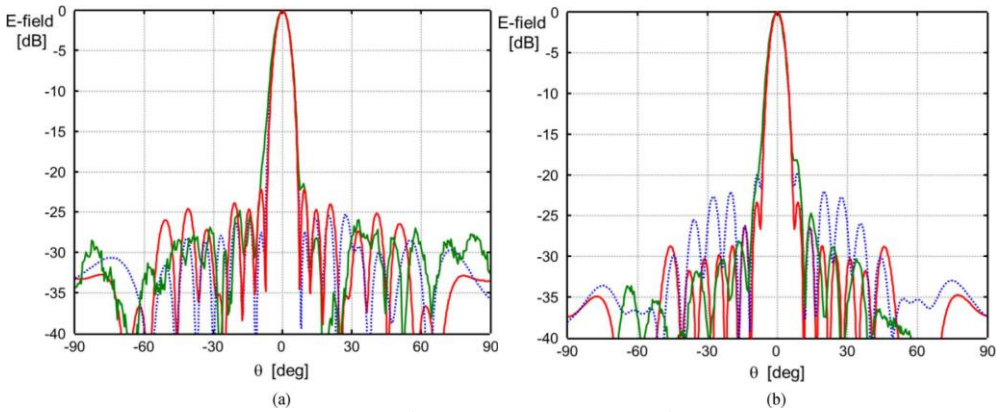

Figure 4.13. Normalized radiation patterns in the E-plane of the pillbox antenna with the feed horn in the central position (Fig. 10, with *l*=0). (a) *f*=23GHz. (b) *f*=24.5GHz. Code proposed in this paper (*red lines*), HFSS simulations (*blue lines*), and measured data (*green lines*).

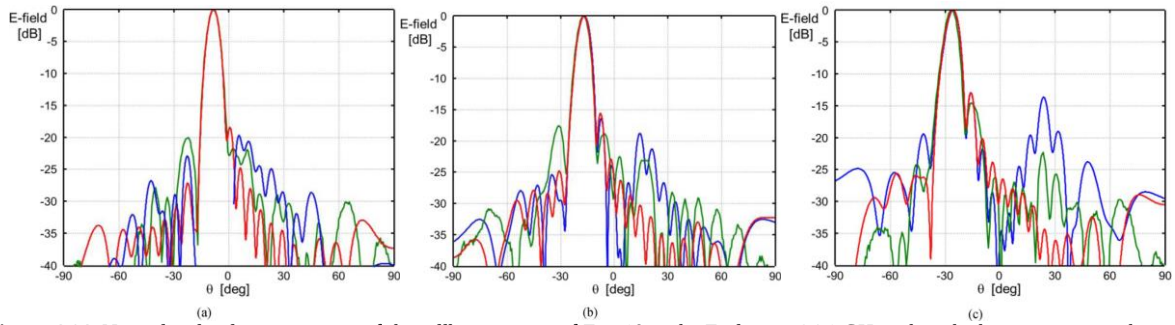

Figure 4.14. Normalized radiation patterns of the pillbox antenna of Fig. 10 in the E-plane at 24.1 GHz, when the horn position is changed. (a) *l*=8.86mm. (b) *l*=17.72mm. (c) *l*=26.58mm. Approach proposed in this paper (*red lines*), HFSS simulations (*blue lines*), and measured data (*green lines*).

Future works

In the next years several improvements will be implemented on the analysis tool:

- Introduction of triangular domain RWG basis functions leading to hybrid discretization of the structure. This will allow the analysis of general shape slots.
- As the antenna aperture increase, the number of unknown can become very large (especially with RWG). We know that the actual integral equation can lead to hill conditioned matrices. Thus, a numerical stability study will be performed, and if needed the integral equation will be modified (Combined Field Integral Equation)
- Introduction of realistic input port as for example microstrip port.
- Hybridization with a Finite Element Method. The introduction of *cylindrical region* ports described by cylindrical modes will allow the hybridization with other numerical techniques. In fact the cylindrical region could be simulated with a FEM and the field on the boundary expanded in cylindrical modes leading to a scattering matrix representation S. This matrix can be easily coupled with the S matrix of the *cylindrical region* ports obtained with the actual formulation. This procedure will allow the analysis of very heterogenic structure as for example a wideband transaction between coaxial cable and waveguide.

This activity will be performed within the framework of the ANR-ASTRID project Fast Hybrid Electromagnetic Modeling for the analysis of highly-integrated complex 3D Substrate Integrated Waveguide antenna front-ends (Fast-HEM-3DSIW).

4.1.2.2 Metasurface antennas

***List of related publications*: [P.2], [P.4], [P.10], [C.4], [C.9], [C.14].**

The properties of these surfaces are described in terms of surface impedances (or admittances) and dimensionless chirality tensors [4.28] (analogous to the constitutive parameters for volumetric metamaterials). Metasurfaces have been recently used in many applications like holographic antennas [4.29], leaky-wave antennas [P.25] [4.30]-[4.31],[P.10], planar lenses [4.32]-[4.33], orbital angular momentum communication [4.34], transformation optics [11]-[12] or polarization convertors [13]-[14].

Holographic and leaky-wave antennas are based on the propagation properties of waves over a local sinusoidally modulated impedance [4.39]. By choosing an appropriate modulation, it is possible to control the propagation of surface waves (SW) along a surface or to obtain the transition from SW to leaky wave (LW) modes in order to realize antennas [4.40]-[P.10].

Surfaces composed of sub-wavelength printed elements over grounded dielectric slabs were largely used in order to obtain modulated scalar impedances by locally changing the dimensions of the elements [3]-[4.43] [P.10]. Symmetric elements are used to produce scalar impedances [4.29]-[4.30],[P.25],[4.43],[P.10] while asymmetric elements can implement tensorial impedances by creating cross-pol field components [3],[22]-[24].

Scalar metasurface antennas can produce general polarized beams [4.29]-[4.30],[P.25],[4.43], [P.10]. However, the direction of the radiating aperture field (or the equivalent surface current) is dictated by the source [P.10]. This latter aspect limits the number of possible aperture field distributions that can be implemented.

Recently, tensorial metasurfaces were successfully used in antenna design that can radiate CP waves [4.29],[4.44] and isoflux shaped beam antennas for space applications [4.44],[4.45]. The additional degrees of freedom offered by tensorial metasurfaces could be used to overcome the limits of scalar solution by generalizing the procedure presented in [P.10].

The objective of the research is to propose a systematic procedure for the design of metasurface antennas capable of implementing a general aperture field distribution (amplitude, phase and polarization). The principal novelty of this approach is the independent control of the generated aperture field components. This important aspect (critical for general aperture implementation), can be achieved by introducing independent modulations of the impedance tensorial components and an exact formulation for the first order holography.

Background Physics

The surface impedance $\underline{\underline{\mathbf{Z}}}_{\mathbf{s}}$ is defined as the ratio between tangential electric ($\mathbf{E}_t$) and the magnetic ($\mathbf{H}_t$) fields at the surface boundary S for a particular wavevector ($\mathbf{k}^{\mathbf{sw}}$):

$$\mathbf{E}_t(\boldsymbol{\rho}')\big|_{\boldsymbol{\rho}'\in S} = \underline{\underline{\mathbf{Z}}}_{\mathbf{s}}\left(\mathbf{k}^{\mathbf{sw}}\right)\hat{\mathbf{n}}\times\mathbf{H}_t(\boldsymbol{\rho}')\Big|_{\boldsymbol{\rho}'\in S} = \underline{\underline{\mathbf{Z}}}_{\mathbf{s}}\mathbf{J}(\boldsymbol{\rho}') \tag{4.36}$$

where $\boldsymbol{\rho}' = \rho_u'\hat{\mathbf{u}} + \rho_v'\hat{\mathbf{v}}$ is a point on the antenna surface, $\hat{\mathbf{n}}$ is the vector normal to the surface, S and $\mathbf{J}(\mathbf{r}) = \hat{\mathbf{n}}\times\mathbf{H}_t(\mathbf{r})\big|_{\mathbf{r}\in S}$ is the equivalent surface current

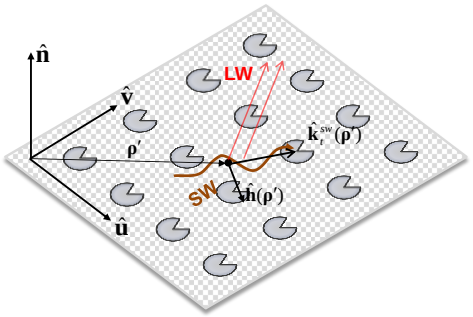

Figure 4.15. Metasurface geometry and leaky wave generation

Since we deal with surface waves (discrete spectrum), the impedance (4.36) is defined only for a discrete set of wavenumbers, namely:

$$\mathbf{k}^{\mathbf{sw}} = k_t^{sw}(n,\omega,\varphi)\hat{\mathbf{k}}_t^{sw} = k_t^{sw}(n,\omega,\varphi)\left(\hat{\mathbf{u}}\cos(\varphi)+\hat{\mathbf{v}}\sin(\varphi)\right) \tag{4.37}$$

where k_{sw} is the wavenumber associated with the *n*-th mode propagating along the direction $\hat{\mathbf{k}}_t^{sw}$ defined by the angle φ at the angular velocity ω.

The impedance boundary condition can be implemented using different approaches, however, in any case it takes into account all of the interaction effects between the wave and the structure and media below the *z*=0 plane (see Fig. 4.15).

We will focus our attention on the dominant mode (n=0) propagating on reciprocal lossless metasurfaces. Conservation of energy (anti-Hermitian impedance tensor $\underline{\underline{\mathbf{Z}}}_{\mathbf{s}}^{\dagger} = -\underline{\underline{\mathbf{Z}}}_{\mathbf{s}}$) in conjuction with reciprocity imply that $\mathbf{Z}_{\mathbf{s}}$ is a purely imaginary symmetric tensor [4.45].

Thus, in a general 2D orthogonal reference system placed on S, equation (4.36) is written as

$$\begin{bmatrix} E_u \\ E_v \end{bmatrix} = j\begin{bmatrix} X_{uu} & X_{uv} \\ X_{uv} & X_{vv} \end{bmatrix}\begin{bmatrix} -H_v \\ H_u \end{bmatrix} = j\begin{bmatrix} X_{uu} & X_{uv} \\ X_{uv} & X_{vv} \end{bmatrix}\begin{bmatrix} J_u \\ J_v \end{bmatrix}. \tag{4.38}$$

where the subscripts *u* and *v* refer to the components of the various quantities in the general framework.

In the following, we suppose that the incident SW is propagating along a general direction $\hat{\mathbf{k}}_t^{sw}$ on a metasurface placed in the x-y plane as shown in Fig. 4.15.

For tensorial surface impedances, the dominant SW mode is a hybrid EH mode. The magnetic field on the surface is assumed to be of the general form

$$\mathbf{H}_t(\boldsymbol{\rho}') = A(\boldsymbol{\rho}')e^{-j\mathbf{k}^{\mathbf{sw}}(\boldsymbol{\rho}')\cdot\boldsymbol{\rho}'}\hat{\mathbf{h}}(\boldsymbol{\rho}') \tag{4.39}$$

where A is the field amplitude, $\hat{\mathbf{h}}$ is the magnetic field polarization unit vector, $\mathbf{k}^{\mathbf{sw}} = k_t^{sw}\hat{\mathbf{k}}_t^{sw}$ is the wave vector and the propagation constant k_t^{sw} is found by solving the dispersion equation.

Let us consider a small modulation of the surface reactance components along the propagation direction of the form

$$X_{ij}(x) = \bar{X}_{ij}\left[1 + M_{ij}\cos\left(\frac{2\pi}{p_{ij}}x\right)\right] \tag{4.40}$$

where $\bar{X}_{ij}$, M_{ij} and p_{ij} are the average reactance, the modulation index and the periodicity of the *ij* component, respectively. It should be noted that the periodicities of the reactance components are not necessarily identical $p_{ij} \neq p_{kl}$.

Under the assumption of small perturbation of the average impedance values ($M_{ij} < 1$), eq.(4.39) can still be considered as a valid approximation of the magnetic field above the modulated impedance [4.29], [4.30], [P.24]. Thus, a first order estimation of the electric field with respect to small parameters M_{ij} can be obtained by replacing (4.39), (4.40) into (4.38) and writing the cosine term of (4.40) in the exponential form, leading to :

$$\begin{cases} E_u = j\left(\bar{X}_{uu}J_u + \bar{X}_{uv}J_v + \dfrac{M_{uu}}{2}\bar{X}_{uu}J_u e^{-j\frac{2\pi}{p_{uu}}x} + \dfrac{M_{uv}}{2}\bar{X}_{uv}J_v e^{-j\frac{2\pi}{p_{uv}}x} + \dfrac{M_{uu}}{2}\bar{X}_{uu}J_u e^{j\frac{2\pi}{p_{uu}}x} + \dfrac{M_{uv}}{2}\bar{X}_{uv}J_v e^{j\frac{2\pi}{p_{uv}}x}\right) \\ E_v = j\left(\bar{X}_{uv}J_u + \bar{X}_{vv}J_v + \dfrac{M_{uv}}{2}\bar{X}_{uv}J_u e^{-j\frac{2\pi}{p_{uv}}x} + \dfrac{M_{vv}}{2}\bar{X}_{vv}J_v e^{-j\frac{2\pi}{p_{vv}}x} + \dfrac{M_{vu1}}{2}\bar{X}_{vu}J_u e^{j\frac{2\pi}{p_{vu}}x} + \dfrac{M_{vv}}{2}\bar{X}_{vv}J_v e^{j\frac{2\pi}{p_{vv}}x}\right) \end{cases} \tag{4.41}$$

For each component of the electric field, the first line represents non radiative surface waves, while the terms of the second line can be leaky waves if $k_t^{sw} - 2\pi/p_{ij} < k_0$. As can be seen in eq.(4.41), the phase of the excited leaky waves can be controlled by the periodicity of the reactance p_{ij} while the amplitude is proportional to the product $\bar{X}_{ij}M_{ij}$.

The idea is to found a procedure to control the generated LW component of the field (4.41), namely

$$\mathbf{E}_t^{LW} = \begin{bmatrix} E_u^{LW} \\ E_v^{LW} \end{bmatrix} = j\begin{bmatrix} \dfrac{M_{uu}}{2}\bar{X}_{uu}J_u e^{-j\frac{2\pi}{p_{uu}}x} + \dfrac{M_{uv}}{2}\bar{X}_{uv}J_v e^{-j\frac{2\pi}{p_{uv}}x} \\ \dfrac{M_{uv}}{2}\bar{X}_{uv}J_u e^{-j\frac{2\pi}{p_{uv}}x} + \dfrac{M_{vv}}{2}\bar{X}_{vv}J_v e^{-j\frac{2\pi}{p_{vv}}x} \end{bmatrix} \tag{4.42}$$

in order to implement a desired objective radiating aperture field distribution:

$$\mathbf{E}_t^{obj} = \begin{bmatrix} E_u^{obj} \\ E_v^{obj} \end{bmatrix} = \begin{bmatrix} \left|E_u^{obj}\right| e^{j\arg(E_u^{obj})} \\ \left|E_v^{obj}\right| e^{j\arg(E_v^{obj})} \end{bmatrix} \tag{4.43}$$

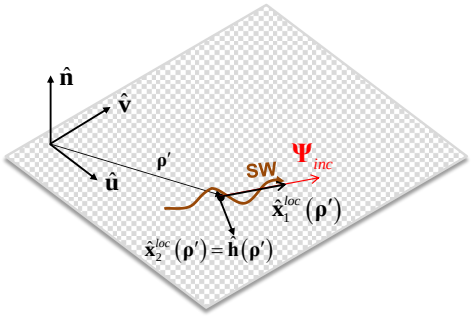

Figure 4.16. Local framework definition.

The easiest approache to obtain the desired phase distribution on the surface is to equate the phase of each individual term in (4.42) with the phase of (4.43) for every component.
Imposing this condition between each term of (4.42) with (4.43) leads to the following condition for the impedance periodicities:

$$p_{ij} = \frac{2\pi}{\arg\left(J_j\right) + \Pi_{ij} - \arg\left(E_i^{obj}\right)} \tag{4.44}$$

where $\Pi_{ij} = \pi\left(\mathrm{sgn}\left(\bar{X}_{ij}\right) - 1\right)/2$ and $\Pi_{uv} = \Pi_{vu}$.

The tensor impedance (4.40) with the periodicities given by (4.44) can be written in compact form if all of the average impedances $\bar{X}_{ij}$ have the same sign. In fact, by defining the *incident wave* $\mathbf{\Psi}_{inc}$ as the phase of the current $\mathbf{J}$, and the *objective wave* $\mathbf{\Psi}_{obj}$ as the phase terms of the objective electric field, namely:

$$\mathbf{\Psi}_{inc} = \begin{bmatrix} \Psi_1^{inc} \\ \Psi_2^{inc} \end{bmatrix} = \begin{bmatrix} e^{j\arg(J_1)} \\ e^{j\arg(J_2)} \end{bmatrix}, \quad \mathbf{\Psi}_{obj} = \begin{bmatrix} \Psi_1^{obj} \\ \Psi_2^{obj} \end{bmatrix} = \begin{bmatrix} e^{j\arg(E_1^{obj})} \\ e^{j\arg(E_2^{obj})} \end{bmatrix} \tag{4.45}$$

the modulated tensorial impedance is obtained as [P.2]:

$$\underline{\underline{\mathbf{Z}}}_{\mathbf{s}} = j\underline{\underline{\mathbf{X}}} + j\underline{\underline{\mathbf{X}}} \circ \underline{\underline{\mathbf{M}}}\, \Im\left(\Psi_{obj} \otimes \Psi_{inc}^{*}\right) \tag{4.46}$$

where $\underline{\underline{\mathbf{X}}}$ is the average reactance tensor, $\underline{\underline{\mathbf{M}}}$ is the modulation index matrice, $\otimes$ and $\circ$ are the outer and the Hadamard products respectively.

As stated before, $\underline{\underline{\mathbf{Z}}}_{\mathbf{s}}$ must be anti-Hermitian. This condition is not guaranteed by (4.46) as the off diagonal impedance elements depend on field parameters that can not be controled a priori (incident field and objective field). This problem arises because we are trying to impose the 4 conditions in (4.44) with only 3 degrees of freedom given by the impedance tensor.

A possible solution is to decompose the tensor (4.46) as the sum of its hermitian part $\underline{\underline{\mathbf{H}}}$ and its antihermiatian one $\underline{\underline{\mathbf{A}}}$ and then to use this latter as the impedance tensor. This choice, even if derived with a different approach, leads to the formulation presented in [4.29]. However, this technique does not garentee a perfect match between (4.42) and (4.43) because a significant part of the tensor that guarantee the exact phase (4.44) is neglected.

In this research, a second approach to overcome the above-mentioned problem is introduced. The idea is to equating the phase of the sum of the terms in (4.42) with the desired phase distribution (4.43). This is a quite complex problem because four impedance elements have to be controlled at the same time while maintaining the anti-hermitian property. In order to simplify this calculation, we take advantage of the fact that physical properties (energy conservation and reciprocity) are conserved under orthogonal transformations. At each point of the metasurface we define a local framework such that the magnetic field $\mathbf{H}_t\left(\boldsymbol{\rho}'\right)$ is directed along a local axis (Fig. 4.16). Such an orthogonal reference system can be defined as:

$$\begin{aligned} \hat{\mathbf{x}}_v^{loc}\left(\boldsymbol{\rho}'\right) &= \hat{\mathbf{h}}\left(\boldsymbol{\rho}'\right) \\ \hat{\mathbf{x}}_u^{loc}\left(\boldsymbol{\rho}'\right) &= \hat{\mathbf{x}}_v^{loc}\left(\boldsymbol{\rho}'\right) \times \hat{\mathbf{n}} \end{aligned}. \tag{4.47}$$

Thus, denoting by $\underline{\underline{\mathbf{R}}}\left(\boldsymbol{\rho}'\right)$ the transformation matrix from the global to the local framework, the local wave and impedance can be written as

$$\mathbf{E}_t^{loc}\left(\boldsymbol{\rho}'\right) = \underline{\underline{\mathbf{R}}}\left(\boldsymbol{\rho}'\right) \cdot \mathbf{E}_t\left(\boldsymbol{\rho}'\right) \qquad \mathbf{H}_t^{loc}\left(\boldsymbol{\rho}'\right) = \underline{\underline{\mathbf{R}}}\left(\boldsymbol{\rho}'\right) \cdot \mathbf{H}_t\left(\boldsymbol{\rho}'\right) \qquad \underline{\underline{\mathbf{Z}}}_s^{loc}\left(\boldsymbol{\rho}'\right) = \underline{\underline{\mathbf{R}}}\left(\boldsymbol{\rho}'\right) \cdot \underline{\underline{\mathbf{Z}}}_s\left(\boldsymbol{\rho}'\right) \cdot \underline{\underline{\mathbf{R}}}\left(\boldsymbol{\rho}'\right)^{-1} \tag{4.48}$$

In equation (4.48) and what follows, the superscript *loc* indicates that the quantity is written in the local framework.

In the local framework, eq.(4.38) becomes

$$\begin{bmatrix} E_u^{loc} \\ E_v^{loc} \end{bmatrix} = j \begin{bmatrix} X_{uu}^{loc} & X_{uv}^{loc} \\ X_{vu}^{loc} & X_{vv}^{loc} \end{bmatrix} \begin{bmatrix} -H_v^{loc} \\ 0 \end{bmatrix} = j \begin{bmatrix} X_{uu}^{loc} & X_{uv}^{loc} \\ X_{vu}^{loc} & X_{vv}^{loc} \end{bmatrix} \begin{bmatrix} J_u^{loc} \\ 0 \end{bmatrix} \tag{4.49}$$

As seen in equation (4.49), only the first column of $\underline{\underline{\mathbf{Z}}}_s^{loc}$ affects the electric field. The idea is to use eq. (4.46) in the local framework only for the elements of the first column, namely:

$$\begin{cases} X_{uu}^{loc} = \bar{X}_{uu}^{loc}\left[1+M_{uu}^{loc}\Im\left(\Psi_{obj,u}^{loc}\cdot\Psi_{obj,u}^{loc*}\right)\right] \\ X_{vu}^{loc} = \bar{X}_{vu}^{loc}\left[1+M_{vu}^{loc}\Im\left(\Psi_{obj,v}^{loc}\cdot\Psi_{obj,u}^{loc*}\right)\right] \end{cases}. \tag{4.50}$$

We can now ensure that $\underline{\underline{\mathbf{Z}}}_{\mathbf{s}}$ is anti-Hermitian by imposing $X_{uv}^{loc} = X_{vu}^{loc}$ as this component does not affect the electric field. In addition, X_{vv}^{loc} is a free quantity that we can use for other design purposes.
Finally, the impedance in the global framework that allows a phase match between the incident wave and the objective wave is obtained as

$$\underline{\underline{\mathbf{Z}}}_{\mathbf{s}}(\boldsymbol{\rho}') = \underline{\underline{\mathbf{R}}}(\boldsymbol{\rho}')\, j\begin{bmatrix} X_{uu}^{loc}(\boldsymbol{\rho}') & X_{vu}^{loc}(\boldsymbol{\rho}') \\ X_{vu}^{loc}(\boldsymbol{\rho}') & X_{vv}^{loc}(\boldsymbol{\rho}') \end{bmatrix}\underline{\underline{\mathbf{R}}}(\boldsymbol{\rho}')^{-1}. \tag{4.51}$$

As a final remark, it can be noted that eq.(4.51) has apparently 3 degrees of freedoms $\left(\bar{X}_{vv}^{loc}, M_{uu}^{loc}, M_{vu}^{loc}\right)$. However, since $\bar{X}_{vv}^{loc}$ affects the propagation constant k_t^{sw}, it cannot be arbitrarily selected.

Amplitude synthesis is based on a proper choice of the free parameters of eq.(4.51). As described before, the amplitude of the LW is proportional to the product $\bar{X}_{ij}M_{ij}$. Thus, the idea is to change this product along the metasurface in order to compensate the spreading factor of the SW and obtain an amplitude behavior proportional to that of the objective field.

As a result, the average reactance and the modulation index of each component of the impedance will vary depending on the position on the metasurface. Eqs.(4.42),(4.43) imply that the following conditions have to be verified

$$\begin{cases} \bar{X}_{11}^{loc}(\boldsymbol{\rho}')M_{11}^{loc}(\boldsymbol{\rho}')\left|H_2^{loc}(\boldsymbol{\rho}')\right| \propto \left|E_{obj,1}^{loc}(\boldsymbol{\rho}')\right| \\ \bar{X}_{12}^{loc}(\boldsymbol{\rho}')M_{12}^{loc}(\boldsymbol{\rho}')\left|H_2^{loc}(\boldsymbol{\rho}')\right| \propto \left|E_{obj\,2}^{loc}(\boldsymbol{\rho}')\right| \end{cases} \tag{4.52}$$

Eq. (4.52) imposes the product $\bar{X}_{ij}^{loc}M_{ij}^{loc}$ but not their individual values. However, since the dispersion constant k_t^{sw} is affected mainly by the average reactances values, smooth continuous variations of these have to be imposed to avoid undesired reflections.

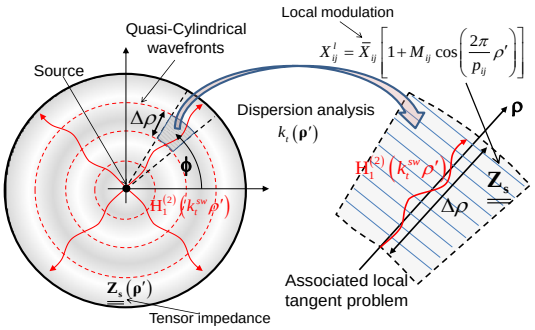

Figure 4.17. Dividing the metasurface into sectorial areas with mono-directional propagation.

In order to estimate the magnetic field needed in eqs.(4.51),(4.52), a Geometrical Optic (GO)-based procedure is introduced [P.10]. The idea is to consider the modulated impedance as a double-scale problem, with a rapid variation rate (with respect to the wavelength) given by the sinusoidal modulation ($p_{ij} < \lambda$) and a slower variation given by the space dependence of the modulation parameters (M_{ij} $\bar{X}_{ij}$, and p_{ij}). Under optic

approximation, the fast impedance variation can be described by an equivalent impedance obtained using the local periodic dispersion [P.10]. Thus, the modulated metasurface can be assimilated to a continuous slowly-variating equivalent surface impedance. It is important to note that even the metasurface is lossless; the equivalent impedance has a real part (resistance) describing the energy loss due to leaky wave radiation.
In order to numerically solve the propagation problem, the metasurface is divided into sectorial areas where propagation can be considered mono-directional (Fig. 4.17). Then, each sectorial area is divided into various subdomains along the propagation direction, in which the impedance modulation (18) is assumed to be constant ($\bar{X}_{ij}$, M_{ij} and p_{ij} are constants). A new procedure able to analytically solve the propagation problem within each subdomain has been introduced (next subsection). The global solution is obtained by imposing the continuity of tangential field across each domain.

Local dispersion Analysis

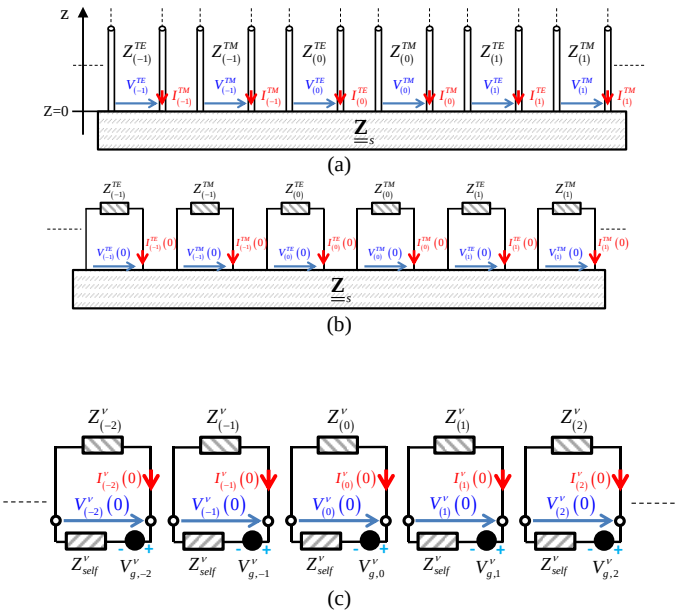

Figure 4.18: (a) Equivalent transmission line problem for $z>0$. (b)(c) Equivalent circuit at $z=0$.

The propagation problem over a periodically modulated surface can be interpreted as shown in Fig. 4.18(a), where an infinite number of independent transmission line along the normal direction (one for each Floquet mode *n* and polarization state) are coupled together at the impedance surface.
The transmission line propagation constants and characteristic impedances are given by

$$k_z^{(n)} = \sqrt{k^2 - k_x^{(n)2}} = \sqrt{k^2 - \left(k_x^{(0)} + n\left(2\pi/p\right)\right)^2}\,, \qquad Z_{(n)}^{TM} = \zeta k_z^{(n)}/k \qquad Z_{(n)}^{TE} = \zeta k/k_z^{(n)} \tag{4.52}$$

where $k = \sqrt{\varepsilon\mu}$ is the wavenumber associated to the medium above the impedance and ζ the corresponding wave impedance.
At the impedance level (z=0) the circuit can be simplified as in Fig.4.18(b), where the infinite transmission lines have been replaces by their corresponding line impedances.
Boundary condition implies the following relation between electric and magnetic field:

$$\mathbf{E}_t\big|_{z=0} = \underline{\underline{\mathbf{Z}}}_s \cdot \left(\hat{\mathbf{n}} \times \mathbf{H}_t\big|_{z=0}\right), \tag{4.53}$$

where the field and the impedance tensor are expressed in the TM/TE framework, namely

$$\begin{bmatrix} V_{TM} \\ V_{TE} \end{bmatrix} = \begin{bmatrix} Z_{TM,TM} & Z_{TM,TE} \\ Z_{TE,TM} & Z_{TE,TE} \end{bmatrix} . \begin{bmatrix} I_{TM} \\ I_{TE} \end{bmatrix} . \tag{4.54}$$

Each component of the surface impedance tensor is supposed of the following general form

$$Z^{\nu,\kappa}(x) = j\bar{X}_s^{\nu,\kappa}\left(1 + M^{\nu,\kappa} f^{\nu,\kappa}(x)\right), \tag{4.55}$$

where ν,κ =TE/TM, $\bar{X}_s^{\nu,\kappa}$ is the average value of surface reactance, $M^{\nu,\kappa}$ <1 is the modulation index and $f^{\nu,\kappa}$ is a periodic function with period $p_{\nu,\kappa}$.

If the periods $p_{\nu,\kappa}$ are multiple of a same period *p*, the problem is still periodic, thus it can be interpreted as composed by a discrete infinite number of independent transmission lines. The only difference with respect to the scalar case is that lines with different polarizations (TE/TM) are coupled together.

In the following we will call this particular framework *the canonical basis* because eqs.(4.53)-(4.55) directly establish a relation between electrical quantities defined in different transmission lines (in general with different polarization state).

Each periodic function $f^{\nu,\kappa}$ in (4.55) is expressed as Fourier series expansion

$$f^{\nu,w}(x) = \sum_{n=-\infty}^{\infty} c_n^{\nu,\kappa} e^{-jn\frac{2\pi}{p_{\nu,\kappa}}x}, \tag{4.56}$$

then, using (4.56) in (4.55) leads to

$$Z^{\nu,\kappa}(x) = Z_{self}^{\nu,\kappa} + \sum_{m=-\infty}^{\infty} Z_{cross,\mathrm{m}}^{\nu,\kappa} e^{-jm\frac{2\pi}{p_{\nu,\kappa}}x}, \tag{4.57}$$

where the following quantities have been introduced:

$$\begin{aligned} Z_{self}^{\nu,\kappa} &= j\bar{X}_s^{\nu,\kappa} \\ Z_{cross,\mathrm{m}}^{\nu,\kappa} &= j\bar{X}_s^{\nu,\kappa} M^{\nu,\kappa} c_n^{\nu,\kappa} \end{aligned} \tag{4.58}$$

Using eqs.(4.56)-(4.58) in boundary condition (4.55) lead to the form:

$$\begin{aligned} V_n^{TM}(0) &= Z_{self} I_n^{TM}(0) + V_{g(n)}^{TM} \\ V_n^{TE}(0) &= Z_{self} I_n^{TE}(0) + V_{g(n)}^{TE} \end{aligned} . \tag{4.59}$$

where

$$\begin{aligned} V_{g(n)}^{TM} &= Z_{self}^{TM,TE} I_n^{TE} + \sum_{\substack{m=-\infty \\ m\neq n}}^{\infty} Z_{c,-m}^{TM,TE} I_{n+m}^{TE} + \sum_{\substack{m=-\infty \\ m\neq n}}^{\infty} Z_{c,-m}^{TM} I_{n+m}^{TM} \\ V_{g(n)}^{TE} &= Z_{self}^{TM,TE} I_n^{TM} + \sum_{\substack{m=-\infty \\ m\neq n}}^{\infty} Z_{c,-m}^{TM,TE} I_{n+m}^{TM} + \sum_{\substack{m=-\infty \\ m\neq n}}^{\infty} Z_{c,-m}^{TE} I_{n+m}^{TE} \end{aligned} \tag{4.60}$$

Eq. (4.59) explains how a general modal circuit in the representation of Fig. 4.18(a) is coupled with all the other modes. Using circuit formalism, condition (4.59) states that in each modal circuit, the boundary condition is equivalent to the impedance Z_{self}^{ν} connected to a controlled voltage source $V_{g,n}^{\nu}$ (Fig.4.18(c)).

An effective impedance (of the homogenized problem for a particular mode) can be defined as

$$\begin{aligned} Z_{eff,\mathrm{n}}^{TM} &= Z_{self}^{TM} + V_{g,\mathrm{n}}^{TM} / I_n^{TM} \\ Z_{eff,\mathrm{n}}^{TE} &= Z_{self}^{TE} + V_{g,\mathrm{n}}^{TE} / I_n^{TE} \end{aligned} . \tag{4.60}$$

The dispersion can be calculated using (4.58)-(4.60) the resonance condition:

$$Z^{v}_{eff,n}\left(k_x\right)+Z^{v}_{n}\left(k_x\right)=0\,, \tag{4.61}$$

where the effective impedance $Z^{v}_{eff,\mathrm{n}}$ (shown in Fig.3(c)) is defined as

$$Z^{v}_{eff,n}=Z^{v}_{self}+V^{v}_{g,n}\big/I^{v}_{n}\,. \tag{4.62}$$

This procedure leads to:

$$\begin{cases} I^{TM}_{n}\left(Z^{TM}_{\mathrm{n}}+Z^{TM}_{self}\right)+Z^{TM,TE}_{self}I^{TE}_{n}+\sum\limits_{\substack{m=-\infty\\ m\neq n}}^{\infty}Z^{TM,TE}_{c,-m}I^{TE}_{n+m}+\sum\limits_{\substack{m=-\infty\\ m\neq n}}^{\infty}Z^{TM}_{c,-m}I^{TM}_{n+m}=0 \\ I^{TE}_{n}\left(Z^{TE}_{\mathrm{n}}+Z^{TE}_{self}\right)+Z^{TM,TE}_{self}I^{TM}_{n}+\sum\limits_{\substack{m=-\infty\\ m\neq n}}^{\infty}Z^{TM,TE}_{c,-m}I^{TM}_{n+m}+\sum\limits_{\substack{m=-\infty\\ m\neq n}}^{\infty}Z^{TE}_{c,-m}I^{TE}_{n+m}=0 \end{cases}. \tag{4.63}$$

Eq. (4.63) can be rewritten in matrix form as $\underline{\underline{\mathbf{M}}}\cdot\mathbf{I}=0$ where $\mathbf{I}=\left[\ldots I^{TM}_{n-1}\quad I^{TE}_{n-1}\quad I^{TM}_{n}\quad I^{TE}_{n}\quad I^{TM}_{n+1}\quad I^{TE}_{n+1}\ldots\right]^{T}$,

$$\underline{\underline{\mathbf{M}}}=\begin{bmatrix} & & & \vdots & & & \\ \ldots & A^{TM}_{n-1} & Z^{TM,TE}_{self} & Z^{TM,TE}_{c,-1} & Z^{TM}_{c,-1} & Z^{TM,TE}_{c,-2} & Z^{TM}_{c,-2} \\ & Z^{TM,TE}_{self} & A^{TE}_{n-1} & Z^{TM,TE}_{c,-1} & Z^{TE}_{c,-1} & Z^{TM,TE}_{c,-2} & Z^{TE}_{c,-2} \\ & Z^{TM}_{c,1} & Z^{TM,TE}_{c,1} & A^{TM}_{n} & Z^{TM,TE}_{self} & Z^{TM,TE}_{c,-1} & Z^{TM}_{c,-1} \\ \ldots & Z^{TM,TE}_{c,1} & Z^{TE}_{c,1} & Z^{TM,TE}_{self} & A^{TE}_{n} & Z^{TM,TE}_{c,-1} & Z^{TE}_{c,-1} & \ldots \\ & Z^{TM}_{c,2} & Z^{TM,TE}_{c,2} & Z^{TM}_{c,1} & Z^{TM,TE}_{c,1} & A^{TM}_{n+1} & Z^{TM,TE}_{self} \\ & Z^{TM,TE}_{c,2} & Z^{TE}_{c,2} & Z^{TM,TE}_{c,1} & Z^{TE}_{c,1} & Z^{TM,TE}_{self} & A^{TE}_{n+1} \\ & & & \vdots & & & \end{bmatrix} \tag{4.64}$$

and $A^{v}_{n}=Z^{v}_{\mathrm{n}}+Z^{v}_{self}$.

The non-trivial solutions of eq.(4.64) are obtained imposing $\det\underline{\underline{\mathbf{M}}}=0$.

Alghoritm

Figure 4.19 summarizes the design steps needed to implement a given objective electric field distribution.

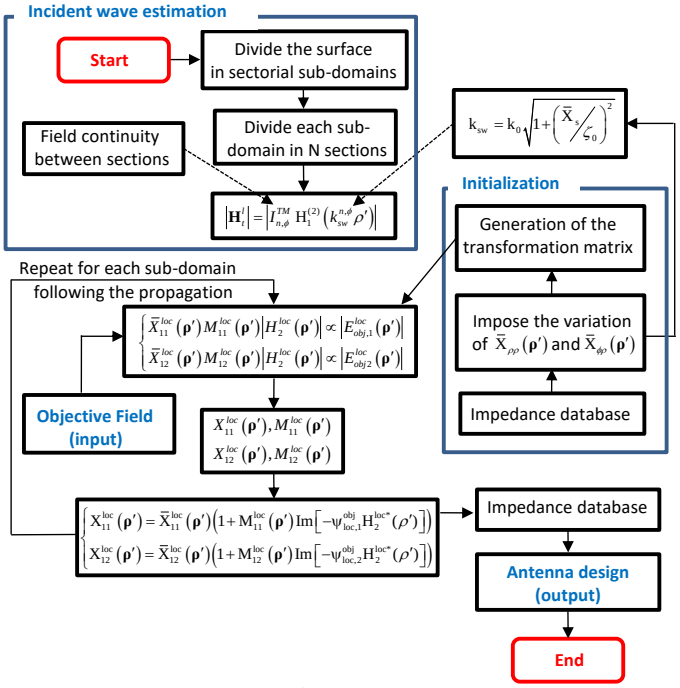

Figure 4.19. Metasurface implementation algorithm.

- Step 1: The average impedances variations laws and the maximum values of the modulation indexes are found by ensuring that the reactance values are available in the database.
- Step 2: The incident surface wave is evaluated by decomposing the metasurface into various subdomains along the propagation direction, in which the surface modulation is assumed to be constant. For a cylindrical SW the metasurface is devided into angular sub-domains, each sub-domain is then divided into N elementary radial sections.

Next, starting from the source and following the propagation, the following steps are performed on each sector:

- Step 3: The propagation constant $k_{t,n,\phi}^{sw}$ is found by solving the local dispersion problem, then amplitude and phase of the magnetic field are found imposing tangential field continuity at sector interface.
- Step 4: The transformation matrix $\underline{\underline{\mathbf{R}}}(\boldsymbol{\rho}')$ is found, the incident and the objective fields are then written in the local framework.
- Step 7: Modulation indexes $M_{11}^{loc}(\boldsymbol{\rho}')$ and $M_{12}^{loc}(\boldsymbol{\rho}')$ are calculated using equation (4.52).
- Step 8: Impedance variations are obtained using equations (4.51) (Holography principle) and (4.52).
- Step 9: The metasurface is discretized according to the selected periodic lattice. Following this, the metasurface layout is obtained by selecting the corresponding patch geometry available in the database.

Impedance design

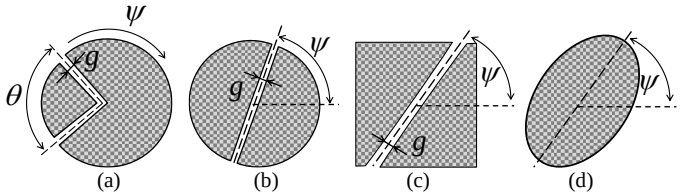

Figure 4.20. Unit cell topologies. The chosen cell (a) consists of a circular patch with a v shaped slot. It is defined by slot wideness g, the orientation angle ψ and the slot aperture angle θ.

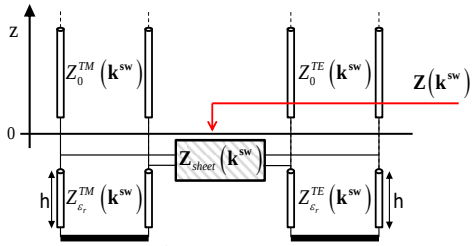

Figure 4.21. Printed metasurface equivalent TM and TE transmission lines.

The obtained surface impedance law $\underline{\underline{\mathbf{Z}_s}}(\boldsymbol{\rho}')$ can be implemented by printing asymmetric subwavelength patches in a squared lattice over a dielectric substrate as already proposed in [4.29] and [4.44]-[4.46].

An in-house tool based on periodical Method of Moment is used to characterize the surface impedance taking into account all the possible dispersion effects (dielectric slab dispersion, etc..). First, the resonating wavenumber $\mathbf{k}^{sw}$ associated to the dominant guided wave is found. Then, the sheet impedance $\mathbf{Z}_{sheet}(\mathbf{k}^{sw})$ (see Fig.4.21) associated to this particular wavenumber is calculated. Finally, the impenetrable impedance $\mathbf{Z}(\mathbf{k}^{sw})$ is obtained by adding the contribution of the grounded dielectric slab at the resonant wavenumber.

Several patch topologies were investigated to find the geometry able to ensure the highest reactance variation range. In order to have independent control of reactance component variations, a large range of impedance values is needed. This can be obtained by adding degrees of freedom to the cell geometry. As a result, a new geometry, composed of a circular patch with a variable v-shaped slot (Fig. 4.20a) is introduced.

This geometry can produce variable cross-reactance values acting mainly on the slot opening angle θ. This additional degree of freedom leads to a four-dimensional database (incident angle, patch dimension, patch orientation angle ψ, and slot opening angle θ) that will significantly increase the design possibilities offered by this unit cell.

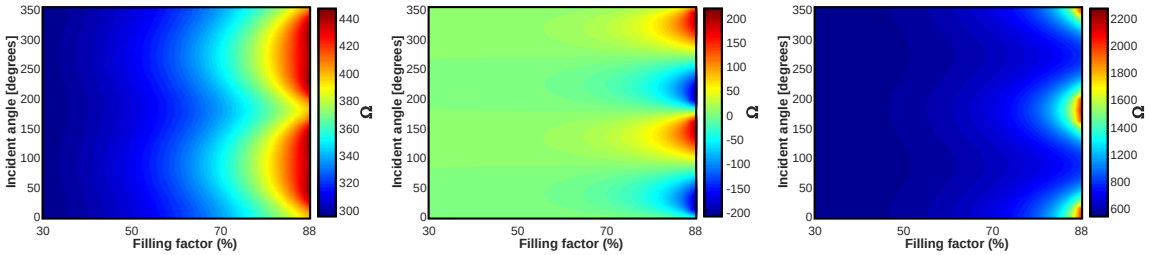

Figure 4.22. Reactance levels corresponding to the unit cells of angles $\theta = 60°$ and $\psi = 0°$ printed over a substrate TMM6 of permittivity 6 and thickness 1.27mm : $X_{\rho\rho}$ (a), $X_{\phi\rho}$ (b), and $X_{\phi\phi}$ (c).

It is important to stress that, since the cell is asymmetrical and the lattice is squared, a rotation ψ of the cell is not equivalent to a change of the incident angle of the SW on the patch lattice. As a result, impedance depends on the orientation angle ψ .

An example of impedance values obtained with the new patch geometry at 20GHz is shown in Fig.4.22. The periodic cells of dimension $\lambda_0/12$, where λ_0 is the free space wavelength, are printed on a Rogers TMM6 substrate with relative permittivity $\varepsilon_r = 6$ and thickness $h = 1.27\text{mm} = 0.207\lambda$. The plots show the impedance as a function of the incident angle (vertical axis) and the ratio between the patch radius and the lattice dimensions (horizontal axis) for $\theta = 60°$ and $\psi = 60°$.

This research is in collaboration with Pr. Hélène Roussel (L2E).

Future research

The research in the next years will be focalized on three important aspects: minimization of two undesired effects as (a) the limited bandwidth and (b) the impact of the feeder on the radiation diagram, and (c) the development of a numerical tool for the analysis of realistic metasurface antennas.

Limited bandwidth. Metasurface antennas present a limited bandwidth (roughly 7%). This is essentially due to the interaction between the surface-wave and the periodic structure. While the period of the printed element is constant with respect to the frequency, the SW propagation constant has to obey to the loaded dielectric slab dispersion equation. As a result, the interaction between SW and periodic structure is strongly frequency dependent.

Possible solution: the optimal solution will be the control of the dispersion curve of the guided mode. Multiple solutions are possible as for example: 1) introduction of additional artificial surfaces in order to control the dispersion of the surface wave; 2) use of ad-hoc quasi-resonant element. Other approaches will be tested as for example the use of multiple periodicities in the definition of the metasurface basic element.

Impact of the feeder on the radiation diagram. A strong hypothesis in the metasurface antenna design procedure is the availability of a *perfect* surface-wave launcher. Typical SW-launchers used in the literature are composed by small circular patches excited by pins. These structures excite the desired SW but also a spatial-wave that affect the radiation pattern of the antenna. This effect is more important in tensorial solutions where the SW is a hybrid mode, since the field polarization is no more conformal to the patch geometry as for scalar solutions.

Possible solution: In my opinion this aspect cannot be addressed in methodic way using commercial software because numerical methods as FEM (Finite Element Method), etc. cannot separate each physical contribution of the total field. In contrast, a theoretical approach based on Green's function of the "loaded" dielectric slab can be used to decompose the radiated field into surface and spatial wave. This will allow the use of some geometrical optimization technique in order to maximize the power associated to the surface wave.

Realistic antenna analysis. Metasurface antenna are electrically large, moreover the patch's small geometrical details leads to very fine mesh that have a strong negative impact on the computational time and the numerical stability. At the moment, it is very hard (or impossible) simulate a final design of such antennas with commercial software using a workstation with more than 128Gbyte of memory.

Possible solution: Integral equation (IE) - Method of moments (MoM) is particularly suitable for the analysis of printed structure since the availability of the dielectric slab Green's functions that allows limiting the presence of

unknowns on the metallic elements surface. A possible solution is to use IE-MoM in association with the Synthetic Function Expansion (SFX) compressive domain decomposition method. SFX method, developed at the Politecnico di Torino, belongs to a class of domain decomposition (DD) full-wave methods that end up in drastically reducing the actual size of the final MoM algebraic problem. The overall large problem is addressed by DD, thus the actual size of the final MoM matrix is reduced by grouping basis functions into "aggregate functions" defined over sub-domains, i.e., portions of the structure that are significantly larger than one cell of the initial mesh. The main advantage of SFX over other similar techniques as Characteristic Basis Function Method (CBFM) is the ability to include the strong near-field interactions between the different blocks of the structure under analysis. This latter aspect is crucial in metasurface application where the surface is excited by a surface-wave (near-field interaction).

4.1.2.3 Reflective and transmissive surfaces

***List of related publications*: [P.9], [C.7], [C.19].**

At very high frequencies, as for THz applications, a reflector or a lens are suitable structures that can be used to implementing the aperture field distribution. The basic idea is to illuminate the above mentioned structures with a source, and to handle the phase of the reflected/transmitted field as shown in Fig.4.23. Although we have investigated both, at THz frequencies, metallic reflectors are very efficient because of their extremely low losses.

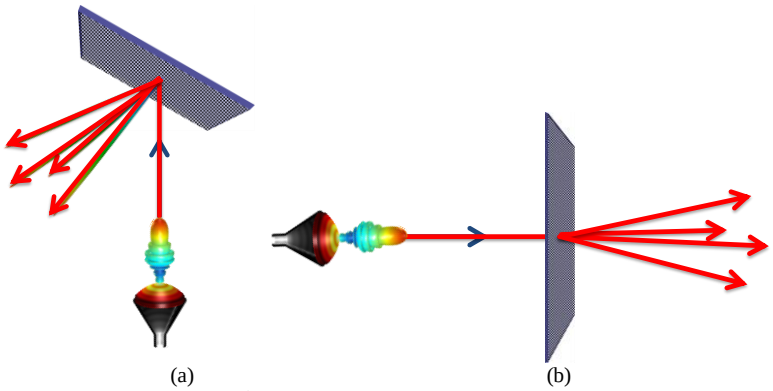

(a) (b)

Figure 4.23 Reflective(a) and transmissive (b) phase gratings

The drawback of this implementation is that only the phase can be synthetized, while the amplitude is fixed by the source generating the incident field. In order to overcome this limitation, the optimization loop has to be changed as shown in Fig. 4.24 in order to take into account this constraint.

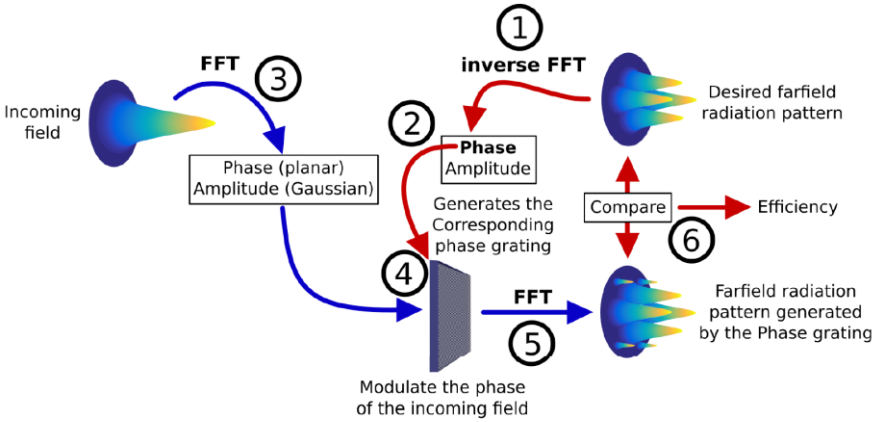

Figure 4.24: Schematic of the program calculating the phase profile of the Global grating

Once the optimal distribution is found the phase can be synthetized by optical consideration as follow:

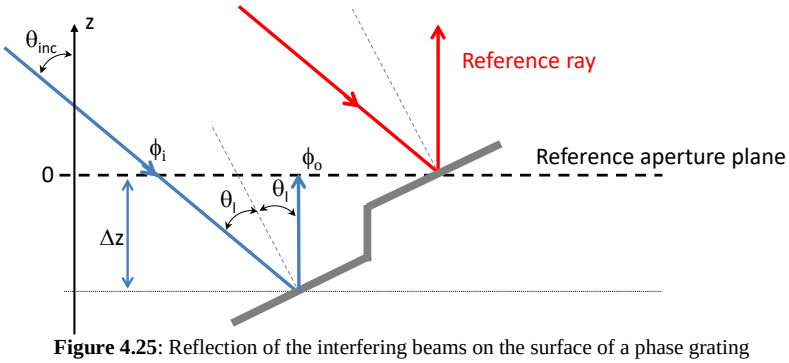

Figure 4.25: Reflection of the interfering beams on the surface of a phase grating

(A) Reflection. In order to correctly generate the aperture field, all the reflected rays should be parallels to the surface normal (the electric field vector lays correctly in the aperture plane) and its phase modified by the path lengths. The reflector geometry is shown in Fig. 4.25. The incoming rays are arriving with an angle θ_{inc} with respect to the aperture normal vector. Each facet of the reflector is inclined of an angle equal to $\theta_{inc}/2$ in order to generate the reflected ray in the desired direction. Then, the distance Δz is selected in such a way to obtain the desired phase shift $\Delta\phi=\phi_o-\phi_i$:

$$\Delta z = \frac{\Delta\phi}{k_0\left(1+\cos\theta_{inc}\right)} \tag{4.65}$$

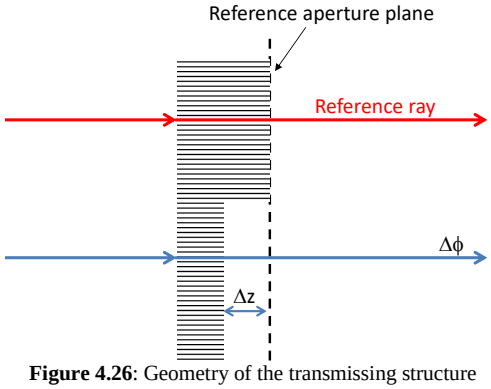

Figure 4.26: Geometry of the transmissing structure

(B) Transmission. The geometry of the transmissive structure is shown in Fig. 4.26. The relief of the transmissive grating modifies the phase front of the incoming beam because its refractive index is different from the refractive index of the air. So, a phase shift is introduced between different rays which do not travel along the same distance inside the structure. A desired phase shift with respect to the reference ray can obtained selecting the height of the dielectric relief as

$$\Delta z = \frac{\Delta\phi}{k_0\left(n_d-1\right)} \tag{4.66}$$

where n_d is the refractive index of the dielectric.

The obtained structures has been called Global phase grating [P.9].

Analysis Tool

In general a Gaussian beam is used as incident field over the phase grating. However, commercial electromagnetic software does not handle Gaussian source. For this reason a Physical Optics (PO) analysis tool has been developed. This latter allows the simulation of very large structures in a reasonable time. An example of a randomly generated reflector is shown in Fig. 4.27. The incident wavevector is depicted in blue, while the field polarization is in red. In the actual version a simple version of shadowing has been implemented (shadowed parts are in black).

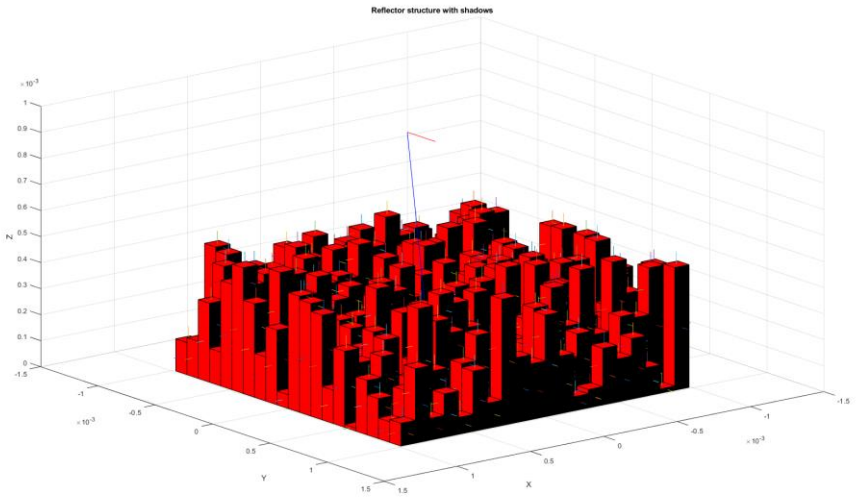

Figure 4.27: Shadowing of the PO analysis

Future work

The next step will be to improve the geometrical optics expression (4.65) for the shape of the reflector. The idea is to use eq.(4.65) as starting point for a geometry optimization based on the available analysis tool. Since this kind of surface can be seen as composed by a multitude of *cavities* (see Fig.4.27), the PO code will be improved implementing an Iterative Physical Optics scheme (IPO). This technique is the iterative refinement of first-order PO surface currents to incorporate higher-order multi-bounce and multiple diffraction effects.
Due to the local coupling of each cell (the average reflector is flat) an alternative approach could be the analysis of the *local environment* of each cell (a small portion of the reflector around the desired cell) using a full-wave IE-MoM.

Another solution that will be investigated is to replace the dielectric transmissive grating approach with a transmitarray. To do so, different dielectric layers with printed metallic periodic elements will be used (see Fig.4.28a). Each unit cell must introduce a certain phase shift between the incident plane wave and the transmitted field, while minimizing the reflection of the incident field. The value of the impedances can be determined by an optimization using transmission line theory. Then, the metallic patterns will be designed to achieve the calculated impedances. A preliminary test for an operation at 600 GHz has been fabricated using the process available by our colleagues at LERMA (Dr. Martina Wiedner). A triple layer structure as shown in figure 4.28(a) has been realized, the final structure is shown in Fig. 4.28(c). Fig. 4.28(b) shows a simulation that illustrates the focusing capability of the transmit array. The measurements are currently on-going.
A PhD student is expected to start in September 2018. The funding comes from the CNES (French Space Agency) and the projects are led by Dr. Martina Wiedner.

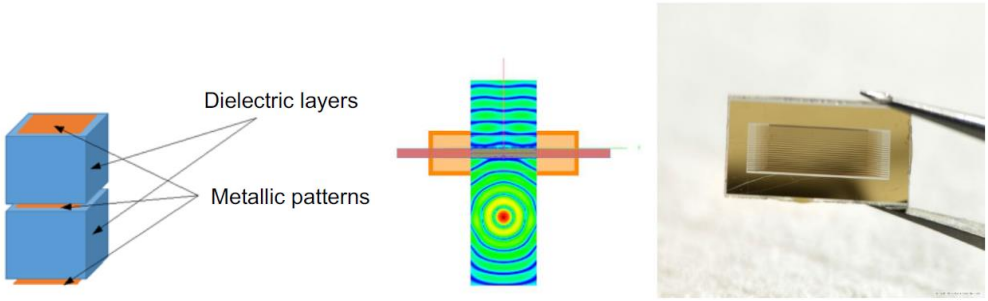

Figure 4.28 (a) Schematic of the transmit array (b) Simulation of the focusing power of the transmit array (c) Photgraphy of the fabricated prototype

4.1.2.4 Antenna optimization

***List of related publications*: [P.2], [P.6], [P.9], [P.10], [P.14], [P.16].**

This section presents the application of the design method for three particular applications. These activities are actually on going and are planned to continue in the next years.

Planar antenna for near-field applications

The design techniques used for focusing and shaping the electromagnetic field in the near-field or Fresnel zone of an antenna stem from the seminal works in [4.53]–[4.55]. In these works, large (in terms of wavelength) and linearly-polarized apertures are considered and an equivalence between their near and far fields is derived. The considered near fields are either transversal or longitudinal to the axis of a defined focal plane parallel to the focusing aperture. In brief, it is shown that the fields in the Fresnel and far-field zones present the same properties if a quadratic phase taper is imposed to the tangential field distribution of the focusing aperture. Therefore, the optimization/shaping of the fields in the Fresnel zone is generally done by using classical far-field techniques. This is strictly valid as long as the focal plane is placed at distance larger than one aperture size and generally beyond the near-field or reactive zone of an antenna. In addition, there is no control or design flexibility on the aperture and spillover efficiency, polarization and size of the system. Besides, complicated and lossy beam forming networks are used to practically implement the required aperture field distribution introducing inevitable distortions [4.56]–[4.58].
A simple planar structure for the near-field can be obtained using the proposed method. An example of Bessel beam antenna has been successfully optimized and implemented using a RLSA antenna [P.16] as shown in Fig. 4.28(a). Measurements agree very well with the developed numerical model (Figs. 4.28(b)-(d)).

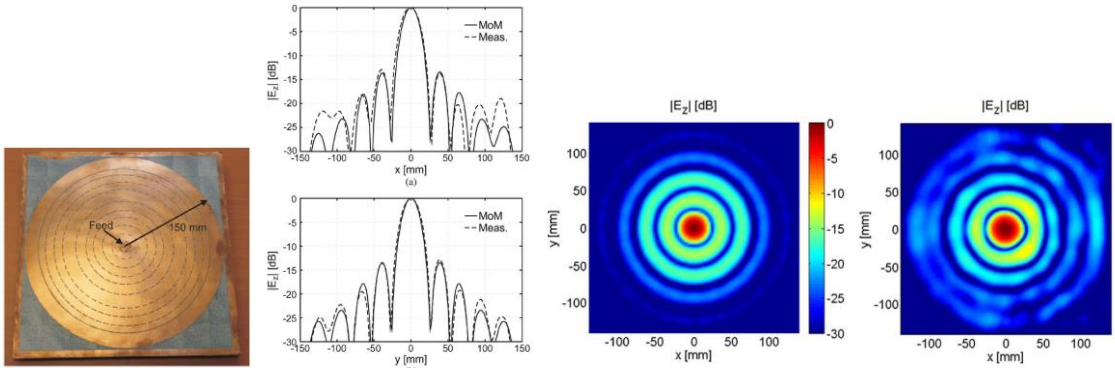

(a) (b) (c) (d)

Figure 4.28. (a) Final prototype. Comparison between measured and MoM results : (b) Normalized component of the electric field at on the focusing (c) 2-D MoM electric field plot. (d) 2-D measured electric field plot.

Two similar antennas have been implemented also with metasurface technology. Fig. 4.29 presents the antenna impedance distributions, while Fig. 4.30 represents the map of the near field generated by the metasurface antennas. As can be seen, the focusing effect is present within the non-diffractive region (white line).

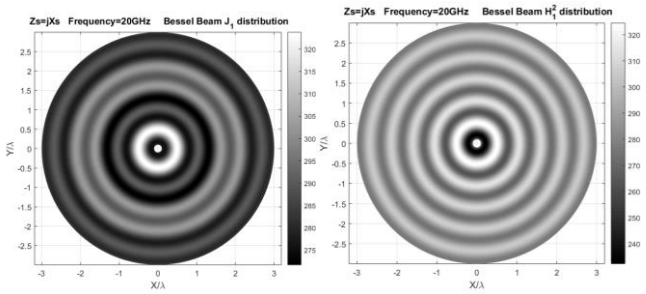

Figure 4.29. Reactance chart for a Bessel beam polarized along *z*, generated with a J_1 distribution or an $H_1^{(1)}$ distribution. The average impedance is Z_s=j 290Ω and modulation index M=0.17.

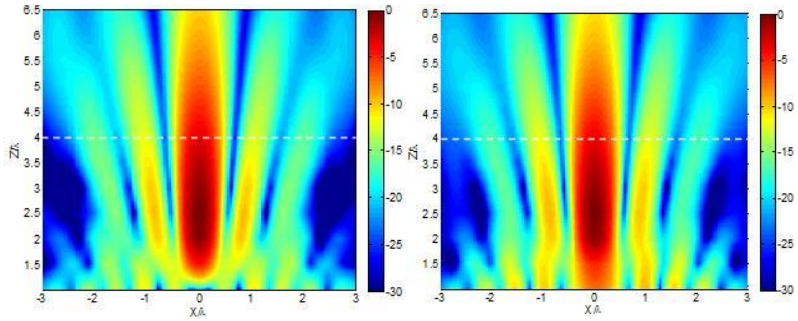

Figure 4.30 Normalized near field E_z component radiated by scanning for a the Bessel beam launcher antenna (a) using the aperture distribution (21). (b) Alternative aperture distribution (24). The white line indicate the limit of non-diffractive range

As third example, an antenna optimized for the near-field focalization in a 3D region working at 30GHz is presented. The antenna layout is presented in Fig.4.31(a). Figs. 4.31(b)-(c), 4.32 present the measured near field and the field obtained with the developed MoM tool. An excellent agreement has been achieved.

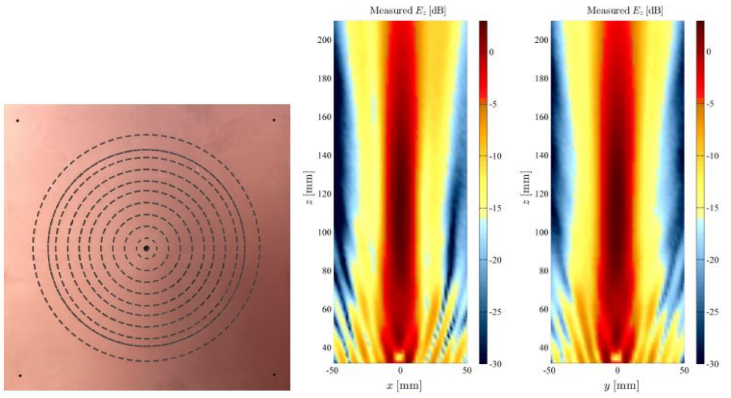

(a) (b) (c)

Figure 4.31. (a) Antenna layout. Measured E_z (normalized) at 30 GHz, on the (b) y = 0 and (c) x = 0 plane

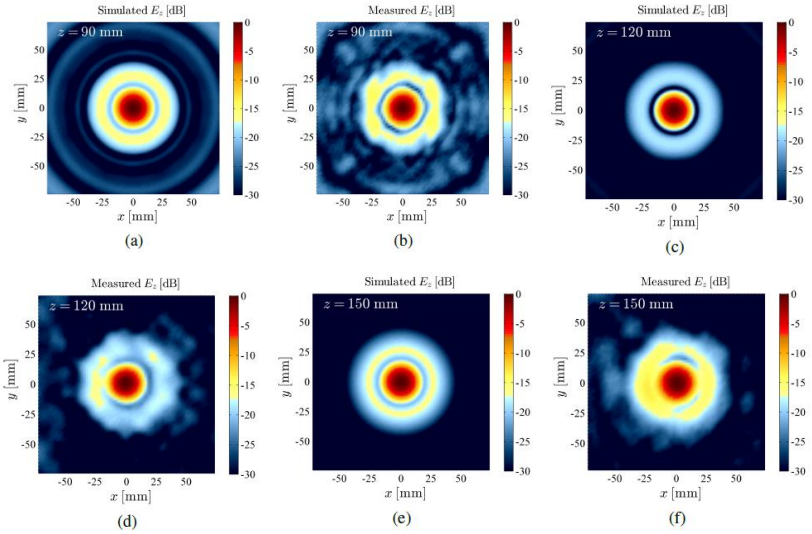

(a) (b) (c) (d) (e) (f)

Figure 4.32. 2D illustrations of the normalized Ez at three different heights (90,120 and 150 mm). Simulations and measurements are presented.

This approach has been also used to investigate the possibility of excitation of Orbital Angular Momentum (OAM) field in the near field. Various antenna solutions have been proposed to radiate far fields carrying OAM. On the other hand, fewer results are known about the focusing capabilities of vortex beams in the near field. A RLSA antenna has been optimized and the preliminary results shown in Fig. 4.33 are very promising.

These works are done together with Dr. Mauro Ettorre, CNRS researcher at IETR, and with Pr. Matteo Albani from the University of Siena (Italy). At this moment a postdoc and a PhD student are working on this subject while in the last two years two PhD have actively contributed to the topic.

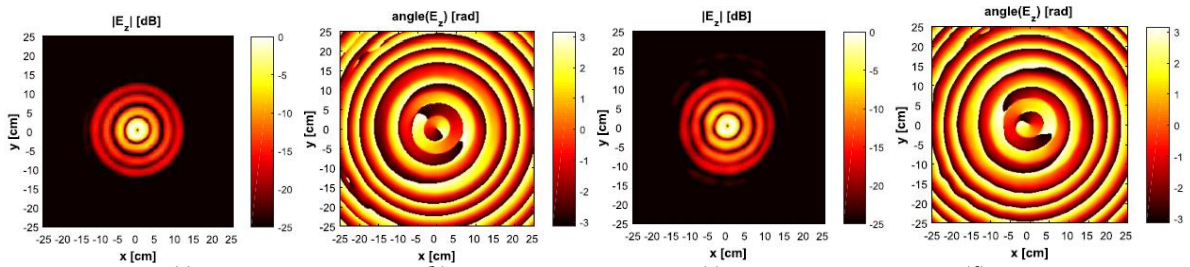

(a) (b) (c) (d)

Figure 4.33. Normalized *Ez* component for *f* = 12.5 GHz by the in-house MoM and CST for z = 32 cm. (a) Amplitude. (b) Phase. Normalized Ez component for f = 12.5 GHz by CST (z = 32 cm, as in Fig. 9). (a) MoM Amplitude. (b) MoM Phase. (c) CST Amplitude. (d) MoM Phase

Planar metasurface antenna design for far field applications

Some preliminary designs have been performed in order to test the aperture field implementation procedure using metasurfaces. Two realizations working at 9.5GHz are shown in Fig. 4.34. The first prototype is a broadside RHCP antenna while the second is a four beams antenna radiating two orthogonal LP beams, and R and L-HCP beams. The measurements are presented in Figs. 4.35-4.36. The desired radiating pattern has been successfully implemented. This work, done in collaboration with Pr. Hélène Roussel from L2E, has been funded by the CNES (PhD thesis +R&T project).

Figure 4.34. Representation of the two manufactured metasurfaces. (a) Broadside RHCP metasurface. (b) Four-beams metasurface.

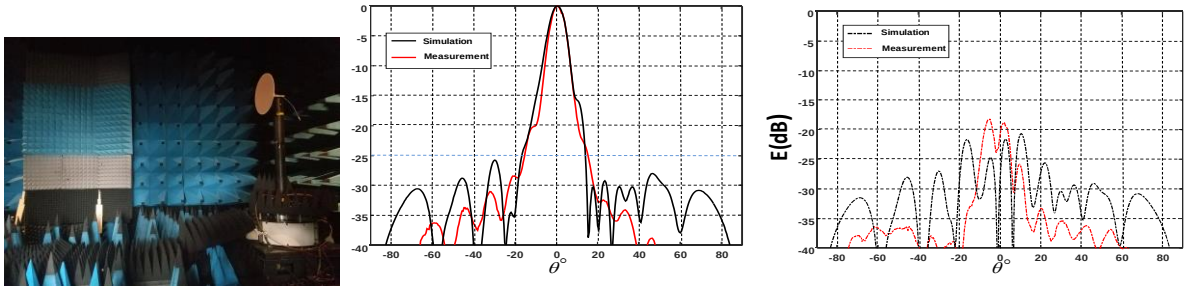

Figure 4.35. Measurement setup of the far field radiation pattern at the GeePs Laboratory. Broadside RHCP metasurface radiation pattern (normalized) at 9.5 GHz. Simulation results are represented in black while measurements are in red (a) RHCP component in the cut-plane. (b) LHCP component in the cut-plane.

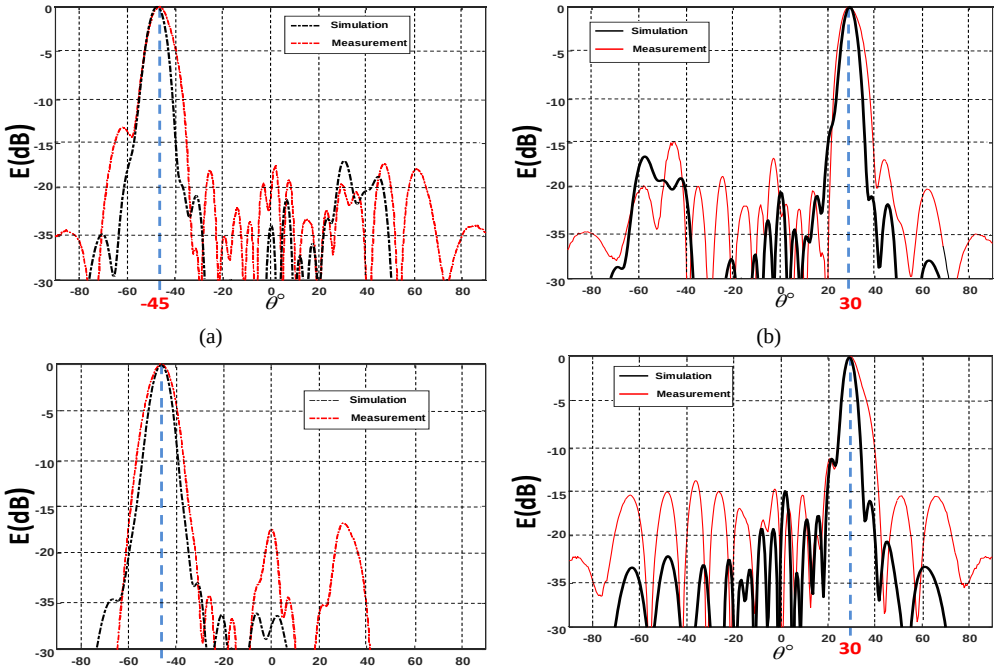

Figure 4.36. Multi-beam metasurface radiation pattern (normalized) at 9.5 GHz. Simulation results are represented in black while measurements are in red (a) RHCP component in the $\phi = 90°$ cut-plane. (b) LHCP component in the $\phi = 90°$ cut-plane. (c) Phi component in the $\phi = 0°$ cut-plane. (d) Theta component in the $\phi = 0°$ cut-plane

THz application

An interesting application of these structures is the design of beam splitters for multi-pixel THz heterodyne receptor for radio astronomy applications. A classical receptor scheme is shown in Fig. 4.36(a). In order to obtain a multipixel receptor the Radio Frequency (RF) signal and the Local Oscillator (LO) have to be splitted in multiple beams of equal power Fig. 4.36(b).

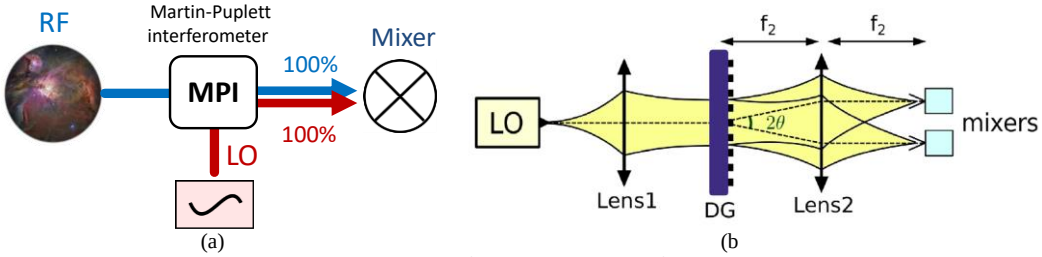

Figure 4.36: Schematic of a. (b) Optical setup of a phase grating

For beam splitter design, Daman or Fourier gratings are commonly used. It is a periodic lattice that can reflect an incident plane-wave into several beams. While the direction of the beams can be chosen, their shape cannot. Also, the shape of the incident beam is not taken into account and this lead to sub-optimal efficiency. To add more degrees of freedom in the design and to efficiently take into account the oblique incident non-planar wave-front, different optimization methods to design phase-only Diffractive Optical Elements (DOEs) exists in the literature where an Inverse Fourier Transform (IFT) maps the desired radiated field pattern onto the DOE aperture. In the process, GO approximation is classically assumed at optical frequencies but can lead to non-optimized performance at THz.

Our procedure does not make use of GO approximation (for the aperture field calculation) but calculates instead the radiated field due to an equivalent magnetic current in the DOE aperture in the optimization process. With respect to GO-assumptions-based design procedure, this rigorous approach enables obtaining equal-intensity split beams, required in multi-pixel instruments.

The difference can be explained by the dipolar nature of the reflector's current radiation that is not taken into account in GO, which leads to unbalanced beams under oblique incidence illumination (the intensity of the field radiated by a current element is not isotropic over the beam angles as supposed by GO).

This work is done together with Dr. Julien Sarrizin (L2E), and is a collaboration with Dr. Martina Wiedner from the Observatoire de Paris (LERMA), who designs and builds heterodyne receivers for THz radio-astronomy.

Two PhD students have worked on this topic. The funding comes from the CNES (French Space Agency) and the projects are led by Dr. Martina Wiedner.
Two prototypes at 610 GHz have been fabricated (see figs 4.37(a) and 4.38(a)) and characterized (see figs 4.37(b) (c) and 4.38(b) (c)).

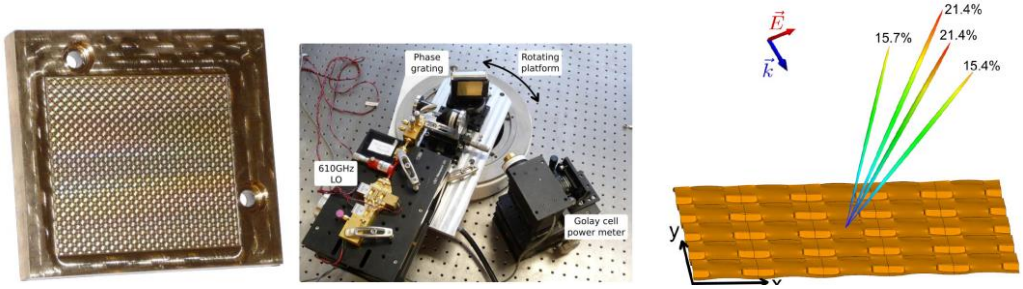

(a) (b) (c)

Figure 4.37: (a)Manufactured reflective phase grating (b) Measurements setup (c) Measured far-field pattern

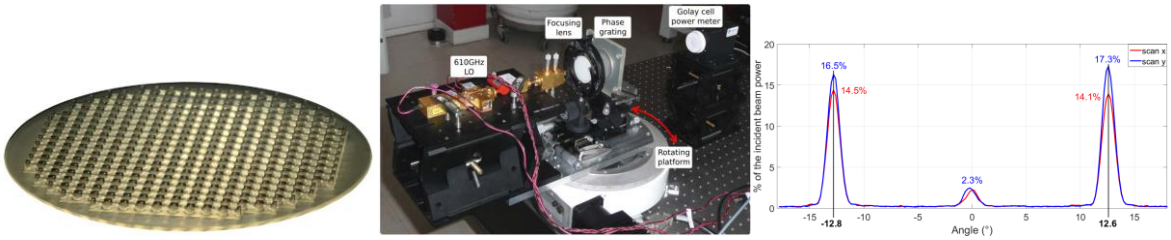

(a) (b) (c)

Figure 4.38. (a) Transmissive phase grating made of TPX®. (b) Measurements set-up (b) Measured power

Future work

A planar antenna for SATCOMM applications will be developed in the ANR-ASTRID Fast-HEM-3DSIW framework in collaboration with the IETR. The current state of the art for communication/surveillance systems shows a need for complex radiating frontends. Such systems should be able to handle multiple beams in order to cover large areas with a high antenna gain. 3D integrated multi-beam antennas can represent a breakthrough for military and civil applications for the integration of such systems in moving platforms. At the moment, the most promising solutions are based on quasi-optical Beam Forming Network (BFN) realized using multilayer Substrate Integrated Waveguide (SIW) technology. The optimization algorithms will be used for the design and realization of a novel complex multilayer quasi-optical Beam Forming Network (up to 6 metallic layers) for SATCOMM antenna frontends working at Ka band.

4.1.3 Equipment

My research mainly lies in modelling and numerical fields, however as shown in the previous section, the test and the application of the procedure needs the realization and the measurements of several antennas prototypes. This activity requires a certain number of rather expensive equipment.

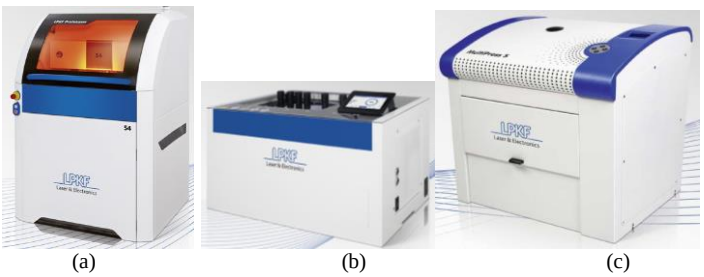

(a) (b) (c)

Figure 4.39: (a) Laser etching machine ProtoLaser S4 (b) Through-hole plating machine LPKF Contac S4 (c) LPKF MultiPress S

The realization of SIW and metasurface antennas will be performed internally at L2E. In fact, a laser etching machine is available from beginning 2018, while a through-hole plating machine and a multipress for creating multilayer circuit have just been acquired and they will be available in the next months (Fig. 4.39).
Regarding the measurement environment, we now have, since 2017, two anechoic chambers. A large one, built by Siepel company in our campus in Saint-Cyr (outside Paris), and a smaller one in the L2E laboratory (Fig. 4.40). Moreover, a collaboration with Dr. Mohammed Serhir (GeePs), expert of measurements, has started recently.
For the structured surface antennas, realization and the measurements will be performed by our colleagues at LERMA.

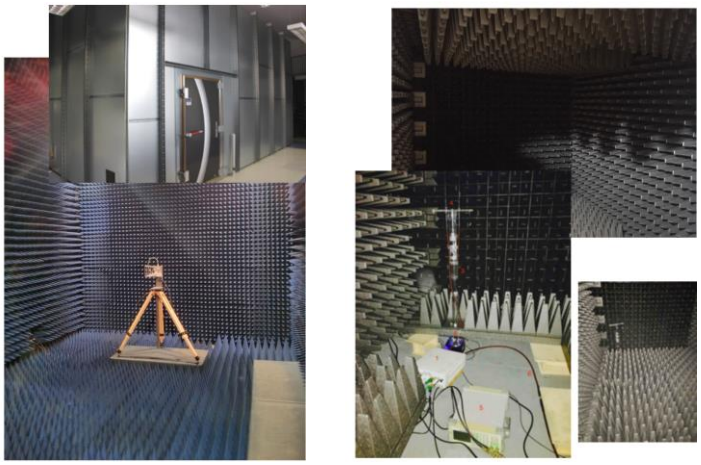

(a) (b)

Figure 4.40: Experimental environment at L2E. (a) Anechoic chamber (Siepel) at Saint Cyr, size: 10m x 4.4m x 4.4m, frequency: 400MHz+ (b) Anechoic chamber at L2E, size: 3m x 3 mx 2m.

REFERENCES

[4.1] R. Piestun and J. Shamir, "Synthesis of three-dimensional light fields and applications," Proc. IEEE, vol. 90, no. 2, pp. 222–244, Feb. 2002.
[4.2] R. Piestun and J. Shamir, "Synthesis of three-dimensional light fields and applications," Proc. IEEE, vol. 90, no. 2, pp. 222–244, Feb. 2002.
[4.3] J. J. Stamnes, Waves in Focal Regions: Propagation, Diffraction and Focusing of Light, Sound and Water Waves. CRC Press, Jan.1986.
[4.4] S. J. Orfanidis. (2013). Electromagnetic Waves and Antennas [Online]. Available: http://eceweb1.rutgers.edu/~orfanidi/ewa/
[4.5] F. J. Goebels and K. C. Kelly, "Arbitrary polarization from annular slot planar antennas," *IRE Trans. Antennas Propagat.*, vol. AP-9, no. 4, pp. 342-349, July 1961
[4.6] N. Goto and M. Yamamoto, "Circularly polarized radial-line slot antennas," IECE Japan, Tech. Rep., APSO-57, Aug. 1980.
[4.7] M. Albani, A. Mazzinghi, and A. Freni, "Automatic design of CP-RLSA antennas," *IEEE Trans. Antennas Propag.*, vol. 60, no. 12, pp. 5538–5547, Dec. 2012.
[4.8] S. Park, Y. Okajima, J. Hirokawa, and M. Ando, "A slotted post-wall waveguide array with interdigital structure for 45 linear and dual polarization," *IEEE Trans. Antennas Propag.*, vol. 53, no. 9, pp. 2865–2871, Sep. 2005.
[4.9] M. Ettorre, R. Sauleau, and L. Le Coq, "Multi-beam multi-layer leaky wave SIW pillbox antenna for millimeter-wave applications," *IEEE Trans. Antennas Propag.*, vol. 59, no. 4, pp. 1093–1100, Apr. 2011.
[4.10] M. Ettorre, A. Neto, G. Gerini, and S. Maci, "Leaky-wave slot array antenna fed by a dual reflector system," *IEEE Trans. Antennas Propag.*, vol. 56, no. 10, pp. 3143–3149, Oct. 2008.
[4.11] I. Boudreau, K.Wu, and D. Deslandes, "Broadband phase shifter using air holes in substrate integrated waveguide," in *Proc. IEEE MTT-S Int.Microw. Symp.*, Baltimore, MD, USA, Jun. 2011, pp. 1–4.
[4.12] P. Chen,Z.Kuai, J. Xu,H.Wang, J. Chen,H.Tang, J. Zhou, andK.Wu, "A multibeam antenna based on substrate integrated waveguide technology for MIMO wireless communications," *IEEE Trans. Antennas Propag.*, vol. 57, no. 6, pp. 1813–1821, Jun. 2009.
[4.13] M. Kishihara, K. Yamane, and I. Ohta, "Analysis of post-wall waveguide by H-plane planar circuit approach," in *Proc. IEEE MTT-S Int. Microw. Symp.*, Honolulu, HI, USA, 2007, pp. 1931–1934
[4.14] K. Tekkouk, M. Ettorre, R. Sauleau, and M. Casaletti, "Folded Rotman lens multibeam antenna in SIW technology at 24 GHz," in *Proc. EuCAP*, Prague, Czech Republic, Mar. 26–30, 2012, pp. 2308–2310.
[4.15] G. Valerio, D. R.Wilton, D. R. Jackson, and A. Galli, "Acceleration of periodic mixed potentials for layered media with 2-D inclusions based on a modified Ewald method," *IEEE Trans. Antennas Propag.*, vol. 60, no. 8, pp. 3782–3793, Aug. 2012.
[4.16] B. Tomasic and A. Hessel, "Linear array of coaxially fed monopole elements in a parallel plate waveguide—Part I: Theory," *IEEE Trans. Antennas Propag.*, vol. 36, no. 4, pp. 449–462, Apr. 1988.
[4.17] M. Casaletti, R. Sauleau, M. Ettorre, and S. Maci, "Efficient analysis of metallic and dielectric posts in parallel-plate waveguide structures," *IEEE Trans. Microw. Theory Tech.*, vol. 60, no. 10, pp. 2979–2989, Oct. 2012.
[4.18] R. E. Matick, Transmission Lines for Digital and Communication Networks. New York: *McGraw-Hill*, 1969.
[4.19] S. P. Morgan, Jr., "Effects of surface roughness on eddy current losses at microwave frequencies," *J. Appl. Phys.*, vol. 20, pp. 352–362, 1949.

[4.20] L. Tsang, X. Gu, and H. Braunisch, “Effects of random rough surface on absorption by conductors at microwave frequencies,” *IEEE Microw. and Wireless Comp. Letters*, vol. 16, no. 4, pp. 221 – 223, Apr. 2006.
[4.21] R. Sorrentino, “Transverse resonance technique,” in *Numerical Techniques for Microwave and Millimeter-Wave Passive Structures*. T. Itoh, Eds. New York: Wiley, 1989.
[4.22] G.W. Hanson, A.B. Yakovlev, Operator Theory for Electromagnetics: An Introduction. *Springer*, 2002.
[4.23] M. Albani, A. Mazzinghi, and A. Freni, “Automatic design of CP-RLSA antennas,” *IEEE Trans. Antennas Propag.*, vol. 60, no. 12, pp. 5538 – 5547, Dec. 2012.
[4.24] L. B. Felsen and N. Marcuvitz, Radiation and Scattering of Waves. *IEEE Press*, 1994.
[4.25] M. Albani, A. Mazzinghi, and A. Freni, “Rigorous MoM analysis of finite conductivity effects in RLSA antennas,” *IEEE Trans. Antennas Propag*, vol. 59, no. 11, pp. 4023 – 4032, Nov. 2011.
[4.26] R. F. Harrington, *Field Computation by Moments Method*. NewYork, NY, USA: IEEE Press, 1992.
[4.27] S. H. Han, X. L. Wang, Y. Fan, Z. Q. Yang, and Z. N. He, “The generalized Chebyshev substrate integrated waveguide diplexer,” *Progress In Electromagnetics Research*, PIER 73, pp. 29–38, 2007.
[4.28] C. Pfeiffer and A. Grbic, “Bianisotropic Metasurfaces for Optimal Polarization Control: Analysis and Synthesis,” *Phys. Rev. Appl.*, vol. 2, no. 4, p. 44011, Oct. 2014.
[4.29] B. Fong, J. Colburn, J. Ottusch, J. Visher and D. Sievenpiper, "Scalar and Tensor Holographic Artificial Impedance Surfaces", *IEEE Trans. Antennas Propagat.*, vol. 58, no. 10, pp. 3212-3221, 2010.
[4.30] A. M. Patel and A. Grbic, “A printed leaky-wave antenna based on a sinusoidally-modulated reactance surface,” *IEEE Trans. Antennas Propag.*, vol. 59, no. 6, pp. 2087–2096, Jun. 2011.
[4.31] D. J. Gregoire, “Impedance modulation patterns for artificial impedance-surface-antennas,” *IEEE Antennas and Propagation Society International Symposium*, Orlando, FL, July 7-13, 201.
[4.32] C. Pfeiffer and A. Grbic, "A Printed, Broadband Luneburg Lens Antenna", *IEEE Trans. Antennas Propagat*., vol. 58, no. 9, pp. 3055-3059, 2010.
[4.33] Ming Huang, Shiwen Yang, Fei Gao, R. Quarfoth and D. Sievenpiper, "A 2-D Multibeam Half Maxwell Fish-Eye Lens Antenna Using High Impedance Surfaces", *Antennas Wirel. Propag. Lett*., vol. 13, pp. 365-368, 2014.
[4.34] T. Dong, X. Ma, and R. Mittra, “Modeling large nonuniform optical antenna arrays for metasurface application,” *Journal of Applied Physics*, vol. 114, no. 4, pp. 043103–043103-10, Jul. 2013.
[4.35] E. Martini and S. Maci, “Metasurface transformation theory,” in Transformation Electromagnetics and Metamaterials: Fundamental Principles and Applications, D. H. Werner and D.-H. Kwon, Eds. Berlin: Springer, 2013.
[4.36] X. Wan, W. Xiang Jiang, H. Feng Ma, and T. Jun Cui, “A broadband transformation-optics metasurface lens,” *Applied Physics Letters*, vol. 104, no. 15, pp. 151601–151601-4, 2014.
[4.37] K. Hannam, D. A. Powell, I. V. Shadrivov, and Y. S. Kivshar, “Broadband chiral metamaterials with large optical activity,” *Phys. Rev. B*, vol. 89, pp. 125105, Mar. 2014.
[4.38] C. Pfeiffer and A. Grbic, “Controlling vector Bessel beams with metasurfaces,” Phys.Rev.Appl., vol. 2, no. 4, p. 044012, 2014
[4.39] A. Oliner and A. Hessel, "Guided waves on sinusoidally-modulated reactance surfaces", *IRE Trans. Antennas Propag*., vol. 7, no. 5, pp. 201-208, 1959.
[4.40] L. Matekovits, "Analytically Expressed Dispersion Diagram of Unit Cells for a Novel Type of Holographic Surface", *IEEE Antennas and Wireless Propagation Letters*, vol. 9, pp. 1251-1254, 2010.
[4.42] S. Podilchak, L. Matekovits, A. Freundorfer, Y. Antar and M. Orefice, "Controlled Leaky-Wave Radiation From a Planar Configuration of Width-Modulated Microstrip Lines", *IEEE Trans. Antennas Propagat*, vol. 61, no. 10, pp. 4957-4972, 2013.
[4.42] C. L. Holloway, E. F. Kuester, J. Gordon, J. O. Hara, J. Booth, & D. R. Smith, “An overview of the theory and applications of metasurfaces: The two-dimensional equivalents of metamaterials,” *IEEE Trans. Antennas Propag*., vol. 54, no. 2, pp. 10–35, Apr. 2012.
[4.43] S. Pandi, C. Balanis and C. Birtcher, "Design of Scalar Impedance Holographic Metasurfaces for Antenna Beam Formation With Desired Polarization", *IEEE Trans. Antennas Propagat*., vol. 63, no. 7, pp. 3016-3024, 2015.
[4.44] G. Minatti, M. Faenzi, E. Martini, F. Caminita, P. De Vita, D. Gonzalez-Ovejero, M. Sabbadini and S. Maci, "Modulated Metasurface Antennas for Space: Synthesis, Analysis and Realizations", *IEEE Trans. Antennas Propagat*., vol. 63, no. 4, pp. 1288-1300, 2015.
[4.45] G. Minatti, S. Maci, P. De Vita, A. Freni and M. Sabbadini, "A Circularly-Polarized Isoflux Antenna Based on Anisotropic Metasurface", *IEEE Trans. Antennas Propagat*., vol. 60, no. 11, pp. 4998-5009, 2012.
[4.46] A. Patel and A. Grbic, "Effective Surface Impedance of a Printed-Circuit Tensor Impedance Surface (PCTIS)", *IEEE Transactions on Microwave Theory and Techniques*, vol. 61, no. 4, pp. 1403-1413, 2013
[4.47] D. Hoppe and Y. Rahmat-Samii, Impedance boundary conditions in electromagnetics. Washington, DC: Taylor & Francis, 1995.
[4.48] E. Martini, M. Mencagli, D. Gonzalez-Ovejero and S. Maci, "Flat Optics for Surface Waves", *IEEE Trans. Antennas Propagat*., vol. 64, no. 1, pp. 155-166, 2016.
[4.49] E. Martini, M. Mencagli, Jr., and S. Maci, “Metasurface transformation for surface wave control,” *Philos. Trans. R. Soc.* A, vol. 373, no. 2049, p. 20140355, 2015.
[4.50] Y.B. Li, X. Wan, B.G. Cai, Q. Cheng, T.J. Cui, “Frequency-controls of electromagnetic multibeam scanning by metasurfaces”, *Scientific Reports*, Vol 4: 6921, 5 November 2014.
[4.51] S. J. Orfanidis. (2013). Electromagnetic Waves and Antennas [Online]. Available: http://eceweb1.rutgers.edu/~orfanidi/ewa/
[4.52] H. Bilow, "Guided waves on a planar tensor impedance surface", *IEEE Trans. Antennas Propagat*, vol. 51, no. 10, pp. 2788-2792, 2003.
[4.53] J. W. Sherman, “Properties of focused apertures in the Fresnel region,” *IRE Trans. Antennas Propag.*, vol. AP-10, no. 4, pp. 399–408, Jul. 1962.
[4.54] W. J. Graham, “Analysis and synthesis of axial field pattern of focused apertures,” *IEEE Trans. Antennas Propag.*, vol. AP-31, no. 4, pp. 665–668, Jul. 1983.
[4.55] R. C. Hansen, “Focal region characteristics of focused array antennas,” *IEEE Trans. Antennas Propag.*, vol. AP-33, no. 12, pp. 1328–1337, Dec. 1985.
[4.56] A. Buffi, P. Nepa, and G. Manara, “Design criteria for near-field-focused planar arrays,” *IEEE Trans. Antennas Propag.*, vol. 14, no. 1, pp. 40–50, Feb. 2012.
[4.57] K. D. Stephan, J. B. Mead, D. M. Pozar, L. Wang, and J. A. Pearce, “A near field focused microstrip array for a radiometric temperature sensor,” *IEEE Trans. Antennas Propag.*, vol. 55, no. 4, pp. 1199–1203, Apr. 2007.
[4.58] M. Bogosanovic and A. G.Williamson, “Microstrip antenna array with a beam focused in the near-field zone for application in noncontact microwave industrial inspection,” *IEEE Trans. Instrum.Meas.*, vol. 56, no. 6, pp. 2186–2195, Dec. 2007.

4.2 Electromagnetic analysis of large natural environments for radar applications

***List of related publications*: [P.3], [IC.1], [C.5], [C.11].**

The main objective of this activity is to develop an efficient and accurate full-wave method for the electromagnetic analysis of large portion of natural environments in presence of targets for the Foliage Penetrating (FoPen) radars.
This work is done together with Pr. Helene Roussel, Full Professor at L2E. The funding comes from the DGA (ANR ASTRID led by Pr. Roussel) and a ANR ASTRID Maturation will be submitted next year.

Context

Since low frequency electromagnetic waves penetrate through forest foliage, the frequency bands VHF, UHF, L and S are typically used for this type of applications [4.59]-[4.64]. FoPen radar development is very expensive and requires extensive measurement programs. The development of a "full wave" electromagnetic model for analyzing scattering from large forest areas surrounding metallic targets can significantly reduce the number of such measurements. Indeed, the use of such models could substitute the first steps of radar developement by identifiying the types of radar configurations which should be investigated.
In addition to detecting targets under cover, the proposed model can also treat problems related to the forest, such as the study of the biomass and the influence of moisture on the diffracted field.

Motivation

The development of exact electromagnetic models of forest scenarios presents two main challenges: (i) First, the scene is composed of highly heterogeneous media (lossy dielectric materials and metals); (ii) The size of the illuminated area (the focal spot of the UHF radar antenna) could be up to 50×50 m^2 which corresponds to 65×65 wavelentgh at 400MHz.
Several techniques have been proposed in the literature for electromagnetic simulation of this type of scenarios. In [4.62], a hybrid FDTD formulation using Huygens' surface approach for the metallic target and a coherent single scattering theory for the forest has been proposed. This model accounts for the coupling between the target and the foliage by using the reciprocity theorem [4.63]. In [4.64], a Multilevel Fast Multipole Algorithm (MLFMA) has been used to evaluate the scattering characteristics of electrically large conducting and dielectric targets placed at the interface of a dielectric half-space below and air above.
Several full-wave techniques can be used to evaluate the field scattered by a heterogeneous environment (dielectric and metallic media). A surface integral formulation has been employed in [4.65] for both metallic and dielectric scatterers. However, this method requires the decomposition of the scene into several homogeneous dielectric sub problems, which is not possible for a natural environment.
The main idea is to develop a model that can take advantage of all the possible physical simplifications that can be safely applied for our application and, at the same time, that can be easily and deeply parallelized.

On going research

A typical scene of interest for our investigation is described in Fig.4.42a. A metallic object is placed in a locally flat natural environment and surrounded by trees. From an electromagnetic point of view, the scene is composed of two classes of elements: the dielectric forest and the metallic target.

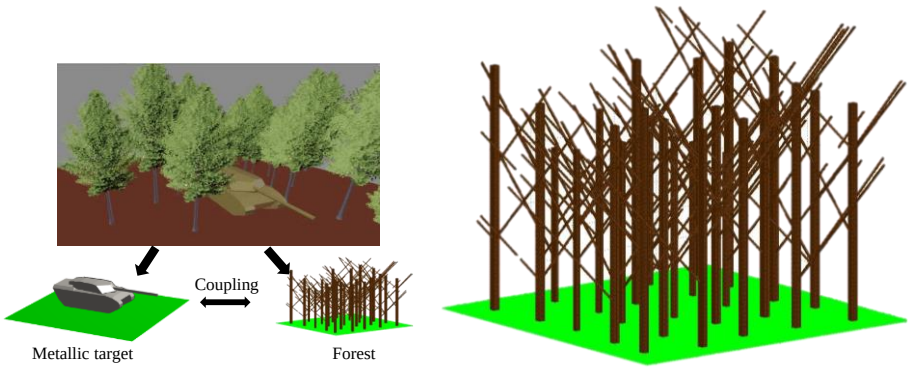

Figure 4.42. (a) Example of representation of a typical scene (b) The trees are described by vertical cylinders (trunks) and tilted cylinders (primary branches) at VHF frequencies (around 400 MHz).

In the frequency range between 100 to 400 MHz (UHF-VHF) the main scatterers of the natural environment are the tree trunks and the primary branches [4.74]. As a result, the forest can be represented by vertical and titled dielectric cylinders as shown in Fig.4.42b.

Our approach is based on a hybrid surface/volume integral formulation which uses the Characteristic Basis Function Method (CBFM) applied in the context of the VEFIE [4.67]-[4.69] to construct a numerical Green's function of the natural environment. This choice is justified by the fact that the volume formulation of the electric field integral equation has been successfully used by our group to model the "forest only" scene.

The scattered electromagnetic field is obtained by solving an Electric Field Integral Equation (EFIE) for the metallic objects using a Method of the Moment (MoM) scheme [4.70]-[4.73]. The target is supposed to be a Perfect Electric Conductor (PEC), while the ground is assumed to be flat. This latter limitation can be overcome by modeling the ground deformations as dielectric objects with the same electromagnetic characteristic as those of the ground.

Hybrid EFIE-VEFIE formulation

Throughout this chapter, the free-space propagation constant k_0 is defined as $k_0 = \omega\sqrt{\varepsilon_0\mu_0} = 2\pi/\lambda_0$ where μ_0, ε_0 and λ_0 are respectively the permeability, permittivity and the wavelength in free space. The observation and source point are represented respectively by $\mathbf{r}$ and $\mathbf{r'}$.

Let us consider a PEC object with boundary Γ with normal $\hat{\mathbf{n}}$ illuminated by by an incident electromagnetic wave $\mathbf{E}_i^S$. This wave will induce a surface electric current $\mathbf{J}_S(\mathbf{r}')$ radiating the scattered wave by the object. This latter can be expressed as the convolution of the unknown current $\mathbf{J}_S$ and the Green's function of the medium. Using the boundary condition on $\mathbf{r} \in \Gamma$ (total electrical tangent field equal to zero) leads to the EFIE:

$$\hat{\mathbf{n}}\times\hat{\mathbf{n}}\times\mathbf{E}_i^S(\mathbf{r}) + \hat{\mathbf{n}}\times\hat{\mathbf{n}}\times\left[jk_0\int_\Gamma G(\mathbf{r},\mathbf{r}')\mathbf{J}_S(\mathbf{r}')d\Gamma - \frac{1}{jk_0}\int_\Gamma \nabla'\cdot\mathbf{J}_S(\mathbf{r}')\nabla G(\mathbf{r},\mathbf{r}')d\Gamma \right] = 0 \tag{4.67}$$

The obtained equation is a Fredholm integral equation of the first kind and it can be used for closed and open structures.

Let us consider now a region Ω filled by an inhomogeneous dielectric with electric permittivity $\varepsilon(\mathbf{r})$ and electric conducibility $\sigma(\mathbf{r})$ illuminated by the incident field $\mathbf{E}_i^V$. Introducing an unknown equivalent volume current as $\mathbf{J}_V(\mathbf{r}) = j\omega k\Delta(\mathbf{r})\varepsilon_0\mathbf{E}$, where $\Delta(\mathbf{r}) = \left(\varepsilon(\mathbf{r}) - \varepsilon_0\right)/\varepsilon_0$ is the dielectric contrast, leads to the following equation (Volume Electric Field Integral Equation) that held for each $\mathbf{r} \in \Omega$:

$$\frac{\mathbf{J}_V(\mathbf{r})}{j\omega\Delta(\mathbf{r})\varepsilon(\mathbf{r})} + j\omega\mu_0\int_\Omega G(\mathbf{r},\mathbf{r}')\mathbf{J}_S(\mathbf{r}')d\Omega + \frac{j}{\omega\varepsilon_0}\nabla\int_\Omega G(\mathbf{r},\mathbf{r}')\nabla'\cdot\mathbf{J}_V(\mathbf{r}')d\Omega = \mathbf{E}_i^V \tag{4.68}$$

When both metallic and dielectric object are present, a hybrid volume surface integral equation can be derived by considering as incident field for the EFIE the sum of the primary field radiated by the source ($\mathbf{E}_i$) and the field radiated by volume currents (namely $\mathbf{E}_i^S(\mathbf{r}) = \mathbf{E}_i(\mathbf{r}) + \mathbf{E}(\mathbf{J}_V,\mathbf{r})$) and for the VEFIE the sum of field radiated by the source and the currents ($\mathbf{E}_i^V(\mathbf{r}) = \mathbf{E}_i(\mathbf{r}) + \mathbf{E}(\mathbf{J}_S,\mathbf{r})$).

For the numerical solution, a Moment Method discretization scheme is then introduced by approximating the surface and volume electric currents as

$$\begin{aligned} \mathbf{J}_S(\mathbf{r}') &= \sum_{n=1}^{N_S} I_n^S\mathbf{f}_n^S(\mathbf{r}') \\ \mathbf{J}_V(\mathbf{r}') &= \sum_{n=1}^{N_V} I_n^V\mathbf{f}_n^V(\mathbf{r}') \end{aligned} \tag{4.69}$$

where I_n^S, I_n^V are unknown coefficients and $\mathbf{f}_n^S, \mathbf{f}_n^V$ are suitable sets of basis surface and volume functions, respectively. Generally a Galerking testing scheme is adopted leading to the following matrix equation

$$\begin{bmatrix} \underline{\underline{\mathbf{Z}}}_{ss} & \underline{\underline{\mathbf{Z}}}_{sv} \\ \underline{\underline{\mathbf{Z}}}_{vs} & \underline{\underline{\mathbf{Z}}}_{vv} \end{bmatrix} \begin{bmatrix} \mathbf{I}_s \\ \mathbf{I}_v \end{bmatrix} = \begin{bmatrix} \mathbf{V}_s \\ \mathbf{V}_v \end{bmatrix} \tag{4.70}$$

where $\underline{\underline{\mathbf{Z}}}_{ss}$, $\underline{\underline{\mathbf{Z}}}_{vv}$ are the coupling matrices between basis functions of the same nature, $\underline{\underline{\mathbf{Z}}}_{vs}$, $\underline{\underline{\mathbf{Z}}}_{sv}$ represent the coupling matrices between different kind of currents, $\mathbf{I}_s$ and $\mathbf{I}_v$ are the unknown surface and volume current amplitudes, while $\mathbf{V}_s$ and $\mathbf{V}_v$ are the source vectors.

Application to the specific problem

In our application $G(\mathbf{r},\mathbf{r}')$ represent the Green's function of the two layered media (free-space and the lossy ground), Ω is the domain occupied by the dielectric scatterers (trunks and main branches), while Γ is the union of the PEC objects surfaces.

Since we are interested only in the diffracted field in the far-field region, a larger representation error in the surface and volume current can be tolered with respect to antenna applications where the currents and the near-field has to be computed accurately in order compute input parameters. This aspect let us introduce some approximations, based on physical arguments, that can significatively speed up the computational time while keeping a good accuracy in this contex (not in general).

The first approximation concerns the geometry and its discretization (meshing and basis function choice). The dielectric cylinders can be safely replaced by parallelepiped [4.66], this allow its discretization into N cubic cells of dimension smaller or equal to $\lambda_s/10$ (where λ_s is the wavelength inside the scatterers) so that the field inside each cell can be considered as constant. Hence, uniform basis functions and Dirac test functions (point matching method) can be used. However, the metallic surface Γ has to be discretized more accurately, thus a triangular mesh and Rao-Wilton-Glisson (RWG) basis functions [4.70] are used.

As second approximation, the Green's function is calculated by using a modified image dipole approach, which is based on an approximated continuous spectrum of plane waves. In the models presented heretofore, the metallic target and the trees are lying on a horizontal plane separating two semi-infinite homogeneous mediums (the ground and free space). The soil roughness is assumed to be negligible in the considered frequency band. The rigorous Green's function calculation of the vector and scalar potentials for a layered medium requires the evaluations of several Sommerfeld-type integrals [4.71]-[4.73]. To avoid doing these calculations, and thereby speeding up our computation significantly, a complex image approximation based on Fresnel reflection coefficients has been introduced (Fig. 4.43a). An image source is placed in the specular position with respect to the plane as for the PEC case, while its amplitude is modified by the Fresnel reflections coefficients given by $\Gamma_\perp = (k_{z0} - k_{z1})/(k_{z0} + k_{z1})$, $\Gamma_\parallel = (n_1 k_{z0} - k_{z1})/(n_1 k_{z0} + k_{z1})$, where $k_{zi} = \sqrt{k_i^2 - k_\rho^2}$ (with i=0,1) are the vertical wave numbers in free space and in the ground medium, k_ρ is the radial wave number, and n_1 is the refractive index of the lossy ground.

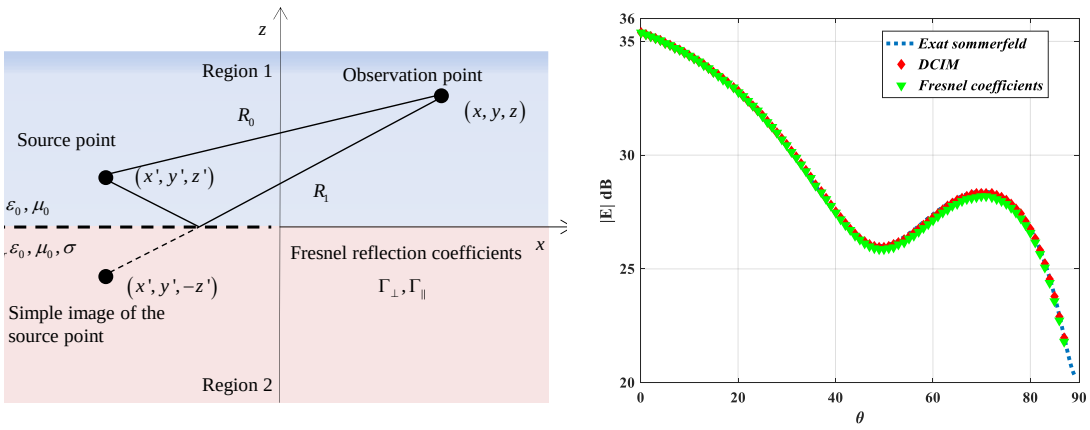

Figure 4.43. (a) Image principle geometry using Fresnel reflection coefficients. (b) Comparison of the amplitude of the total field diffracted by an oblique electric dipole moment oriented along ($\theta = 45°, \phi = 0°$) at $r = 5\text{m}$ plotted in the XZ plan ($\phi = 0°$).

The field $\mathbf{E}_i$ radiated by the image source is thus expressed as $\mathbf{E}_i(\mathbf{r}) = \Gamma_{\parallel}\mathbf{E}_p(\mathbf{r}) + (\Gamma_{\perp} - \Gamma_{\parallel})(\mathbf{E}_p(\mathbf{r}) \cdot \hat{\mathbf{u}})\hat{\mathbf{u}}$ where $\mathbf{E}_p$ is the field radiated by a source placed at the image position and $\mathbf{u} = (\mathbf{r} - \mathbf{r'}_{image}) / \|\mathbf{r} - \mathbf{r'}_{image}\| \times \hat{\mathbf{z}}$ and $\hat{\mathbf{u}} = \mathbf{u} / \|\mathbf{u}\|$.

The accuracy of the approximated approach based on the use of the Fresnel reflections coefficients has been widely investigated and the computational time compared with other methods. An example of an electric dipole placed in the free-space (region-1) above a lossy ground (region-2), as illustrated in Fig.4.43a. A lossy ground of relative permittivity $\varepsilon_r = 7$, and conductivity $\sigma = 0.02$ S/m is considered. The source point is located at $(x', y', z') = (0, 0, 0.1)$ m, and the working frequency is $f = 500$MHz. Figure 4.43b presents a comparison of the amplitude of the field obtained by using three different methods: - the rigorous Sommerfeld calculation (rigorous solution); - a two level discrete complex image method [4.74]-[4.76]; -the Fresnel coefficients method. The Fresnel coefficients method provides a sufficiently accurate result demanding a significantly lower execution time. Indeed, doing the simulation under the same computer the calculation of the Sommerfeld integral and the DCIM take respectively 59.25s and 16.77s while the approach proposed takes 2.83s. Such reduction in CPU time is of great interest when dealing with large scenes.

In the recent past years an efficient VEFIE solver has been developed [4.66] in our lab. It is based on an Extended-CBFM (CBFM-E) compression scheme [4.68] and can handle a large number of unknowns. This latter algorithm begins with a domain decomposition of the scene into several geometrical smaller blocks. In each block, Characteristic Basis Functions (CBFs) are generated by aggregating uniform (low-level) basis functions. The number of CBFs retained for each block is much lower than the original number of low-level basis functions, leading to a significant MoM interaction matrix compression. This scheme can easily handle problems involving millions of unknowns with a significant reduction of computational time and memory requirement with respect to conventional MoM approach.

In order to take advantage of the above-mentioned tool, we rewrite the linear system (4.70) by solving, separately, the two unknown currents terms ($\mathbf{I}_s$ and $\mathbf{I}_v$):

$$\left[\underline{\underline{\mathbf{Z}}}_{ss} - \underline{\underline{\mathbf{Z}}}_{c,s}\right]\mathbf{I}_s = \mathbf{V}_s - \underline{\underline{\mathbf{Z}}}_{sv}\underline{\underline{\mathbf{Z}}}_{vv}^{-1}\mathbf{V}_v \tag{4.71}$$

$$\left[\underline{\underline{\mathbf{Z}}}_{vv} - \underline{\underline{\mathbf{Z}}}_{c,v}\right]\mathbf{I}_v = \mathbf{V}_v - \underline{\underline{\mathbf{Z}}}_{vs}\underline{\underline{\mathbf{Z}}}_{ss}^{-1}\mathbf{V}_s \tag{4.72}$$

where $\underline{\underline{\mathbf{Z}}}_{c,s} = \underline{\underline{\mathbf{Z}}}_{sv}\underline{\underline{\mathbf{Z}}}_{vv}^{-1}\underline{\underline{\mathbf{Z}}}_{vs}$ and $\underline{\underline{\mathbf{Z}}}_{c,v} = \underline{\underline{\mathbf{Z}}}_{vs}\underline{\underline{\mathbf{Z}}}_{ss}^{-1}\underline{\underline{\mathbf{Z}}}_{sv}$ represent the coupling matrices.

Equation (4.71) can be interpreted as a EFIE scheme for the surface currents using the VEFIE formulation as numerical Green's function. System (4.72), represents a VEFIE scheme for the volume currents using the EFIE formumation as numerical Green's function.

Matrices representing volume current interactions are compressed by the CBFM_E approach enabling us to handle very large scenarios.

NUMERICAL AND EXPERIMENTAL VALIDATION

The model has been validated by comparisons with avaiable commercial software and by comparison with measurements.

Numerical validation

In order to obtain reference solutions small structures have been analyzed. An example is shown in Fig. 4.44a. The scenario is composed of a metallic parallelepiped surrounded by two identical trees. The size of the parallelepiped is (0.2 m × 0.2 m × 1.2m). The trees are composed of trunks of height 2.1m and 4 primary branches. The relative permittivity and conductivity of the trees are $\varepsilon_r = 4.2$ and $\sigma = 0.0167$S/m). The distance between the cube and the trees is $d = 0.25$m. The relative permittivity and conductivity of the ground are $\varepsilon_r = 5$ and $\sigma = 0.034$S/m, respectively. The incident field is a plane wave propagating along the direction defined by $(\theta_{inc}, \phi_{inc}) = (30°, 0°)$ at the frequency of $f = 300$MHz. The discretization of the scene leads to 7518 unknowns (7200 for the volume formulation and 318 for the surface one). In Fig.4.44b, a comparison of the amplitude of the diffracted Field (polar HH) obtained with DEMOS and FEKO is presented for an observation point at a distance $R = 2000$m. We note that good agreement is obtained between the two models.

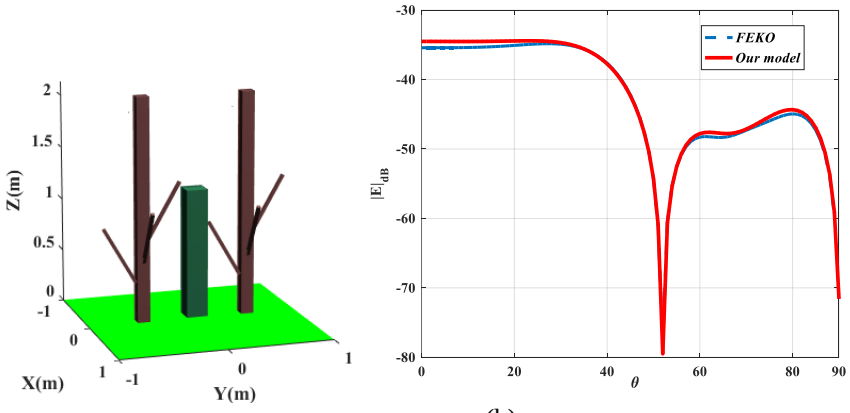

(b)

Figure 4.44. Comparison of the diffracted field. (a) the considered scene (b) the amplitude of the polar HH (dB) in the $\phi = 0°$ cut-plane.

In terms of the computing time, DEMOS is more efficient than FEKO, which uses the traditional MoM. In fact, it took 1minute and 15seconds to perform the analysis while FEKO needed around 35 minutes. The execution times were obtained on the same computer (CPU Intel® i7 4600U with 16 Gb RAM).

Experimental validation

Since environmental conditions and experimental uncertainties may dramatically influence the scattering as well as the forest electromagnetic properties change during the year, the underlying idea is to carry out bi-static scaled-model measurements in an anechoic chamber. Their aim is to validate our scattering model in well-controlled conditions. Some experiments have been conducted in the anechoic chamber of CCRM in Marseille, France (see Fig. 4.45a). The dimensions of the anechoic chamber are equal to 14 x 6.5 x 6.5 m3. The bi-static measurement setup consists of two antennas, a transmitter and a receiver, placed on a semi-circular vertical arch and/or a rotating arm (allowing the positioning of the antennas in the horizontal plane), a network analyzer, synthesizers and external mixers [4.76]. We plan to assess our model by comparing our results with measurements on controlled structures and for different frequencies and incident angles. Some preliminary measurements have already been performed, concerning a mono-static case and a simple configuration composed of a L-shaped target placed on a metal plate and surrounded by 2 trees (see Fig. 4.45a). On figure 4.45b, we compare for the VV and HH polarizations the variations of the measured and scattered fields with respect to the incident angle θ at 11Ghz. We obtain a good agreement between the two results.

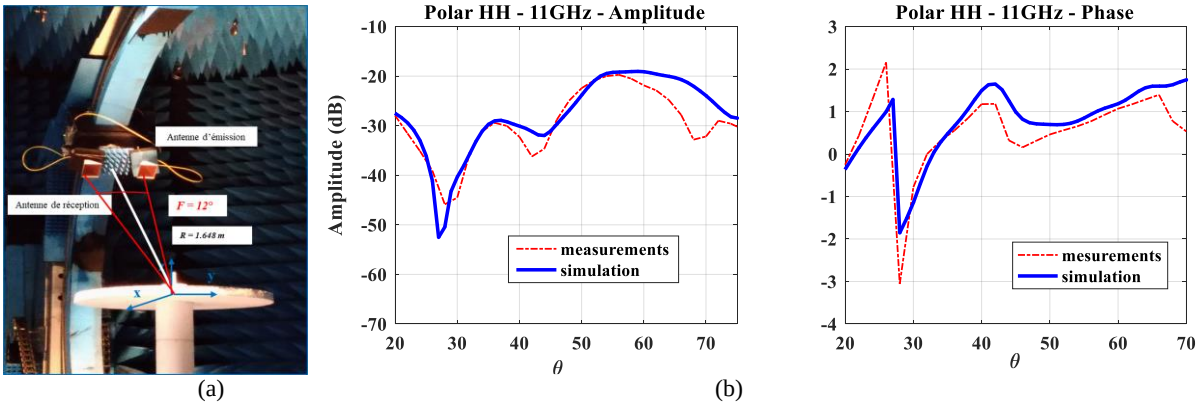

(a) (b)

Figure 4.45. a) The target b) Comparison of the scattered field (measured (red) and calculated (blue) scattered fields) by the L-shaped target placed on a metal plate.

APPLICATION OF THE MODEL TO REALISTIC CASES

The developed model can be used to investigate the effect of a metallic target in a realistic scenario. A large forest area generated arbitrary in a scene of $(15m \times 15m)$ (Fig. 4.56). The scene is comprised of 52 trees that corresponds to a tree density of ($0.23\,[trees/m^2]$) and a metallic military tank. Each tree has 8 primary branches and their heights vary between 1.2 m to 4.5 m. The relative permittivity and conductivity of the ground are $\varepsilon_r = 5$ and $\sigma = 0.07$S/m . The tank is 2.6m high, 3.2min length and 1.5m in width. The incident field is a plane wave of frequency $f = 400$MHz .

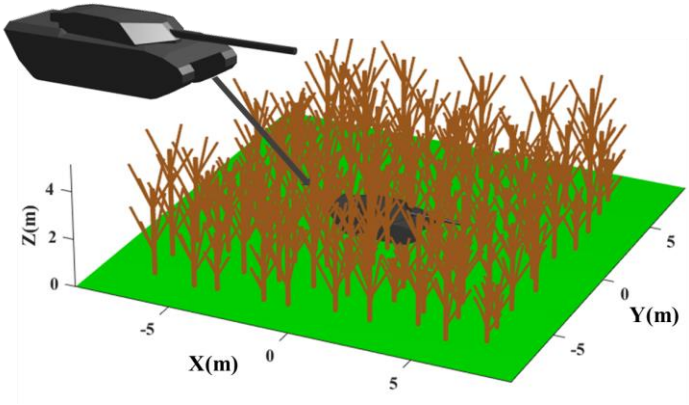

Figure 4.46. Geometry of the considered scene.

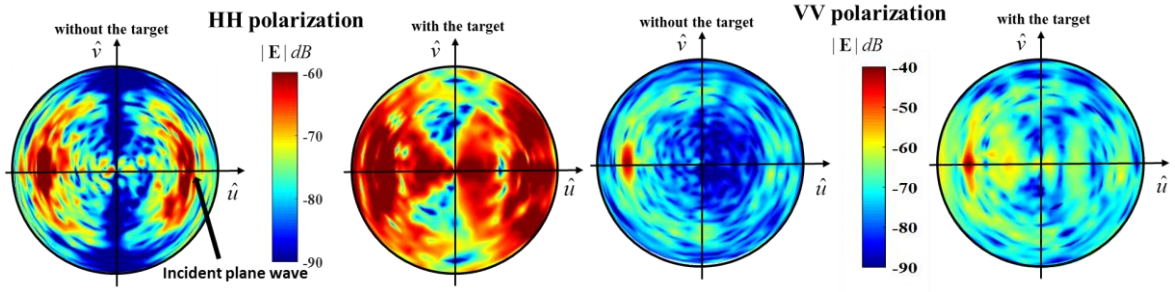

Figure 4.47. Influence of the presence of a metallic target in a forest environment on the amplitude of the co-polar *VV* and *HH* for the incident angle $(\theta_{inc},\phi_{inc}) = (45°,0°)$: (a) without the target (dB). (b) in presence of the target (dB).

Figure 4.47 presents the amplitude of the co-polarisations (*VV* and *HH)* of the scattered field calculated at a distance R=2000m with respect to the direction cosines ($\hat{u} = \sin\theta\cos\phi$ and $\hat{v} = \sin\theta\sin\phi$), both in presence and absence of the metallic target. This is done in order to investigate the effect of the presence of the target on the field diffracted by the forest. For this example, a bi-static configuration is used. The incident angles are $(\theta_{inc},\phi_{inc}) = (45°,0°)$ and the observation points are such that θ_s varies from 0° to 89° (with a step of 1°) and the azimuth angle ϕ_s varies from 0° to 360° (with a step of 5°).

Not unexpectedly, for the co-polarization cases of *VV* and *HH*, the maxima are in the forward ($\theta_{obs} = \theta_{inc}$ and $\phi_{obs} = \phi_{inc}$) and backward ($\theta_{obs} = \theta_{inc}$ and $\phi_{obs} = \phi_{inc} + 180°$) directions, when we consider only the forest, the latter being the strongest (the subscript *obs* refers to the angles of the observation points). This is due to the double bounce of signals between the trunk and the ground. Both of these lobes are relatively narrow. This is the typical bi-static scattering pattern of a single vertical cylinder laying on a flat surface, and by extension the one of a forest patch comprised of vertical trunks and branches with relatively vertical orientations.

In the other side concerning the cross-polar *HV* and *VH* given in Fig. 4.48, the maxima are not in the backward and forward directions. This may be due, at least partly, to the presence of primary branches of the trees. We can also imagine being able to better detect the target for these polarizations if we use bi-static configurations in ϕ. We notice also that the level of polar *VV* is more important than the other polar field; consequently, we use a different scale for this polarization to maintain a contrasting image.

It is worthwhile to note that the presence of a metallic target significantly enlarges the aperture of the two main lobes of the pattern. This leads us to the conjecture that the most desirable bi-static angular directions for detecting metallic objects are not in the back- and forward-scattering directions (using *HH* and *VV* polarisations) but in the angular ranges that skirt these angles instead.

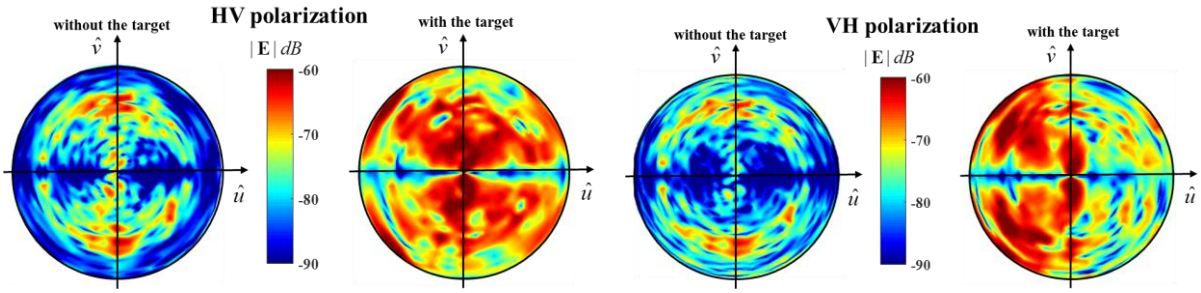

(a) (b)

Figure 4.48. Influence of the presence of a metallic target in a forest environment on the amplitude of the cross-polar *VH* and *HV* for the incident angle $(\theta_{inc},\phi_{inc}) = (45°,0°)$: (a) without the target (dB). (b) in presence of the target (dB).

Additionally, we investigate the effect of the presence of the forest on the radar cross-section of the tank, and we also treat the same scene for a monostatic configuration (*HH* polarization). The results of comparison are given in Fig.4.49a. It can be seen from this figure that the presence of the tank affects the RCS of the forest and depends on the position of the tank in the forest and the surrounding trees. For the other case of co-polarization (*VV*), the difference between the RCS of the forest alone and that of the forest in the presence of target is less obvious.

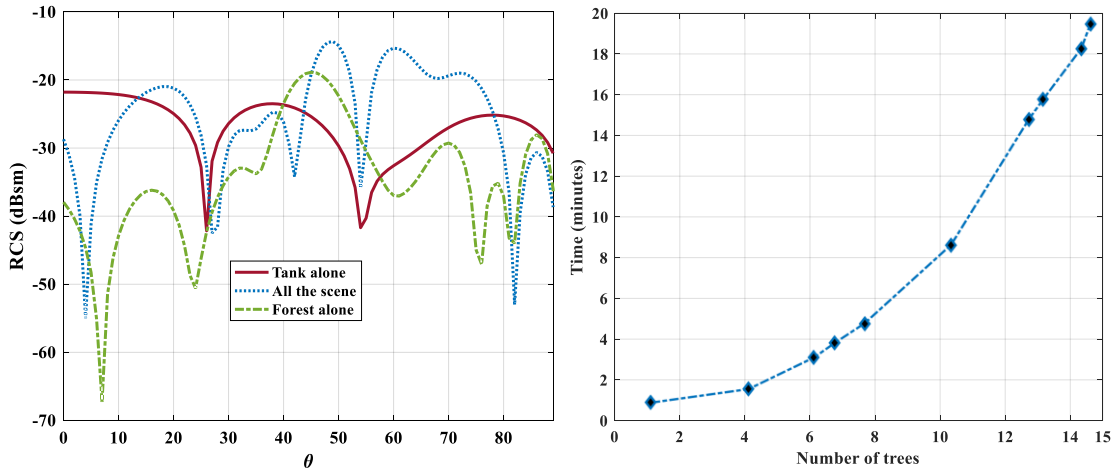

(a) (b)

Figure 4.49. (a)The effect of the forest on the polar *HH* monostatic RCS on theta of the tank. The incident field is a plane wave propagating along the direction defined by $0° \le \theta_{inc} \le 90°$ and $\phi_{inc} = 0°$. (b) Time consumption in terms of number of trees.

The simulation of the scene has been carried out on a shared memory computer (CPU Intel® CPU E5-1650 v3 with 128 Go RAM). The discretization of the scene leads to 773 670 unknowns (762 240 for the volume formulation and 11430 for the surface one). Using a CBFM-E for the forest the number of unknowns is reduced to 93223, thus realizing a compression rate (CR defined in [4.68]) of 8.17. The memory consumption for this complex scene is 96 514 Mb. The entire simulation takes 16h 25min for the bi-static case and 7h30min for the monostatic one. This simulation has been carried out by using a computer with a CPU Intel® i7 4600U and 16 Gb RAM). The execution time as a function of the number of trees (which is directly related to the number of unknowns) is shown in Fig. 4.89b.

Future work

1) Acceleration of the $\underline{\underline{\mathbf{Z}}}_{sv}$ matrix filling time

Each element $z_{i,v}^{sv}$ of the $n \times m$ rectangular matrix $\underline{\underline{\mathbf{Z}}}_{sv}$ represents the field radiated by the i-th RWG basis function in the center of the v-th volumetric cell. Since we are dealing with large scenarios, it follows that almost the totality of the dielectric cell centers are in the far-field region for each single basis function. Because of the nature of the Green's function, the matrix $\underline{\underline{\mathbf{Z}}}_{sv}$ will be numerically rank-deficient. In other words, the effective

rank of the matrix $r << \min(m,n)$. From this consideration it follows that in principle it is possible to recreate the information contained in $\underline{\underline{\mathbf{Z}}}_{sv}$ with a number of parameters smaller than the product $m \times n$.

To take advantage of this consideration we will investigate the use of the Adaptive Cross Approximation Algorithm (ACA) [4.77]. ACA is a purely algebraic procedure that aims to approximate $\mathbf{Z}_{m\times n}$ through a product form

$$\mathbf{Z}_{m\times n} \approx \bar{\mathbf{Z}}_{m\times n} = \mathbf{U}_{m\times r}\mathbf{V}_{r\times n} \tag{4.73}$$

by keeping the Frobenus norm of the relative error below a selected threshold ε, namely:

$$\left\|\mathbf{Z}_{m\times n} - \bar{\mathbf{Z}}_{m\times n}\right\| \le \varepsilon \left\|\mathbf{Z}_{m\times n}\right\|. \tag{4.74}$$

The interesting thing about this algorithm is that it approximates the original matrix by requiring only partial knowledge of the original matrix. In particular, the $\underline{\underline{\mathbf{Z}}}_{sv}$ matrix could be recreated by calculating only *r(m+n)* coupling terms and recreated with a complexity of $O\left(r^2\left(m+n\right)\right)$.

2) Compression of the $\underline{\underline{\mathbf{Z}}}_{ss}$ matrix

In the actual form of our formulation the matrix $\underline{\underline{\mathbf{Z}}}_{ss}$ is directly the EFIE-MoM coupling matrix of the metallic objects alone. Its size is directly related to the discretization of these objects (the size increase as the size and the geometrical complexity of the objects increase). Realistic complex targets could thus produce very large coupling matrices leading to extremely long computational time. Moreover, the EFIE suffers from ill-conditioning in the presence of dense discretizations [4.78]. This latter problem can be solved by using Calderon-based preconditioners [4.79]-[4.81].

In order to overcome these problems we plan to extend the CBF method to the metallic objects [reference]. Particular attention has to be taken in order to guarantee the continuity of the surface current at the interface between adjacent CBF.

The expected benefits by applying this procedure, based on a Singular Value Decomposition (SVD) of a matrix containing the current solution of each block illuminated with different sources, are: 1) an important matrix size compression; 2) the SVD filtering could improve the compressed matrix condition number.

3) New measurements campaign

A new measurements campaign has to be plan in order to validate experimentally the scattering of complex metallic objects in presence of a more realistic environment. The main issue will be the introduction of a realistic ground for two reasons: - the need of a uniform material with the desired complex dielectric constant; 2

4) Parallelization of the code

The model is in principle easily parallelizable. The volumetric interactions have been already successfully parallelized with an MPI implementation [4.82]. The next step will be the parallelization of the whole code for the hybrid formulation.

References

[4.59] M. R. Allen, J. M. Jauregui and L. E. Hoff, "FOPEN-SAR detection by direct use of simple scattering physics," Proceedings International Radar Conference, Alexandria, VA, 1995, pp. 152-157.

[4.60] Liao, DaHan, and Traian Dogaru. "Full-Wave Scattering And Imaging Characterization Of Realistic Trees For FOPEN Sensing". IEEE Geoscience and Remote Sensing Letters 13.7 (2016): 957-961.

[4.61] Sullivan, Anders. "Advanced Modeling and Simulation of Low Frequency Foliage Penetrating Radar." US Army Research Laboratory, Research Report (1995).

[4.62] K. Sarabandi, M. Dehmollaian and H. Mosallaei, "Hybrid FDTD and single-scattering theory for simulation of scattering from hard targets camouflaged under forest canopy," in IEEE Transactions on Geoscience and Remote Sensing, vol. 44, no. 8, pp. 2072-2082, Aug. 2006.

[4.63] M. Dehmollaian and K. Sarabandi, "Electromagnetic Scattering From Foliage Camouflaged Complex Targets," in IEEE Transactions on Geoscience and Remote Sensing, vol. 44, no. 10, pp. 2698-2709, Oct. 2006.

[4.64] Zhijun Liu, Jiangqi He, Yongjun Xie, A. Sullivan and L. Carin, "Multilevel fast multipole algorithm for general targets on a half-space interface," in IEEE Transactions on Antennas and Propagation, vol. 50, no. 12, pp. 1838-1849, Dec 2002.
[4.65] S. M. Rao, T. K. Sarkar, P. Midya and A. R. Djordevic, "Electromagnetic radiation and scattering from finite conducting and dielectric structures: surface/surface formulation," in IEEE Transactions on Antennas and Propagation, vol. 39, no. 7, pp. 1034-1037, July 1991.
[4.66] S. Bellez, C. Dahon and H. Roussel, "Analysis of the Main Scattering Mechanisms in Forested Areas: An Integral Representation Approach for Monostatic Radar Configurations," in IEEE Transactions on Geoscience and Remote Sensing, vol. 47, no. 12, pp. 4153-4166, Dec. 2009.
[4.67] I. Fenni, H. Roussel, M. Darces and R. Mittra, "Fast Analysis of Large 3-D Dielectric Scattering Problems Arising in Remote Sensing of Forest Areas Using the CBFM," in IEEE Transactions on Antennas and Propagation, vol. 62, no. 8, pp. 4282-4291, Aug. 2014.
[4.68] R. Mittra, K. Du, "Characteristic basis function method for iteration-free solution of large method of moments problems", Progr. Electromagn. Res. B, vol. 6, pp. 307-336, Apr. 2008.
[4.69] S. Rao, D. Wilton and A. Glisson, "Electromagnetic scattering by surfaces of arbitrary shape," in IEEE Transactions on Antennas and Propagation, vol. 30, no. 3, pp. 409-418, May 1982.
[4.70] Michalski, Krzysztof A. "The mixed-potential electric field integral equation for objects in layered media." Archiv für elektronik und übertragungstechnik 39 (1985): 317-322.
[4.71] K. A. Michalski and D. Zheng, "Electromagnetic scattering and radiation by surfaces of arbitrary shape in layered media. I. Theory," in IEEE Transactions on Antennas and Propagation, vol. 38, no. 3, pp. 335-344, Mar 1990.
[4.72] K. A. Michalski and D. Zheng, "Electromagnetic scattering and radiation by surfaces of arbitrary shape in layered media. II. Implementation and results for contiguous half-spaces," in IEEE Transactions on Antennas and Propagation, vol. 38, no. 3, pp. 345-352, Mar 1990.
[4.73] H. Nguyen, H. Roussel and W. Tabbara, "A coherent model of forest scattering and SAR imaging in the VHF and UHF-band," in IEEE Transactions on Geoscience and Remote Sensing, vol. 44, no. 4, pp. 838-848, April 2006.
[4.74] M. I. Aksun, "A robust approach for the derivation of closed-form Green's functions," in IEEE Transactions on Microwave Theory and Techniques, vol. 44, no. 5, pp. 651-658, May 1996.
[4.75] A. Alparslan, M. I. Aksun and K. A. Michalski, "Closed-Form Green's Functions in Planar Layered Media for All Ranges and Materials," in IEEE Transactions on Microwave Theory and Techniques, vol. 58, no. 3, pp. 602-613, March 2010.
[4.76] Geffrin, J. M., Sabouroux, P., & Eyraud, C. (2005). Free space experimental scattering database continuation: experimental set-up and measurement precision. inverse Problems, 21(6), S117
[4.77] K. Zhao, M. N. Vouvakis, and Jin-Fa Lee, "The Adaptive Cross Approximation Algorithm for Accelerated Method of Moments Computations of EMC Problems," IEEE Trans. on Electromagnetic Compability, Vol. 47, No. 4, pp. 763-773, Nov. 2005
[4.78] K. F. Warnick and W. C. Chew, "On the spectrum of the electric field integral equation and the convergence of the moment method,"International Journal for Numerical Methods in Engineering, vol. 51, no. 1, pp. 31–56, 2001.
[4.79] R. J. Adams, "Physical and analytical properties of a stabilized electric field integral equation," IEEE Trans. Antennas Propagation, vol. 52,pp. 362–372, Feb. 2004.
[4.80] H. Contopanagos, B. Dembart, M. Epton, J. Ottusch, V. Rokhlin, J. Visher, and S. M. Wandzura, "Well-Conditioned Boundary IntegralEquations for Three-Dimensional Electromagnetic Scattering," IEEE Trans. Antennas Propagation, vol. 50, pp. 1824–1930, Dec. 2002.
[4.81] F. P. Andriulli, K. Cools, H. Bagci, F. Olyslager, A. Buffa, S. Christiansen, and E. Michielssen, "A Multiplicative Calderon Preconditionerfor the Electric Field Integral Equation," IEEE Trans. Antennas Propagation, vol. 56, no. 8, pp. 2398–2412, 2008.
[4.82] M. Fall, H. Roussel, C. Dahon, M. Casaletti, I. Fenni et al, "A high performance MPI implementation of numerical modeling of electromagnetic scattering from forest environment," Conference IEEE APS 2016, Jun 2016, Fajardo (Porto-Rico), United States. 2016, AP-S/URSI 2016

Conclusion

This HDR thesis summarizes the professional activities I have conducted this last decade, both before and after I joined Sorbonne. The presented research project, dealing with the implementation of planar aperture field antennas, represents the natural junction between the different activities I have been working: antenna design, metamaterials, and numerical methods. The novelty of the project is the strong interaction between different techniques coming from these domains (aperture field optimization, numerical analysis and antenna physics).
Aperture field reconstruction using three planar complementary technologies has been exposed:

A) **Slot antennas.** Slot antennas are very well known in the antenna community. However, to the best of my knowledge, few works are present in the literature about the aperture field reconstruction. A new technique for the implementation of a general aperture distribution has been presented and will be improved in the next years in order to prevent undersampling problems. ***Weak point***: only discrete distribution can be implemented. ***Strong point:*** the primary feeder radiates inside a parallel plate waveguide and do not contribute directly to the radiated field.

B) Metasurface antenna. Metasurface antennas based on the conversion of a surface wave into leaky wave have recently been introduced. Some interesting examples have been published for far field applications. However, these design procedures are very complicated and not general leading to limited degrees of freedom in the radiation pattern. A completely different approach enabling the aperture field synthesis has been introduced and preliminary examples in the near and far field region presented. The future research will be focalised in the bandwidth enhancement. Some reconfigurable structures as for example LCD technology will also be considered. ***Weak points***: The feeder is placed above the metasurface to excite the desired surface-wave. It radiates also a spurious field in the free space that can limit the antenna performance. ***Strong point:*** continuous distribution can be implemented.

C) **Shaped surfaces**. Shaped reflectors as Fourier grating, etc. have been used in the past to design beam splitters and other devices at THz regime. These devices are based on periodic profiles, where the period is determined by the desired angle between beams. This aspect limits the versatility of these solutions for the following reasons: 1) the beam directions are dictated by the periodicity, thus it is not possible to radiate to customary directions; 2) it is very hard to independently control the shape and the energy associated to each beam; 3) the periodic nature of the surface will excite non-desired harmonics. The proposed aperture field shaped surface does not suffer in principle of these restrictions. Further developments are necessary to optimize the procedure. The possibility to improve the transmissive solution using a transmittaray will be deeply investigated in the next years. ***Weak points***: The profile is no more periodic, this means that the alignment has to be done very carefully. The bandwidth is narrow. ***Strong point:*** continuous distribution can be implemented. This means that this technique can be used to design planar lenses etc.

In conclusion, my perspective for the next years consists in continuing to develop analytical and numerical models for electromagnetics. The particularity of these models is that they are not general purpose tools but they are targeted to particular applications in order to take advantage of the physics of the problem. The natural desired output is the design of novel planar antennas. Furthermore, I would like to continue my scientific collaborations and developing new ones with both academics and industrials.

Appendix: List of Publications

In this appendix are listed the publications I have authored and co-authored in peer-reviewed journals, books and conferences.

Type	Number
Journal Articles	29
Invited International Conference Papers	19
International Conference Papers	58
National Conference Papers	12
Book chapter	1

Journal Articles (Articles dans des revues de catégorie A)

[P.1] S. Razafimahatratra, J. Sarrazin, G. Valerio, F. Sarrazin, **M. Casaletti**, P. De Doncker, and A. Benlarbi-Delai, "Input Impedance of an Aperture Over a Lossy Half-Space: Application to on-Body Antenna Performance at 60 GHz ," *Progress In Electromagnetics Research C*, Vol. 83, pp. 161-178, 2018.
[P.2] M. Teniou, H. Roussel, M. Serhir, N. Capet, G. Piau, **M. Casaletti**, "Tensorial metasurface antennas radiating polarized beams based on aperture field implementation," in *International Journal of Microwave and Wireless Technologies*, 10(2), pp. 161-168. 2018
[P.3] L. Hettak, H. Roussel, **M Casaletti**, R. Mittra, "A Numerically Efficient Method for Predicting the Scattering Characteristics of a Complex Metallic Target Located Inside a Large Forested Area," in *IEEE Transactions on Geoscience and Remote Sensing*, vol. 56, no. 2, pp. 1177-1185, Feb. 2018.
[P.4] M. Teniou, H. Roussel, N. Capet, G. Piau and **M. Casaletti**, "Implementation of radiating aperture field distribution using tensorial metasurfaces," in *IEEE Transactions on Antennas and Propagation*, vol. 65, no. 11, pp. 5895-5907, Nov. 2017.
[P.5] Q. Zhang, J. Sarrazin, **M. Casaletti**, P. De Doncker and A. Benlarbi-delaï, "Assessment of on-body skin-confined propagation for Body Area Network," in *IEEE Antennas and Wireless Propagation Letters*, vol. 16, pp. 2610-2613, 2017.
[P.6] D. Comite, G. Valerio, M. Albani, A. Galli, **M. Casaletti** and M. Ettorre, "Exciting Vorticity Through Higher Order Bessel Beams With a Radial-Line Slot-Array Antenna," in *IEEE Transactions on Antennas and Propagation*, vol. 65, no. 4, pp. 2123-2128, April 2017.
[P.7] M. Casaletti, G. Valerio, R. Sauleau and M. Albani, "Mode-Matching Analysis of Lossy SIW Devices," in *IEEE Transactions on Microwave Theory and Techniques*, vol. 64, no. 12, pp. 4126-4137, Dec. 2016.
[P.8] I. Iliopoulos, **M. Casaletti**, R. Sauleau, P. Pouliguen, P. Potier and M. Ettorre, "3-D Shaping of a Focused Aperture in the Near Field," in *IEEE Transactions on Antennas and Propagation*, vol. 64, no. 12, pp. 5262-5271, Dec. 2016.
[P.9] F. Defrance, **M. Casaletti**, J. Sarrazin, M. C. Wiedner, H. Gibson, G. Gay, R. Lefèvre, and Y. Delorme, "Structured surface reflector design for oblique incidence beam splitter at 610 GHz," *Optic Express*, vol. 24, Issue 18, pp. 20335-20345 (2016).
[P.10] M. Casaletti, M. Śmierzchalski, M. Ettorre, R. Sauleau and N. Capet, "Polarized Beams Using Scalar Metasurfaces," in *IEEE Transactions on Antennas and Propagation*, vol. 64, no. 8, pp. 3391-3400, Aug. 2016.
[P.11] S. C. Pavone, M. Ettorre, **M. Casaletti**, and M. Albani, "Transverse circular-polarized Bessel beam generation by inward cylindrical aperture distribution," *Optic Express*, vol. 24, Issue 10, pp.11103-11111 (2016).
[P.12] M. Ettorre, F. Foglia Manzillo, **M. Casaletti,** R. Sauleau, L. Le Coq, N. Capet, "Continuous Transverse Stub Array for Ka-Band Applications," in *Antennas and Propagation, IEEE Transactions on*, vol.63, no.11, pp.4792-4800, Nov. 2015.
[P.13] F. Foglia Manzillo, M. Ettorre, **M. Casaletti**, N. Capet, R. Sauleau, "Active Impedance of Infinite Parallel-Fed Continuous Transverse Stub Arrays," in *Antennas and Propagation, IEEE Transactions on*, vol.63, no.7, pp.3291-3297, July 2015.

[P.14] M. Ettorre, S.C. Pavone, **M. Casaletti,** M. Albani, "Experimental Validation of Bessel Beam Generation Using an Inward Hankel Aperture Distribution," in *Antennas and Propagation, IEEE Transactions on* , vol.63, no.6, pp.2539-2544, June 2015.
[P.15] M. Albani, S. Pavone, **M. Casaletti**, M. Ettorre," Generation of non-diffractive Bessel beams by inward cylindrical traveling wave aperture distributions," Optics Express 22(15), July 2014.
[P.16] M. Ettorre, **M. Casaletti,** G. Valerio, R. Sauleau, L. Le Coq, S. C. Pavone, M. Albani, "On the Near-Field Shaping and Focusing Capability of a Radial Line Slot Array," in *Antennas and Propagation, IEEE Transactions on*, vol.62, no.4, pp.1991-1999, April 2014.
[P.17] M. Casaletti, G. Valerio, J. Seljan, M. Ettorre, R. Sauleau, "A Full-Wave Hybrid Method for the Analisys of Multilayered SIW-based Antennas," *IEEE Transactions on Antennas and Propagations*, vol.61, no.11, pp.5575-5588, Nov. 2013.
[P.18] G. Valerio, **M. Casaletti**, J. Seljan, R. Sauleau, M. Albani, "Efficient Computation of the Coupling Between a Vertical Line source and a slot," *IEEE Transactions on Antennas and Propagations*, vol.61, no.12, pp.6084-6093, Dec. 2013.
[P.19] M. Casaletti, S. Maci, "Aperture Beam Expansion by Using a Spectral 2D-GPOF method", *Progress In Electromagnetic Research M*, Vol. 28, pp. 245-257, 2013.
[P.20] E. Gandini, M. Ettorre, **M. Casaletti**, L. Le Coq and R. Sauleau, "SIW Slotted Waveguide Array With Pillbox Transition For Mechanical Beam Scanning", *Antenna and Wireless Propagation Letters*, Vol. 11, pp.1572-1575.
[P.21] M. Casaletti, R. Sauleau, S. Maci, M. Ettorre, "Efficient Analysis of Metallic and Dielectric Posts in Parallel-Plate Waveguide Structures", *IEEE Transactions on Microwave Theory and Techniques*, vol. 60, n.10, pp. 2979 - 2989, October 2012.
[P.22] M. Casaletti, S. Maci, G. Vecchi, "Entire-Domain Basis Functions for Scattering from Large Curved Surfaces Formulated by Transformation Optics", *IEEE Transactions on Antennas and Propagations*, Vol. 60, n.9, pp. 4271 – 4280, September 2012.
[P.23] M. Bosiljevac, **M. Casaletti**, F. Caminita, Z. Sipus, and S. Maci, "Non-Uniform Metasurface Luneburg Lens Antenna Design ," *IEEE Transactions on Antennas and Propagations*, Vol. 60, n.9, pp. 4065 – 4073, September 2012.
[P.24] S. Maci, G. Minatti, **M. Casaletti**, and M. Bosiljevac, "Metasurfing: Addressing Waves on Impenetrable Metasurfaces", *Antenna and Wireless Propagation Letters*, Vol. 10, pp. 1499 – 1502, 2011.
[P.25] G. Minatti, F. Caminita, **M. Casaletti**, and S. Maci, "Spiral leaky-wave antennas based on modulated surface impedance," *IEEE Transactions on Antennas and Propagations*, Vol. 59, n. 12, pp. 4436 – 4444, December 2011.
[P.26] M. Casaletti, S. Maci, and G. Vecchi, "A complete set of linear-phase basis functions for scatterers with flat faces and for planar apertures," *IEEE Transactions on Antennas and Propagations*, Vol.59 n.2, pp.563-573, February 2011.
[P.27] S. Škokić, **M. Casaletti**, S. Maci and S. B. Sørensen, "Complex conical beams for aperture field representations," *IEEE Transactions on Antennas and Propagations*, Vol.59 n.2, pp.611-622, February 2011.
[P.28] M. Casaletti, S. Maci and G. Vecchi "Diffraction-like synthetic functions to treat the scattering from large polyhedral metallic objects," *Advanced Computational Electromagnetic Society*, Vol.24, N.2, 2009.
[P.29] S. Maci, A. Cucini, M. Caiazzo, and **M. Casaletti**, "A pole-zero matching method for EBG surfaces composed of a dipole FSS printed on a grounded dielectric slab," *IEEE Transactions on Antennas and Propagations* Vol.53, n.1, pp.70-81, January 2005.

Invited International Conference Papers (Articles invités dans de conférences internationales avec comités de lecture)

[IC.1] L. Hettak, H. Saleh, C. Dahon, **M. Casaletti**, O. Meyer, J.M. Geffrin, "DEMOS : a Domain dEcomposition MOdel for Scattering in forest environments compared with mono and bistatic measurements on scaled models," ICEAA 2017 International Conference on Electromagnetics in Advanced Applications, September 2017 Verona, Italy.
[IC.2] G. Valerio, **M. Casaletti**, J. Seljan, M. Ettorre, R. Sauleau, M. Albani, "Numerical-Asymptotic Synergic Approach for Speeding Up the Filling Time in a MoM/Mode Matching Code for Large SIW Structures", *EUropean Conference on Antennas and Propagation (EUCAP-2014)*, The Hague (Pays-Bas), avril 2014.
[IC.3] G. Valerio, **M. Casaletti**, J. Seljan, M. Ettorre R. Sauleau, and M. Albani, "Numerical-asymptotic synergic approach for speeding up the filling time in a MoM/mode matching code for large SIW structures," at ***INTELECT'2013***, Dubrovnik, Croatia, 14-15 Oct. 2013.
[IC.4] M. *Casaletti, G. Valerio, J. Seljan and M. Ettorre, "A Full-wave Hybrid Method for the Fast Analysis of SIW-based Antennas" EuCAP 2013, Gothenburg.*

[IC.5] G. Valerio, **M. Casaletti**, J. Seljan, M. Ettorre, and R. Sauleau "Optimized Analysis of Slotted Substrate Integrated Waveguides by a Method-of-Moments Mode-Matching Hybrid Approach," *International Conference on Electromagnetics in Advanced Applications (ICEAA)*, Turin, 2013.
[IC.6] M. Casaletti, R. Sauleau, S. Maci, and M. Ettorre, ''Mode matching method for the analysis of substrate integrated waveguides," *EuCAP 2012*, Prague.
[IC.7] G. Minatti, F. Caminita, P. De Vita, **M. Casaletti** and S. Maci, "Circularly polarized metasurfing antennas," *International Congress on Advanced Electromagnetic Materials in Microwave and Optics*, Barcelona Spain, 10-15 October 2011.
[IC.8] M. Casaletti, S. Maci, and G. Vecchi, "A large domain complete basis function set for curved surfaces," *URSI General Assembly and Scientific Symposium of International Union of Radio Science*, Istanbul Turkey, 13-20 August 2011.
[IC.9] M. Casaletti, E. Martini, and S. Maci, "Field expansion in terms of conical and localized beams," *URSI General Assembly and Scientific Symposium of International Union of Radio Science*, Istanbul Turkey, 13-20 August 2011.
[IC.10] G. Minatti, F. Caminita, **M. Casaletti**, and S. Maci, "Design criteria for spiral metasurfaces Antennas," *IEEE AP-S International Symposium 2011*, Spokane USA, July 3-8, 2011.
[IC.11] M. Casaletti; S. Maci, and S. Skokic, "Generation of beams by aperture field spectra," *EuCAP-2011*, Rome Italy, 11-15 April 2011.
[IC.12] M. Bosiljevac, **M. Casaletti**, F. Caminita, and S. Maci, "Highly tapered, uniform phased horn based on variable impedance lens effect," *EuCAP-2011*, Rome Italy, 11-15 April 2011.
[IC.13] S. Skokic, **M. Casaletti**, S. Maci, and S. Sorensen, "Beam-waveguide analysis using complex conical beams," *EuCAP-2011*, Rome Italy, 11-15 April 2011.
[IC.14] G. Minatti, F. Caminita, **M. Casaletti**, and S. Maci, "Leaky wave circularly polarized antennas based on surface impedance modulation," *ICECom 2010*, Dubrovnik Croatia, Sept. 20-23 2010.
[IC.15] M. Casaletti, S. Maci, and G. Vecchi , "A complete basis function set for curved surfaces," *EMTS-2010 U.R.S.I.*, Berlin Germany Aug. 16-19, 2010.
[IC.16] M. Casaletti, S. Skokic, S. Maci, and S. Sørensen "Beam expansion in multi-reflector quasi-optical systems," *EuCAP-2010*, Barcelona Spain, 12-16 April 2010.
[IC.17] M. Casaletti, S. Maci, and G. Vecchi, "Global Generalized Shannon Functions for the Scattering of 3-D Polyhedral Surfaces," *EuCAP-2010*, Barcelona Spain, 12-16 April 2010.
[IC.18] M. Casaletti, F. Caminita, and S. Maci, "Lens Effect in Parallel Plate Waveguide by Using a Metamaterial Surface," *EuCAP-2010*, Barcelona Spain, 12-16 April 2010.
[IC.19] M. Casaletti, S. Maci, and G. Vecchi, "Generalized Shannon Basis function for Curved Surfaces," *EuCAP-2010*, Barcelona Spain, 12-16 April 2010.

International Conference Papers (Articles dans des conférences internationales avec comités de lecture)

[C.1] S. C. Pavone, **M. Casaletti**, and M. Albani, "Design and Optimization of a Circular Polarized Linear Array in SIW for Last-Mile Application," *IEEE APS* 2018, 8-13 July 2018, Boston, USA.
[C.2] H. Mohamad, T. Zheng, **M. Casaletti**, Z. Ren, A. Abdelshafy, F. Capolino, G. Valerio, "Degenerate Band Edge Condition in Substrate-Integrated Waveguides," *IEEE APS* 2018, 8-13 July 2018, Boston, USA.
[C.3] S. C. Pavone, **M. Casaletti**, and M. Albani, "Automatic Design of a Rhcp Linear Slot Array in Substrate Integrated Waveguide" *EuCAP-2018*, London, England, 9-13 Avril 2018.
[C.4] M. Teniou, H. Roussel, N. Capet, G. Piau and **M. Casaletti**, "Modulated Tensorial Metasurfaces for Aperture Field Generation," *EuCAP-2017*, Paris, France, 19-24 March 2017.
[C.5] L. Hettak, H. Roussel, **M. Casaletti**, C. Dahon, R. Mittra, "Hybrid Formulation for the Electromagnetic Analysis of Metallic Objects Placed in Natural Environments," *EuCAP-2017*, Paris, France, 19-24 March 2017.
[C.6] Q. Zhang, J. Sarrazin, **M. Casaletti**, L. Petrillo, P. De Doncker, A. Benlarbi-Delaï, "On-Body Skin Confined Propagation for Body Area Networks (BAN)," *EuCAP-2017*, Paris, France, 19-24 March 2017.
[C.7] F. Defrance, **M. Casaletti**, J. Sarrazin, M.C. Wiedner, H. Gibson, G. Gay, R. Lef`evre, Y. Delorme, "Structured Surface Design to Generate Any Beam Pattern at THz Frequencies," *EuCAP-2017*, Paris, France, 19-24 March 2017.
[C.8] J. Sarrazin, G. Valerio, S. Razafimahatratra, **M. Casaletti**, F. Sarrazin, L. Petrillo, P. De Doncker, A. Benlarbi-Delai Aziz, "Antenna Radiation Efficiency Considerations in Body Area Networks," *BODYNETS*, Turin, 15-16 December 2016.
[C.9] M.Teniou, H.Roussel, N.Capet, G.-P.Piau, **M.Casaletti**, "Complex aperture field generation using tensorial metasurfaces," *IEEE APS 2016*, Jun 2016, Fajardo (Porto-Rico), United States. 2016, AP-S/URSI 2016.
[C.10] I. Iliopoulos, M. Ettorre, R. Sauleau, **M. Casaletti**, P. Potierz and P. Pouliguen, "3D Focal Spot Manipulation at Millimeter Waves," *IEEE APS 2016*, Jun 2016, Fajardo (Porto-Rico), United States. 2016, AP-S/URSI 2016.

[C.11] M. Fall, H. Roussel, C. Dahon, **M. Casaletti**, R. Mittra, "A high performance MPI implementation of numerical modeling of electromagnetic scattering from forest environment," *IEEE APS 2016*, Jun 2016, Fajardo (Porto-Rico), United States. 2016, AP-S/URSI 2016.
[C.12] I. Iliopoulos, M. Ettorre, R. Sauleau, **M. Casaletti**, P. Potierz and P. Pouliguen, "3D Near-Field Shaping of a Focused Aperture," *EuCAP 2016*, Apr 2016, Davos, Switzerland. pp.1 - 4, 2016, *10th European Conference on Antennas and Propagation.*
[C.13] S. Pavone, M. Ettorre, M. Casaletti, M. Albani, "Analysis and design of CP Bessel beam launchers," *EuCAP 2016*, Apr 2016, Davos, Switzerland. pp.1 - 4, 2016, 10th European Conference on Antennas and Propagation.
[C.14] M. Casaletti, M. Smierzchalski, M. Ettorre, Ronan Sauleau, and Nicolas Capet, "Scalar metasurface antennas able to radiate polarized tilted beam," *First International Workshop on Metamaterials-by-Design*, 3-4 December 2015, Paris Saclay, France.
[C.15] M. Ettorre, F. Foglia Manzillo, **M. Casaletti**, R. Sauleau, N. Capet, "A Compact and High-gain Ka-band Multibeam Continuous Transverse Stub Antenna," *Antennas and Propagation Society International Symposium (APSURSI)*, Vancouver (Canada), July 2015.
[C.16] M. Casaletti, G. Valerio, R. Sauleau, M. Albani, "Rigorous Losses Evaluation in the Numerical Analysis of SIW Structures," *EUropean Conference on Antennas and Propagation (EUCAP-2015)*, Lisbon (Portugal), April 2015.
[C.17] F. Foglia Manzillo, M. Ettorre, **M. Casaletti**, R. Sauleau, N. Capet , "Modeling and Design of ParallelFed Continuous Transverse Stub (CTS) Arrays," *EUropean Conference on Antennas and Propagation (EUCAP-2015)*, Lisbon (Portugal), April 2015.
[C.18] M. Smierzchalski, **M. Casaletti**, M. Ettorre, R. Sauleau, N. Capet, "Scalar Metasurface Antennas with Tilted Beam," *EUropean Conference on Antennas and Propagation (EUCAP-2015)*, Lisbon (Portugal), April 2015.
[C.19] F. Defrance, **M. Casaletti**, J. Sarrazin, M. Wiedner, Y. Delorme, G. Gay, R. Lefevre," Non-periodic phase gratings," ISSTT 2015 (26th International Symposium on Space Terahertz Technology), Cambridge, Massachusetts, U.S.A.; 03/2015.
[C.20] M. Ettorre, **M. Casaletti**, G. Valerio, R. Sauleau, L. Le Coq, S. C Pavone, M. Albani, "Automatically optimized near-field focusing radial line slot array," *Antennas and Propagation Society International Symposium (APSURSI), 2014 IEEE*; 07/2014.
[C.21] G. Valerio, **M. Casaletti**, J. Seljan, R. Sauleau, M. Albani, "Efficient computation of post-slot interactions in complex layered media with vertical interconnects," *Antennas and Propagation Society International Symposium (APSURSI), 2014 IEEE*; 07/2014.
[C.22] M. Ettorre, **M. Casaletti**, G. Valerio, L. Le Coq, R. Sauleau, S.C. Pavone, M. Albani, "*A Radial Line Slot Array Focusing in the Near Field: Analysis and Design*" *EUropean Conference on Antennas and Propagation (EUCAP-2014)*, The Hague (Pays-Bas), avril 2014.
[C.23] J. Seljan, G. Valerio, **M. Casaletti**, K. Tekkouk, M. Ettorre, R. Sauleau, " *Hybrid MoM/Mode-Matching Method for SIW Devices Housing Layered Dielectric Substrates*", *EUropean Conference on Antennas and Propagation (EUCAP-2014)*, The Hague (Pays-Bas), avril 2014.
[C.24] M. Ettorre, **M. Casaletti**, G. Valerio, R. sauleau, L. Le Coq, S.C. Pavone, M. Albani, "Automatically Optimized Near-Field Focusing Radial Line Slot Array", *IEEE Antennas and Propagation Symposium (APS)*, Memphis (USA), juillet 2014.
[C.25] M. Albani, S.C. Pavone, **M. Casaletti**, M. Ettorre, "Non-diffractive Hankel beams", *IEEE Antennas and Propagation Symposium (APS)*, Memphis (USA), juillet 2014;
[C.26] G. Valerio, **M. Casaletti**, J. Seljan, R. Sauleau, M. Albani ,"Efficient Computation of Post-Slot Interactions in Complex Layered Media with Vertical Interconnects", *IEEE Antennas and Propagation Symposium (APS)*, Memphis (USA), juillet 2014.
[C.27] Anthony Grbic, Jason Heebl, **M. Casaletti**, M. Ettorre, M. F. Imani "Generating Bessel Beams with Planar Structures", *IEEE Antennas and Propagation Symposium (APS)*, Memphis (USA), juillet 2014.
[C.28] M. Casaletti, G. Valerio, J. Seljan, R. Sauleau, M. Albani , "Efficient Analysis of Lossy Substrate Integrated Waveguide Structures", *IEEE Antennas and Propagation Symposium (APS)*, Memphis (USA), juillet 2014.
[C.29] M. Albani, **M. Casaletti**, M. Ettorre, G. Valerio, R. Sauleau, "A New Synthesis Technique for Nera-Field Focusing Systems," *IEEE AP-S International Symposium*, 2013.
[C.30] M. Casaletti, G. Valerio, J. Seljan, M. Ettorre, R. Sauleau, "Efficient Analysis of SIW-based Antenna Geometries Through a Rigorous Mode-Matching Approach," *IEEE AP-S International Symposium*, 2013.
[C.31] M. Ettorre, **M. Casaletti**, A. Grbic, "Power Link budget for Propagating Bessel beams," *IEEE AP-S International Symposium*, 2013.

[C.32] S. Skokic, Z. Sipus, S. Maci, M. Bosiljevac, **M. Casaletti**, "Application of complex conical beams in reflector system analysis," *International Conference on Mathematical Methods in Electromagnetic Theory (MMET)*, 2012
[C.33] K. Tekkouk, M. Ettorre, R. Sauleau, **M. Casaletti**, "Compact multibeam rotman lens antenna in SIW technology," *IEEE AP-S International Symposium*, 2012.
[C.34] M. Bosiljevac, **M. Casaletti**, Z. Sipus, F. Caminita, and S. Maci, "Designing Horn Antennas Based on Variable Metasurface Concept," *EUCAP 2012*, Prague.
[C.35] Skokic, **M. Casaletti**, M. Bosiljevac, Z. Sipus, and S. Maci, "Analysis of Curved Frequency Selective Reflector Antenna Systems - a Combined Approach," *EUCAP 2012*, Prague.
[C.36] K. Tekkouk, M. Ettorre, R. Sauleau, and **M. Casaletti**, "Folded Rotman Lens," *EUCAP 2012*, Prague.
[C.37] Nguyen Ngoc Tinh, **M. Casaletti**, T.V. La, R. Sauleau, "Synthesized elliptical lens with optimized extension for focal array fed lens antennas," *EUCAP 2012*, Prague.
[C.38] T. V. La; Ngoc Nguyen Tinh, **M. Casaletti**, R. Sauleau, "Design of medium-size dielectric bifocal lenses for wide-angle beam scanning antennas," *EuCAP 2012*, Prague.
[C.39] M. Casaletti, S. Maci, and S. Skokic, "Beams Generation by Aperture Field Spectra," *IEEE AP-S International Symposium 2011*, Spokane USA, July 3-8, 2011.
[C.40] M. Casaletti, F. Caminita, S. Maci, M. Bosiljevac, and Z. Sipus, "New Type of Horn Based on Variable Metasurface," *IEEE AP-S International Symposium 2011*, Spokane USA, July 3-8, 2011.
[C.41] G. Minatti, **M. Casaletti**, F. Caminita, P. De Vita, and S. Maci, "Planar antennas based on surface-to-leaky wave transformation," *EuCAP-2011*, Rome Italy, 11-15 April 2011.
[C.42] M. Casaletti, S. Maci, and G. Vecchi, "Complete basis functions set for curved scatterers based on Shannon sampling theorem," *IEEE AP-S International Symposium 2010*, Toronto Canada, July 11-17, 2010.
[C.43] M. Casaletti, S. Skokic, S. Maci, and S. Sørensen, "Different types of circular domain wave-objects," *IEEE AP-S International Symposium 2010*, Toronto Canada, July 11-17, 2010.
[C.44] M. Casaletti, F. Caminita, and S. Maci, "Luneburg lens designed by using a variable artificial surface," *IEEE AP-S International Symposium 2010*, Toronto Canada, July 11-17, 2010.
[C.45] M. Casaletti, S. Maci, and G. Vecchi, "Global generalized Shannon functions for the scattering of 3D polyhedral surfaces," *IEEE AP-S International Symposium 2010*, Toronto Canada, July 11-17, 2010.
[C.46] M. Casaletti, S. Maci, and G. Vecchi, "Orthogonal MoM basis functions based on spectral sampling," *IEEE AP-S International Symposium*, 2009.
[C.47] M. Casaletti, S. Maci, and G. Vecchi, "Comparison between sets of synthetic basis functions based on different generating processes," *IEEE AP-S International Symposium*, 2009.
[C.48] M. Casaletti, S. Skokic, S. Maci, and S. Sorensen, "Conical Beams for the analysis of Beam Waveguides," *IEEE AP-S International Symposium*, 2009.
[C.49] G. Carli, E. Martini, A. Borzi, **M. Casaletti**, and S. Maci, "Beam analysis of multireflector systems," *URSI* 2009.
[C.50] S. Skokic, **M. Casaletti**, S. Maci, and S. Sorensen, "Complex conical beam expansion for the analysis of beam waveguides," *EuCAP-2009*, Berlin Germany, 23-27 March 2009.
[C.51] M. Casaletti, S. Maci, and G. Vecchi, "PO synthetic function based on spectral domain sampling for the treatment of EM scattering from large flat surfaces," *IEEE AP-S International Symposium*, 5-11 July 2008.
[C.52] M. Casaletti, S. Maci, and G. Vecchi, "A synthetic function approach to the scattering from large objects by using incremental diffraction-type basis functions," *ICEAA '07 International Conference on Electromagnetics in Advanced Applications*, Torino Italy, 17-21 September 2007.
[C.53] M. Casaletti, S. Maci, and G. Vecchi, "Edge-generated synthetic basis functions for large scattering problems," *EMTS 2007 International Symposium on Electromagnetic Theory*, Ottawa Canada, 26-28 July 2007.
[C.54] M. Casaletti, S. Maci, and G. Vecchi, "An iteration-free approach to the scattering from large objects by using incremental diffraction-type basis functions," *IEEE AP-S International Symposium*, Honolulu Hawai'i USA, 10-15 June 2007.
[C.55] M. Casaletti, F. Molinet, and J. Fortuny-Guasch, "Field diffracted by a target in front of a flat rough surface: a perturbation method approach," *URSI Kleinheubacher Tagung 2004*, Miltenberg (Germany), 27 Sept.-01 Oct. 2004.
[C.56] S. Maci, **M. Casaletti**, M. Caiazzo, and A. Cucini, "Dispersion analysis of printed periodic structures by using a pole-zero network synthesis," *ICECOM 2003*, Dubrovnik, October 1-5 2003.
[C.57] S. Maci, **M. Casaletti**, M. Caiazzo, and A. Cucini, "Band-Gap properties of artificial surfaces", Special session on "Metamaterials: Electromagnetic Bandgap (EBG) Media," I*CEAA*, Torino, September 8-12, 2003.
[C.58] S. Maci, **M. Casaletti**, M. Caiazzo, and C. Boffa, "Dispersion properties of periodic grounded structures via equivalent network synthesis," *IEEE AP-S Symp*., Columbus, Ohio, June 22-27, 2003.

National Conference Papers (Articles dans de conférences nationales avec comités de lecture)

[NC.1] L. Hettak, H. Roussel, **M. Casaletti**, C. Dahon, R. Mittra, "Modèle direct pour la détection de cibles métalliques dans un milieu naturel," 20èmes Journées Nationales Micro-Ondes, May 2017, Saint-Malo, France.
[NC.2] M. Teniou, H. Roussel, N. Capet, G-P. Piau, **M. Casaletti**, "Méthode de conception d'antennes à métasurfaces pour la génération de distribution arbitraire de champs d'ouvertures," 20èmes Journées Nationales Micro-Ondes, May 2017, Saint-Malo, France.
[NC.3] Q. Zhang, J. Sarrazin, **M. Casaletti**, L. Petrillo, P. D. Doncker, A Benlarbi-Delaï, " Analyse de propagation confinée dans la peau pour le réseau corporel BAN (Body Area Network) ," 20èmes Journées Nationales Micro-Ondes, May 2017, Saint-Malo, France.
[NC.4] L. Hettak, H. Roussel, **M. Casaletti**, I. Fenni, R. Mittra, "Formulation hybride pour l'étude de la diffraction de cibles placées en environnements naturels," ARMIF 2016, Paris, France.
[NC.5] L. Hettak, H. Roussel, **M. Casaletti**, I. Fenni, R. Mittra, "Formulation hybride pour l'étude de la diffraction de cibles placées en environnements naturels," XIXèmes Journées Nationales Microondes 2015, Jun 2015, Bordeaux, France. 2015.
[NC.6] M. Ettorre, **M. Casaletti**, R. Sauleau, S.C. Pavone, M. Albani, "Conception et optimisation d'antennes RLSA focalisantes en champ proche, " XIXèmes Journées Nationales Microondes 2015, Jun 2015, Bordeaux, France.
[NC.7] M. Ettorre, F. Foglia Manzillo, **M. Casaletti**, R. Sauleau, N. Capet, "Réseau d'antennes CTS pour applications satellitaires en bande Ka," XIXèmes Journées Nationales Microondes 2015, Jun 2015, Bordeaux, France.
[NC.8] M. Casaletti, G; Valerio, J. Seljan, M. Ettorre, R. Sauleau, "Méthode de raccordement modal pour l'analyse rapide d'antennes SIW," 18èmes *Journées Nationales Microondes (JNM)*, Paris France, 15-17 Mai 2013.
[NC.9] M. Ettorre, S.M. Rudolph, **M. Casaletti**, R. Sauleau, A. Grbic, "Guide radial à ondes de fuite pour la génération de faisceaux de Bessel," 18èmes *Journées Nationales Microondes (JNM)*, Paris France, 15-17 Mai 2013.
[NC.10] M. Śmierzchalski, **M. Casaletti**, K. Mahdjoubi, and S. Collardey, "Determination of Bloch impedance for bi-anisotropic metamaterials," *GDR Ondes: interferences d'ondes*, Nice France, 24-26 October 2011.
[NC.11] M. Casaletti, S. Maci, and G. Vecchi "Shannon basis function set for curved surfaces," *RINEM '10*, Benevento Italy, September 2010.
[NC.12] M. Casaletti, S. Maci, and G. Vecchi "Diffraction-like synthetic functions to treat the scattering from large polyhedral metallic objects," *RINEM '08*, Lecce Italy, September 2008.

Book Chapter (Chapitre de livres)

[BC.1] M. Ettorre, S. C. Pavone, **M Casaletti**, M. Albani, A. Mazzinghi, A. Freni, "Near-Field Focusing by Non-diffracting Bessel Beams" in Aperture Antennas for Millimeter and Sub-Millimeter Wave Applications, Springer, ISBN: 978-3-319-62772-4